MONTAN
UNIVERSITÄT
LEOBEN

Chair of Ceramics

Master's Thesis

# Investigation of new slag compositions for the continuous casting of soft steel

Alan Jiyuan Ye

May 2019

# AFFIDAVIT

I declare on oath that I wrote this thesis independently, did not use other than the specified sources and aids, and did not otherwise use any unauthorized aids.

I declare that I have read, understood, and complied with the guidelines of the senate of the Montanuniversität Leoben for "Good Scientific Practice".

Furthermore, I declare that the electronic and printed version of the submitted thesis are identical, both, formally and with regard to content.

Date 07.05.2019 AlanYe

Signature Author
Alan Jiyuan, Ye
Matriculation Number: 01435688

# Abstract

Mould slag plays a pivotal role in the continuous casting of steel. $CaF_2$-containing slag compositions have been industrially successful, but associated health hazards have been demonstrated. The purpose of this master thesis is to develop a novel $CaF_2$-free slag composition within the $Na_2O$-$K_2O$-CaO-MgO-FeO-MnO-$SiO_2$-$TiO_2$-$Al_2O_3$-$B_2O_3$ chemical system with the help of FactSage and optical basicity calculation. The compositions are expressed as molar ratios between the oxides. The requirements for the composition are to exhibit low crystallization tendency, have a melting point below 1250 $^{o}$C, and viscosity below 3 poise at 1300 $^{o}$C. FactSage was utilized to produce slag compositions that meet such criteria. Several compositions are tested, with a boron-free and a boron-containing compositions meeting most of the criteria.

Slag compositions were mixed from pure raw material, liquefied at 1400 $^{o}$C, and quenched to assess the glass formation ability. Compositions demonstrating high glass formation ability were selected for further testing. Viscosity at 1300 $^{o}$C and dynamic break temperature were determined with the help of a concentric cylinder type rheometer with a cooling rate of 5K/min. Furnace crystallization test and simultaneous thermal analysis were conducted to measure the temperature where crystals are formed. The furnace crystallization test samples were used for scanning electron microscopy to determine the mineralogical composition with the aid of the XRD and SEM results. Time-temperature-transformation diagrams were constructed with single hot thermocouple technique to assess the crystallization tendency.

Two novel slag compositions exhibit relatively satisfactory characteristics. One is a boron-free slag with the chemical composition (wt%) of 39.22% $SiO_2$, 31.39% CaO, 11.53% $Na_2O$, 5.84% $K_2O$, 3.03% MgO, and 8.99% $TiO_2$. Its $T_m$ is 1161 $^{o}$C, but its viscosity at 1300 $^{o}$C is 4.48 poise. Its nose temperature is 900 $^{o}$C, at which point $t_{0.5}$ is 3.6 ± 0.8 sec, and $t_{95}$ is 22 ± 3 sec. Improvements are needed in regards to viscosity. The other slag is a boron-containing composition with the chemical composition (wt%) of 37.23% $SiO_2$, 26.66% CaO, 12.27% $Na_2O$, 6.21% $K_2O$, 2.81% MgO, 8.35% $TiO_2$, and 6.47% $B_2O_3$. Its $T_m$ is 1188 $^{o}$C, and its viscosity at 1300 $^{o}$C is 2.21 poise. Its nose temperature is 700 $^{o}$C, at which point $t_{0.5}$ is 6.1 ± 1.3 sec, and $t_{95}$ is 44 ± 13 sec.

The results from tested compositions suggest that introducing $Al_2O_3$ to the boron-free slag at above 4 wt% increases the crystallization tendency very significantly due to the formation of $C_2S$, but the viscosity is reduced to 3.3 poise. Adding MnO and FeO at small percentages to the boron-free composition significantly reduces glass formation ability. However, if added together with $Al_2O_3$, viscosity is significantly reduced to 1 poise without reduction in glass formation ability.

# Acknowledgement

The investigator of this master thesis topic would like to thank his immediate supervisor, Dr. Nathalie Kölbl, for her instrumental direction in this project. The investigator would also like to thank Dr. Irmtraud Marschall, for the discussions on the project. The investigator would like to thank Mr. Christian Schober for the many hours he had spent on the experiments and training. Finally, the investigator would like to sincerely thank Professor Harald Harmuth for his years of teaching and instruction.

**Table of Contents**

# List of Figures

# List of Tables

# List of Abbreviations and Symbols

| **Abbrev./Symbol** | **Terminology** |
|---|---|
| A/S ratio | $Al_2O_3$ to $SiO_2$ weight ratio |
| AS system | $Al_2O_3$-$SiO_2$ system |
| CA | $CaAl_2O_4$ |
| CAS system | $CaO$-$Al_2O_3$-$SiO_2$ system |
| $CAS_2$ | anorthite |
| CASB system | $CaO$-$Al_2O_3$-$SiO_2$-$B_2O_3$ system |
| CMAST system | $CaO$-$MgO$-$Al_2O_3$-$SiO_2$-$TiO_2$ system |
| CMS system | $CaO$-$MgO$-$SiO_2$ system |
| CS | wallastonite |
| CS system | $CaO$-$SiO_2$ system |
| $C_3A$ | $Ca_3Al_2O_6$ |
| $C_3B$ | $Ca_3B_2O_6$ |
| $C_3S_2$ | rankanite |
| C/A ratio | $CaO$ to $Al_2O_3$ weight ratio |
| C/S ratio | $CaO$ to $SiO_2$ weight ratio |
| CTS | sphene |
| CTS system | $CaO$-$SiO_2$-$TiO_2$ system |
| $C_{12}A_7$ | majenite |
| $C_2AS$ | gehlenite |
| $C_2B$ | $Ca_2B_2O_5$ |
| $C_2S$ | belite |
| $C_xA_yBS_z$ | $Ca_xAl_{2y}B_2Si_zO_{(x+3y+2z+3)}$ |
| $C_xM_yS_z$ | $Ca_xMg_ySi_zO_{(x+y+2z)}$ |
| DTA | differential thermal analysis |
| FCT | furnace crystallization test |
| GFA | glass formation ability |
| KAS system | $K_2O$-$Al_2O_3$-$SiO_2$ system |

| | |
|---|---|
| KCS system | $K_2O$-CaO-$SiO_2$ system |
| $K_xC_yS_z$ | $K_{2x}Ca_ySi_zO_{(x+y+2z)}$ |
| $\Lambda_{th}$ | optical basicity |
| LOI | loss of ignition |
| MAS system | MgO-$Al_2O_3$-$SiO_2$ system |
| $M_xA_yS_z$ | $Mg_xAl_{2y}Si_zO_{(x+3y+2z)}$ |
| NABS system | $Na_2O$-CaO-$B_2O_3$-$SiO_2$ system |
| NAS system | $Na_2O$-$Al_2O_3$-$SiO_2$ system |
| NCAS system | $Na_2O$-CaO-$Al_2O_3$-$SiO_2$ system |
| NCS system | $Na_2O$-CaO-$SiO_2$ system |
| N/K ratio | $Na_2O$ to $K_2O$ ratio |
| $N_xC_yS_z$ | $Na_{2x}Ca_ySi_zO_{(x+y+2z)}$ |
| PaS | N•sec/$m^2$ |
| $R_{crit}$ | critical cooling rate |
| RO | CaO or MgO |
| rpm | rotation per minute |
| $R_2O$ | $Na_2O$ or $K_2O$ |
| SEM | scanning electron microscope |
| SHTT | single hot thermocouple technique |
| S/(N+A+S) ratio | $SiO_2$ to ($Na_2O$+$Al_2O_3$+$SiO_2$) weight ratio |
| $T_{br}$ | breaking temperature |
| $T_{crys,onset}$ | onset of crystallization temperature |
| $T_g$ | glass transition temperature |
| $T_m$ | melting point |
| $T_o$ | Vogel-Fulcher-Tammann temperature |
| $T_{rg}$ | reduced glass transition temperature |
| TTT | time-temperature-transformation |
| wt % | weight percentage |
| XRD | X-ray powder diffraction |

## 1. Problem Definition

Mould powder is added to the mould on top of liquid steel in the continuous casting process. The mould powder liquefies and the liquid slag is entrapped into the gap between the strand and the mould where a liquid, crystalline and glassy layers are formed. The mould powder should fulfill the following tasks: lubrication of the steel, ensuring a consistent and sufficient rate of heat transfer, preventing the steel from re-oxidation, and absorption of inclusions from the steel. The mould slag should not react with the steel, or leach a significant amount of precious alloy metals from the steel.

In order to guarantee a trouble free operation for soft steel, a successful slag composition should have the following properties. The liquidus temperature of the mould slag should be below 1250 $^{o}$C. The ideal temperature would be below 1160 $^{o}$C to ensure the continuity of the slag liquid film layer and reduce slag rim formation. Low viscosities at 1300 $^{o}$C are also desirable, the criteria being below 3 poise for ensuring the entrapment into the gap. A high degree of glass phase formation is desired over crystallization in the solid layers of slag. Therefore, devitrification is to be reduced.

The established mould powder recipe works within the $CaO$-$SiO_2$-$CaF_2$ system, with the crystalline phase being cuspidine. This chemical system has excellent properties such as low liquidus temperature and decreased viscosity at working temperature. However, partial pressures of volatile $NaF_{(g)}$ and $KF_{(g)}$ is formed at working temperatures, and this in turn reacts to form HF, which is hazardous to operators and intensifies machine wear. As a result, industry has been searching for an alternative chemistry system that offers similar properties without the adverse health impacts. Some of the proposed fluorine-free chemistry systems use $LiO_2$, $B_2O_3$, $Na_2O$, $K_2O$, $La_2O_3$, and $TiO_2$ as substitutes of $CaF_2$. In this master thesis, the chemical system has to operate within the $SiO_2$-$Al_2O_3$-$Na_2O$-$K_2O$-$CaO$-$MgO$-$TiO_2$-$B_2O_3$ system. FeO and MnO can also be introduced but may not exceed 0.8 wt% for each. The amount of $TiO_2$ also may not exceed 20 wt% for economic consideration. The melting points and viscosities of possible chemical compositions will be calculated with the commercially available software FactSage. If the requirements given above are fulfilled, samples will be mixed from pure raw materials, liquefied and quenched to room temperature on an iron plate. If a glassy specimen is formed, crystallization tendency of the slag is investigated using simultaneous thermal analysis (DTA), furnace crystallization test (FCT), and single hot thermocouple technique (SHTT). From SHTT the time-temperature-transformation diagrams are generated. Additionally the mineralogical compositions of the FCT specimens will be investigated.

# 2. State of Art

## 2.1. Mould in the continuous casting of steel process

Continuous casting of steel has become the primary casting method of the steel industry due to its high quality and efficiency. The continuous casting process starts with the molten steel from the ladle and ends with the solidified slab as seen in Figure 1 [1]. Molten steel is fed from the ladle into the tundish, where its temperature is monitored and a constant molten steel level is maintained for slab quality [2-4].

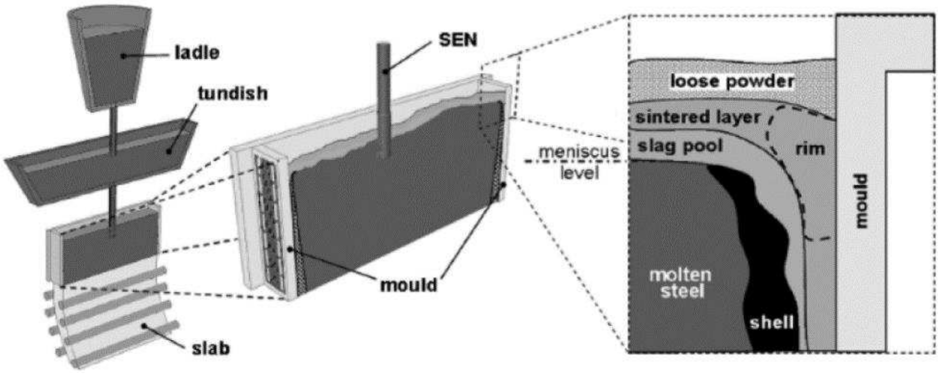

Figure 1. A depiction of the mould [5]

The mould is open on both of its vertical ends. The oxidation of the steel is prevented by covering the top opening with loose mould powder. The mould is made of copper due to the high thermal conductivity, and the inner surfaces of the mould could be coated with a layer of Ni and Cr in order to reduce wear. The heat transfer out of the mould is facilitated by running water, and the heat flux is controlled to be constant. Molten steel cools down and partially solidifies due to the heat transfer. The solidified section of steel is called the shell, and grows in thickness as the steel is transported downwards. The shell has to be able to hold the liquid melt inside. The shell and molten steel, together called the strand, are transported downwards at a constant rate in order to prevent crack formation. The transport rate is called casting speed, which is typically 0.7 to 2 m/min. A small shrinkage takes place due to steel cooling down, and as a result the mould is designed with a concave shape that corresponds to this shrinkage. This helps facilitating the heat transport by reducing the air gap between the shell and the mould. The downwards transport of the shell is lubricated by the mould slag [6].

## 2.2. Mould slag

Mould powder is supplied to the top opening of the mould onto the liquid steel, where it liquefies. It is entrapped into the gap between the strand and the mould, where it solidifies and differentiates into the liquid slag film, crystalline slag film, and the glassy slag film. The three films together are about 3-5 mm in thickness. State of the art slag composition uses $CaF_2$

as a main network modifier due to its effect in significantly lowering viscosity and melting point. The main phase in the crystalline slag film is cuspidine, $3CaO \cdot 2SiO_2 \cdot CaF_2$, which is excellent for controlling the heat transfer [7]. The chemical composition range of common slags is shown in Table 1. Important performance parameters for mould slags are viscosity and melting point. The requirements for these parameters vary depending on the type of steel casted. The requirements are listed in Table 2 [9-17].

Table 1. $CaF_2$-containing slag chemical range [8]

| Component and Composition in wt (%) | | | | | |
|---|---|---|---|---|---|
| $CaF_2$ | 2-15 | $Fe_2O_3$ | 0-6 | SrO | 0-5 |
| $B_2O_3$ | 0-10 | CaO | 22-45 | $Li_2O$ | 0-5 |
| $SiO_2$ | 17-56 | MgO | 0-10 | $K_2O$ | 0-2 |
| $Al_2O_3$ | 0-13 | MnO | 0-5 | $Na_2O$ | 0-25 |
| $TiO_2$ | 0-8 | BaO | 0-10 | carbon | 2-20 |

Table 2. Performance requirements for slags [9-17]

| Steel Type | Carbon Content (wt%) | Casting Speed (m/min) | Viscosity at 1300 ºC (Poise) | Melting Point (ºC) |
|---|---|---|---|---|
| low-carbon steel | < 0.08 | 0.8-2.0 | 0.4-3 | 970-1150 |
| medium-carbon steel | 0.08-0.25 | 0.8-1.6 | 0.5-3.9 | 1050-1190 |
| high-carbon steel | > 0.25 | 0.7-1.3 | 0.8-2 | 980-1180 |
| stainless steel | | 1.2-1.4 | 4-5 | 1150-1180 |

The behavior of the powder in the mould is shown in Figure 2. The powder and sintered powder is kept at a depth of 10-15 cm by supplying fresh powder. The powder consumption for common $CaF_2$-containing slags is typically about 0.3 kg per ton of steel casted. Typical powder compositions contain 4 to 20 % carbon, which creates a $CO/CO_2$ flux upwards to the surface in the liquid slag. This keeps the mould under reducing conditions. The alkaline contents of the mould powder normally are added in the carbonate form, as this is much more stable for storage. The depth of the liquid slag layer is desirably to be kept relatively constant at 10 mm. A thin mushy slag layer consisting of liquidus slag, sintered powder, and resolidified slag exists between the liquid slag and sintered powder layer. It is prevented from intruding into the gap between mould wall and steel shell by the rim. The rim is a layer composed of sintered powder and resolidified slag and congregates next to the walls of the mould on top of the liquid slag layer. The rim serves an important function of applying a force helping to push the liquid slag in between the mould wall and the steel shell. [18, 19].

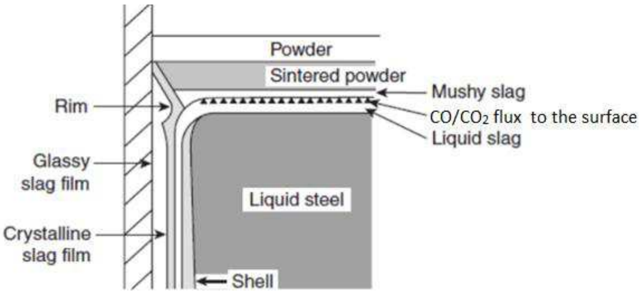

Figure 2. Different layers of the mould powder and slag in the mould [20]

Industry has expressed a desire to move away from $CaF_2$-containing mould fluxes, due to the fluorine emissions, which forms fluoric acid that corrodes production aggregates and poses long-term health hazards for workers. As the slag powdered is sintered, the first liquid phases occur, which have a concentration of alkalis and fluorine due to their low eutectic points. Fluorine reacts with the alkalis, which result in partial pressures of fluorine being released to the atmosphere [21, 22].

$$Na_2O_{(slag)} + CaF_{2(slag)} \leftrightarrow CaO_{(slag)} + 2Na^+_{(g)} + 2F^-_{(g)} \tag{1}$$

$$K_2O_{(slag)} + CaF_{2(slag)} \leftrightarrow CaO_{(slag)} + 2K^+_{(g)} + 2F^-_{(g)} \tag{2}$$

A common industrial slag with 14 wt% $Na_2O$ and 9 wt% $CaF_2$ is shown to yield a partial pressure of NaF of 4.4 kPa at 1300 °C. This is not so insignificant. In the subsequent alkali condensation reaction, the fluorine may react with the humidity in atmosphere, which lead to the very harmful substance HF:

$$2Na^+_{(g)} + 2F^-_{(g)} + H_2O_{(g)} \rightarrow Na_2O_{(s)} + HF_{(g)} \tag{3}$$

The fluorine content also reacts with the other oxides in the slag to produce partial pressure of $SiF_4$, $AlF_3$, $BF_3$, and $MgF_2$. However, these partial pressures are insignificant when compared to those of NaF and KF. The saturated partial pressure of $MgF_2$ is only 1 Pa at 1300 °C [23].

It may appear that fluorine emission could be resolved by developing an alkali-free slag compositions. However, the consequent rise in viscosity and melting point cannot be remediated. Therefore, substitute for $CaF_2$ in slag recipe has been the topic of interest [7].

### 2.2.1. Property considerations

Depending on steel grade, special requirements on physical properties of mould slags are important for producing good quality products. Major defects that could possibly occur during the continuous casting of steel include nonmetallic inclusions, breakout, cracks, and oscillation marks. Of these breakout is the most serious, and is often associated with reduction in the lubrication of the strand [24]. Cracks occur due to too high tensile stresses in the strand associated with the rate of heat transfer to the slag. Oscillation marks are somewhat made more severe due to too high viscosity of the slag [25].

#### 2.2.1.1. Viscosity

One of the most important properties of mould slags that affect the quality of the strand and the efficiency of the casting process is viscosity. It plays a pivotal role in slag infiltration and lubrication of the strand. The viscosity of a liquid depends on its chemical composition and temperature as expressed by the Fulcher-Vogel-Tammann equation [66]:

$$\ln(\mu) = A + \frac{B}{T - T_o} \quad (4)$$

where T is the temperature; $T_o$ is the Vogel-Fulcher-Tammann temperature, at which the viscosity of the glass goes to infinity; $\mu$ is the viscosity at temperature T; A, B are constants calculated by complex non-linear equations in relation to the chemical composition.

Fluorine free mould slag compositions may include the following oxides: $SiO_2$, $Al_2O_3$, $B_2O_3$, $TiO_2$, CaO, MgO, SrO, FeO, MnO, $Na_2O$, and $K_2O$ [26-32]. Their relative effects on viscosity of the slag, which somewhat correspond to their role in the glass network theory in relation to Dietzel's field strength,

$$Dietzel's\ field\ strength = Z/\alpha^2 \quad (5)$$

where Z is the ion valency of the non-oxygen ion, and $\alpha$ is the distance of the balance points of the positively charged ion and the oxygen. The effect of selected oxides on the viscosity and melting point of a non-basic slag are generalized below in Table 3:

Table 3. Properties of selected oxides and their effects on viscosity and melting point ($T_m$); CN refers to coordination number [26-32]

| | SiO2 | Al2O3 | | B2O3 | | TiO2 | CaO | MgO | SrO | Na2O | K2O |
|---|---|---|---|---|---|---|---|---|---|---|---|
| Viscosity | ↑↑ | ↑↑↑ (1) | | ↓↓↓(2) | | ↓ | ↓↓ | ↓↓ | ↓ | ↓↓↓ | ↓↓↓ |
| Tm | ↑↑ | ↑↑↑ | | ↓↓ | | ↑ | ↓↓ | ↓↓ | ↓ | ↓↓↓ | ↓↓↓ |
| M in MOx | Si | Al | | B | | Ti | Ca | Mg | Sr | Na | K |
| CN | 4 | 4 | 6 | 3 | 4 | 6 | 8 | 6 | 8 | 6 | 8 |
| Single bond strength (kcals) | 106 | 79-101 | 53-67 | 119 | 89 | 73 | 32 | 37 | 32 | 20 | 13 |
| Dietzel's Field Strength | 1.57 | 0.96 | 0.84 | 1.63 | 1.34 | 1.04 | 0.33 | 0.45 | 0.28 | 0.19 | 0.13 |
| Ionic radius for CN=6 (Å) | 0.39 | 0.57 | | 0.20 | | 0.64 | 1.06 | 0.78 | 1.27 | 0.98 | 1.33 |

(1) only if the moles of basic oxides is more than the moles of nonbasic oxides, which is likely to be the case

(2) depends on the amount of basic oxide due to boron anormaly

| | |
|---|---|
| ↑↑↑ | relatively greatly increase |
| ↑↑ | increase |
| ↑ | relatively slightly increase |
| ↓ | relatively slightly decrease |
| ↓↓ | decrease |
| ↓↓↓ | relatively greatly decrease |

In the glass network theory, oxides with low basicity, which can be identified with a Dietzel's field strength above 1.4 and molar single bond strength above 80 kcals, are the network formers, and provide the bridging oxygen bonds in the glass matrix. Oxides with high basicity are the network modifiers. They create non-bridging oxygen bonds. The network modifiers have a Dietzel's field strength below 0.4 and molar single bond strength below 20 kcals. Others are intermediate oxides. As can be seen in Table 1, network formers generally increase the viscosity of the melt due to increasing number of bridging oxygen bonds, while network modifiers have the opposite effect due to increasing number of non-bridging oxygen bonds [66].

$SiO_2$ is the primary network former in several glass systems. Alkali network modifiers only have marginal ability in lowering the viscosity if $SiO_2$ molar content is above 60%. This is due to the high viscosity associated with the $Q^n$ unit distribution between $Q^3$ and $Q^4$, where n is the number of bridging oxygens per Si atom. So the $SiO_2$ molar content of the mould slag must be below 60% [33].

It has been suggested in literature, that the viscosity of a glass system with $SiO_2$ as the primary network former will be significantly lowered by introducing different oxides at low percentages, such as below 0.5 molar percent, due to the increase in entropy of the melt [33]:

$$\ln(\mu) = A_e + \frac{B_e}{T * S(T)} \tag{6}$$

where $A_e$ is the high temperature viscosity limit, which is the viscosity close to the vaporization temperature of the liquid slag; $B_e$ is a constant in $Jmol^{-1}$ proportional to the potential barrier opposed to the cooperative rearrangement of the liquid structure; S(T) is the melt configurational entropy at temperature T. The oxides are not necessarily network formers, network modifiers, or intermediates; the entropy of the system increases with every additional oxide. Of course, if the additional oxides were network formers, this viscosity lowering effect is lost once the dosage of the oxides exceeds a certain threshold. The threshold could be understood as the marginal solubility limit of the oxide in a pure silica melt. Therefore the viscosity of the silica-rich melt will not be lowered with small amounts of $Cr_2O_3$ or $ZrO_2$. Since the oxides are introduced at molar percentages below 0.3%, it is reasonable to assume that the slag phases will not be affected qualitatively. However, the complexity of the chemical system may possibly leads to reaction with the steel [34].

$B_2O_3$ is a network former. Pure boron glass matrix consist of $BO_3$ triangles and boroxol rings. The $BO_3$ glass configuration is transformed to $BO_4$ tetrahedra configuration as alkali oxides are introduced in the glass matrix. This transformation takes place in a linear fashion until $R_2O/B_2O_3$ molar ratio reaches 0.5. This gives rise to the expectation that minimums in viscosity and melting point of alkali-borate glass could be expected when alkali molar content is around 30%. However, this is not the case due to boron anomaly. The minimum in properties could be expected at $R_2O/B_2O_3$ ratio of 16/84 [35].

Unlike other network formers, $B_2O_3$ has the effect of very significantly lowering viscosity in the haplogranitic system ($K_2O$-$Na_2O$-$Al_2O_3$-$SiO_2$) across all temperatures, which makes it a rather useful addition for this purpose to any slags in the KAS or NAS systems. Literature shows that while the $B_2O_3$ has a pronounced effect on viscosity with dosage ranging from 1 to 25 weight percent, at higher dosage this effect has diminishing returns. The most cost-effective dosage for minimizing viscosity has been suggested to be between 1 to 4.4 wt% $B_2O_3$ [36].

$Al_2O_3$ is an intermediate oxide, but acts as a primary network former in many glass systems due to the activation by network modifiers when $R_2O/Al_2O_3$ molar ratio is above 1. Al substitutes the Si in the glass matrix, but has a much higher effect on increasing viscosity than $SiO_2$ per mole overall [31]. This is not entirely true however due to the entropy consideration mentioned in equation 6. It has been suggested that for the CAS system there is an optimum A/S weight ratio at 0.1 for minimum viscosity [29].

$TiO_2$ is an intermediate oxide, but at below around 10 molar percent acts as a network former in a common NCAS glass system by forming glass matrix of interconnected $TiO_4$ and $SiO_4$ tetrahedra. In this range, replacing $SiO_2$ with $TiO_2$ content results in decrease in viscosity. At above 10 molar percent of $TiO_2$, rising fractions of Ti result in the formation of $TiO_5$ polyhedra, which lead to small increases in viscosity. It has been suggested that in a CMAST system, the viscosity increases linearly as $TiO_2$ is substituted by $Al_2O_3$ on a 1 to 1 molar ratio within the $Q^n$ region where $Q^2$ to $Q^3$ ratio is below 1.65, where both $Al^{3+}$ and $Ti^{4+}$ still enter the matrix as network formers in the forms of $AlO_4$ and $TiO_4$. This is due to, as two $Al^{3+}$ replace two $Ti^{4+}$, one $Ca^{2+}$ is needed to keep the equilibrium of electric charge. So for every two mole of $TiO_2$ that are replaced by $Al_2O_3$, one mole of CaO no longer acts as network modifier, and the viscosity increases [37-39].

Alkali oxides are network modifiers, and reduce viscosity within all aluminosilicate glass systems. Alkali containing AS glass systems exhibit mixed alkali effect for viscosity, so as one alkali ion is substituted by another, the viscosity changes predictably, first decreasing to a minimum, then rising again until one alkali ion is completely substituted. This means that a minimum in viscosity can be expected for each system associated with a particular molar ratio of for example $K_2O/(Na_2O+K_2O)$ [40].

Alkaline earth oxides can be categorized as network modifiers, although they exhibit less influence on viscosity per mole as compared to alkalis due to higher Dietzel's field strength. It has been suggested that a similar alkaline earth mix effect exists between MgO and CaO, and that a minimum in viscosity can be expected for a particular molar ratio of MgO/(MgO+CaO) [41]. However, finding this ratio may not be as important as finding the $K_2O/(Na_2O+K_2O)$ ratio, since a limit to MgO content could be expected in order to avoid paragenesis of $C_xM_yS_z$ phases, which have both high melting points and high devitrification tendencies [42].

There are several models to predict viscosity of slags. For $CaF_2$-$B_2O_3$-free slags, the modified Iida model, which correlates the activity coefficients of the oxides in dependence of temperature to viscosity, has good accuracy (±25%) compared to other models. The viscosity of a slag is calculated as:

$$\mu = A * \mu_o * \exp(E/B_i), \qquad (7)$$

where A and E are temperature (in Kelvin) dependent parameters:

$$A = 1.029 - 2.078E - 03 * T + 1.050E - 06 * T^2 \qquad (8)$$

$$E = 28.46 - 2.088E - 02 * T + 4.000E - 06 * T^2 \quad (9)$$

$\mu_o$ is the sum of the partial viscosities of the melts of each oxide in dependence of temperature, $\mu_{oi}$, multiplied by their weight fractions, $X_i$

$$\mu_o = \sum \mu_{o_i} * X_i \quad (10)$$

Iida model is based on a modified basicity index, $B_i$, which categorizes the oxides as basic ones, denoted by B, and non-basic ones, denoted by A.

$$B_i = {\sum(\alpha_i X_i)_B}\Big/{\sum(\alpha_i X_i)_A} \quad (11)$$

The activity coefficient, $\alpha_i$, is the interaction of the oxide with other components of the slag. For 1300 °C, the $\alpha_i$ and $\mu_{oi}$ of selected oxides of interest are listed in table 4:

Table 4. Activity coefficient and partial viscosities (in $10^{-3}$•PaS) of selected oxides [43, 44]

| non-basic oxide | $SiO_2$ | | $B_2O_3$ | | $Al_2O_3$ | | $TiO_2$ | |
|---|---|---|---|---|---|---|---|---|
| | $\alpha_i$ | $\mu_{oi}$ | $\alpha_i$ | $\mu_{oi}$ | $\alpha_i$ | $\mu_{oi}$ | $\alpha_i$ | $\mu_{oi}$ |
| | 1.48 | 4.64 | 2.12 | 0.33 | 0.1 | 10.22 | 0.36 | 8.12 |
| basic components | CaO | | MgO | | MnO | | FeO | |
| | $\alpha_i$ | $\mu_{oi}$ | $\alpha_i$ | $\mu_{oi}$ | $\alpha_i$ | $\mu_{oi}$ | $\alpha_i$ | $\mu_{oi}$ |
| | 1.53 | 33.03 | 1.51 | 56.51 | 1.03 | 9.35 | 0.96 | 4.2 |
| | Li2O | | Na2O | | K2O | | CaF2 | |
| | $\alpha_i$ | $\mu_{oi}$ | $\alpha_i$ | $\mu_{oi}$ | $\alpha_i$ | $\mu_{oi}$ | $\alpha_i$ | $\mu_{oi}$ |
| | 3.55 | 4.01 | 1.94 | 0.93 | 1.37 | 0.51 | 1.53 | 2.59 |

Another popular slag viscosity model is the Urbain model designed for complex slags in the CAS system, which gives an accuracy of ±30% for $CaF_2$-containing slags [45]. However, it has rather large inaccuracies for the $CaF_2$-free systems as it categorizes $TiO_2$ and $ZrO_2$ as network modifiers. This problem has been mitigated in the modified Urbain model proposed by Dong *et al* [46].

Iida model has significant inaccuracies for $B_2O_3$-containing slags, as upwards of 100% error has been reported [47]. Modified Urbain model could predict within ±30% accuracy for $B_2O_3$-containing slags [48]. The NPL model proposed by Mills and Sridhar based on optical basicity, $\Lambda_{th}$, could predict viscosity within ±60% accuracy for $B_2O_3$-containing slags [49]. A modified NPL (New Philadelphia Laboratory) model is proposed by Ray and Pal, which is very accurate for glasses but less so for slags [50]. Shankar has proposed another modified NPL model (see section 2.2.1.6), which can also be considered a modified Riboud model, based on a modified basicity index for slags, which could predict viscosity within ±15% accuracy for $B_2O_3$-containing slags [51].

Viscosity of a slag is often measured by a high-temperature rotational rheometer. The slag is melted in a crucible at 1400 °C, and its viscosity is measured as the temperature is decreased. The viscosity in logarithmic scale plotted against the inverse of temperature in $K^{-1}$ would yield a graph akin to Figure 3, which can be used to determine the breaking temperature, $T_{br}$. Two straight lines approximating the tangents to the viscosity curves are drawn, and their intersection determines $T_{br}$. At this temperature it is thought that the solid and liquid state within the slag film is 50-50. $T_{br}$ depends on the cooling rate during the measurement, and therefore experimental procedures must be stated to compare the results of different slags [52].

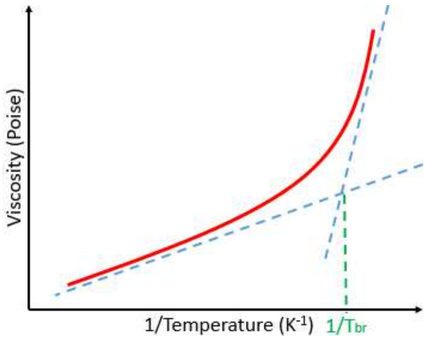

Figure 3. Illustration of determination of $T_{br}$ from rheometer result

### 2.2.1.2. Melting point

A slag with low melting point offers excellent lubrication properties and facilitate fast slab growth. The melting point of the slag is predetermined by its chemical composition. In Table 1, the effect on the melting point of the slag by increasing the content of each oxide is generalized. However, while these trends are certainly useful guidelines for developing new slag compositions, they are only true as long as the crystallization mechanism of the slag is not changed. If the composition enters a different composition triangle or tetrahedral due to the increasing content of one oxide, the melting point of the slag could become too high due to formation of a mineral phase with high $T_m$. The composition of the slag should not be located within the composition triangles that will result in the paragenesis of such a phase. However, while many ternary phase diagrams are well-established, it is difficult to consult them due to the complexity of the slag compositions. As observed with many pseudo-ternary phase diagrams, the primary fields of the phases could shrink, expand, or shift significantly due to the presence of an oxide not belonging to the ternary system. In some cases, a congruently melting phase could become incongruently melting, and cooling in disequilibrium avoids its formation. Therefore, pseudo-ternary phase diagrams should be consulted to reasonably estimate if the paragenesis of a phase with high $T_m$ would take place. Also, due to the complex chemistry of the slag, the liquidus surfaces of the phases should be significantly lowered in terms of temperature when compared to the ternary phase diagrams.

For a common $CaF_2$-containing mould slag within the chemical range of: 65-75% ($CaO+SiO_2$), C/S ratio is between 0.7 and 1.3, 0-6% M, 2-6% A, 2-10% (N+K), up to 10% $CaF_2$, with possible $TiO_2$ and MnO additions, the melting point could be predicted according to the following relation to within ±35 °C [53]:

$$T_m = 1191 + 4.2 * X_A + 11.4 * X_S - 11 * X_C + 5.7 * X_M + 8.3 * X_F + 11.6 * X_{MnO} - 15.8 * X_K - 10.1 * X_N + 1.9 * X_{CaF_2} \quad (12)$$

$T_m$ is in degree Celsius, and X are weight fractions in percentage. As can be observed, MgO has a completely opposite effect on melting point as listed in Table 1. This is due to its unwanted effect on shrinking the primary field of cuspidine. The melting points of fluorine containing mould slags show good predictability attributable to the enlargement of the cuspidine primary field due to the addition of further oxides [54]. The $CaF_2$-free slags do not permit the same level of predictability due to the complexity of their phase formation, which will be discussed in section 3.

Differential thermal analysis, DTA, provides an accurate method to measure the melting point of the slag. An inert reference material or an empty crucible alongside the slag (65 mg) is heated at a constant rate (5 K/min) to 1400 °C. Then both are cooled with a defined rate of for example 5 K/min. The temperature difference between the two crucibles indicates the phase changes occurring within the slag, including the melting of the slag. They go along with exothermal or endothermal heat zones, which can be seen as peaks within the DTA-curve. However, if the slag contains a significant amount of alkalis and $B_2O_3$, due to the large surface area to volume ratio of the sample, a significant amount of material loss can take place, in which case DTA does not give an accurate evaluation of $T_m$ [55].

Furnace crystallization test, FCT, provides a more accurate assessment of the melting point when the slag contains significant amount of volatiles. The working principle of FCT is the same as DTA, except for the sample loading (27 g) and the percentage of material loss is less than that of DTA [56].

### 2.2.1.3. Heat transfer

Heat is transferred from the liquid steel to the mould through the slag, which allows the initial solidification of the slab to take place. Uniform and consistent heat transfer is one of the key factors to avoid surface defects of the slab. Heat transfer that is too low would result in insufficient strand shell thickness; high heat transfer is somewhat preferred, but could lead to longitudinal cracks on slab surface if it was too high. Non-uniform heat transfer is often detrimental, especially during casting hypo-peritectic steel [57]. The heat transfer of the slag is difficult to calculate, as it depends on the slag chemical composition [58], crystallization tendency, and melting rate. It is further complicated in actual operation by the slab speed and steel grade [23].

As shown in Figure 2, the slag film can be divided into a liquid film in contact with the slab, a crystalline film, and a glassy film. There is also a small air gap between the slag film and the mould wall which results in an interfacial thermal resistance. The heat transfer from the slab to the mould wall therefore could be depicted in terms of thermal resistance as shown in Figure 4, and the following relationship could be drawn:

$$T_{slab} - T_{wall} = q_{tot} * (R_{liquid} + R_{crystal} + R_{glass} + R_{int}) \qquad (13)$$

where $q_{tot}$ is the heat flux, $T_{slab}$ is the temperature of the slab surface in contact with slab, $T_{glassy}$ is the temperature at which the viscosity is too high for crystallization to occur, and $T_{wall}$ is the temperature of the hot side of the mould wall. Resistance has the unit $m^2/(MW)$. $R_{int}$ is the thermal resistance of the interfacial gap.

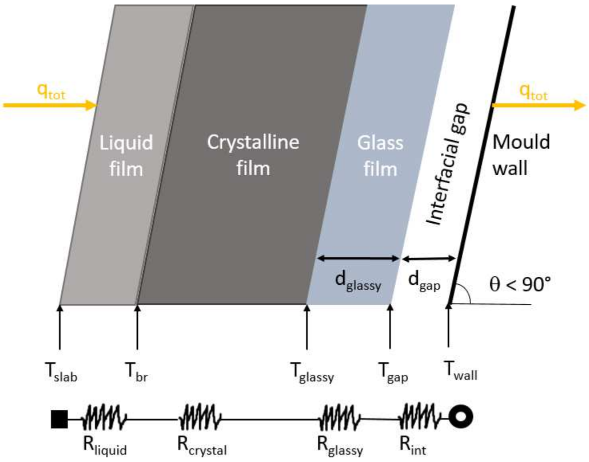

Figure 4. Heat flux from the slab to the mould wall depicted in thermal resistance terms

For the liquid slag film, the Rayleigh number of a low viscosity slag in continuous casting process is typically in the $10^6$ magnitude range, which means the dominant mode of heat transfer in the liquid slag film is convection. It could be generalized that a slag with low melting point typically has a high heat transfer coefficient [59].

The heat convection and lubrication provided by the liquid film is important for minimizing longitudinal cracks and sticker breakout for the slab. In Figure 4, the distinction between slag liquid film and crystalline film is defined to be at the break temperature. Therefore the break temperature is an important physical parameter for the slag. The break temperature is lower than the melting point of the slag; $T_{br}$ is typically 1100-1200 °C for established $CaF_2$ containing slags, and could be lowered to 1000 °C in $B_2O_3$ containing slags. $T_{br}$ has a linear relationship to the chemical composition of the slag in the steady state:

$$T_{br} = 1180 - 3.94 * X_A - 7.87 * X_S + 11.37 * X_C - 9.88 * X_M + 24.34 * X_F + 0.23 * X_{MnO} - 30.87 * X_K + 6.96 * X_N - 17.32 * X_{CaF_2} \quad (14)$$

where $T_{br}$ is in degree Celsius. Equation 14 could predict $T_{br}$ to an accuracy within ±30 °C. $T_{br}$ values can be very different in dynamic situations, and have different measured values due to different rates of cooling, but the linear dependency on chemical composition remains [53].

The mode of heat transfer in the crystalline and glassy film is conduction. The thermal conductivity of the crystalline film depends on the crystal phases. Different phases have different thermal conductivities, which lower the uniformity. Therefore in order to generate uniform and consistent heat transfer, having the paragenesis of only one type of crystal is most ideal. However, this is difficult to achieve. As a result, the crystallization mechanism and crystal growth are important areas of investigation that need to be carried out. Glassy slag films have uniformity of thermal conductivity [54].

Interfacial gaps occur due to the shrinkage of the slag during crystallization, and are therefore unavoidable. The mode of heat transfer across the gap is radiation, and therefore $R_{int}$ value depends on the emissivity and absorptivity of the glassy film. These two physical parameters are predictable in the CAS glass formation regions, as this chemical system is well studied [60].

The $R_{liquid}$, $R_{crystal}$, and $R_{glassy}$ of the slag could be measured by infrared emitter technique, IET. Set up of such an experiment can be seen in Figure 5 [61]. The heat flux is provided through infrared radiation from the top. Slag sample is loaded below the infrared lamp, and on top of a copper surface, which is water-cooled. The hot face temperature is controlled to approximate $T_{br}$. So that some liquid phase is present at the hot face. The cold face temperature is around 600 °C. Thermocouples are imbedded within the slag, and the temperature gradients could be measured. $q_{tot}$ is measured by the water flow rate and the temperature difference between water inlet and outlet. The thermal resistance can then be calculated, for example

$$T_1 - T_2 = q_{tot} * R_{1-2} \tag{15}$$

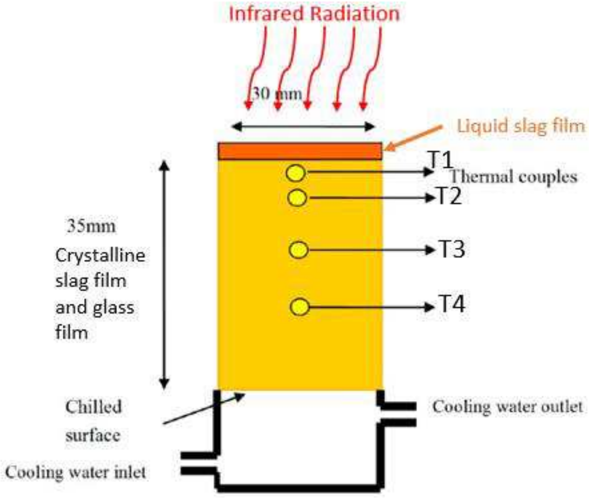

Figure 5. IET set up [61]

The radiative thermal conductivity, $K_{rad}$, could be measured experimentally to within ± 5% accuracy using the Fourier transform infrared spectrometer, FTIR. Sample is prepared as a cut disc of 0.3 ± 0.02 mm from quenched glassy slag, heat flux is provided by an infrared beam emitter, and the receiver is made of copper. The effect of crystallization on radiative heat transfer could also be measured by raising the power output, allowing crystallization to take place in the disc. In order to estimate $d_{gap}$, the slag is assumed to behave like grey gas, yielding:

$$q_{tot} = K_{glassy} * \frac{T_{glassy} - T_{gap}}{d_{glassy}} = K_{rad} * \frac{T_{gap} - T_{wall}}{d_{gap}} \tag{16}$$

$$K_{rad} = \beta \frac{(T_{glassy}^4 - T_{gap}^4)}{T_{glassy} - T_{gap}} d_{glassy} \tag{17}$$

$$\beta = \frac{n_e^2 k}{0.75 \alpha d_{glassy} + \varepsilon_{glassy}^{-1} + \varepsilon_{copper}^{-1} - 1} \tag{18}$$

Here, $n_e$ is the refractive index, assumed to be 1.6 for glassy slag; k is the Stefan-Boltzmann constant; $\alpha$ is the absorption coefficient, assumed to be 400 $m^{-1}$ for glassy slag; $\varepsilon_{glassy}$ is the emissivity for glassy slag, assumed to be 0.92; $\varepsilon_{copper}$ is the emissivity for copper, assumed to be 0.4. The temperatures are in Kelvin [62].

Experiments have shown that it is difficult to correlate the chemical composition of the slag with its measured thermal resistance. This is in part due to the difficulty in predicting the depth of the two films, although the sum of the depth is often controlled. As can be seen in Figure 6, for an industrial slag containing 2 wt% MgO, 9 wt% $Na_2O$, 6 wt% $CaF_2$, 0.5 wt% $Li_2O$, the alumina content is increased linearly from point 1 to 4 while C/S ratio is maintained. However, there is no observable linear pattern in the thermal resistance parameters [57].

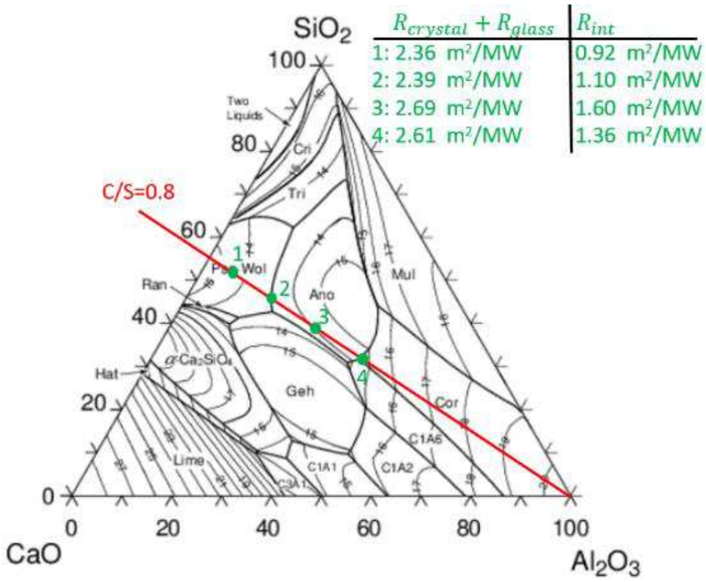

Figure 6. Thermal resistance for compositions with C/S ratio of 0.8 and increasing $Al_2O_3$ contents [57]

### 2.2.1.4 Glass formation ability

Glass can be considered a supercooled liquid. In theory, any thermodynamically stable melt (no creeping or evaporation) can be formed into glass by being cooled rapidly enough below its glass transformation temperature, $T_g$, which prevents the formation of nuclei or significant amount of crystal. Here $T_g$ may be defined as the temperature for a viscosity of $10^{12}$ PaS is reached, where crystal growth due to diffusion is impeded by such high viscosity [52]. Glass formation ability, GFA, of such a stable melt is defined to be the ease of a melt to undergo vitrification upon cooling. This parameter does not have a consensus in its measurements and unit, but is often defined by the critical cooling rate, $R_{crit}$, the minimum cooling rate that results in the vitrification of the liquid. Barandiaran proposes that $R_{crit}$ is related to the melting point, $T_m$ (in Kelvin), and can be calculated according to the following equation:

$$R_{crit} = \exp(A - \frac{B}{T_m^2}) \quad (19)$$

where A and B are empirical constants based on formulas related to chemical composition. A lower melting point results in a smaller $R_{crit}$, and a higher GFA [63, 64].

It has been proposed by Takeuchi that a slag with high viscosity between $T_g$ and $T_m$ exhibit low $R_{crit}$ and high GFA due to the suppression of crystallization kinetics. Low viscosity between the $T_{br}$ and $T_m$ is a desirable characteristic for the lubrication of steel shell. Therefore having the $T_g$ and $T_{br}$ being as close as possible would favor GFA, as this would indicate a sharp rise in viscosity between these two temperatures, which would not favor crystallization due to the mechanism of diffusion, and therefore resulting in a lower $R_{crit}$ [65].

#### 2.2.1.5 Crystallization tendency

Crystallization tendency is not a reciprocal property of GFA, but a measurement of how readily the glass undergoes crystallization. Glass matrix has higher free energy than crystal lattice, and this is the driving force for its crystallization process. The crystallization process is retarded by high viscosity. Therefore, as temperature rises and viscosity lowers, theoretically crystals would precipitate out of the glass matrix, except for invert glass where crystal matrix is not possible. For mould slags, the crystallization tendency could be understood to be the ratio of the thickness of the slag crystalline film to the thickness of slag glass film in Figure 4 [57, 64].

In the perspective of ternary phase diagrams, greatest tendency of devitrification occurs at compositions at or close to the composition points of binary and ternary compounds, while the lowest tendency occurs at compositions near the liquidus lines (especially close to invariant points). However, this characteristic is difficult to utilize due to the significant shifting of primary fields in a complex chemical system [66].

The crystallization mechanism depends on the nucleation rate and the crystal growth rate, which depend on temperature and cooling rate. The two parameters reach their individual maxima at different temperatures. Therefore a glass composition with a large difference between the two temperatures would have a low crystallization tendency. However, while this has important application to the quenching procedure in glass production, it may not be straightforwardly applicable when discussing the thickness of the slag crystalline film due to the relatively slow cooling rate.

The residence time of a slag in the mould once it had been pushed in between the mould wall and slab by the rim has been reported to be 15-30 min for casting speeds of 0.7 to 1.4 m/min. The temperature drop experienced by the slag from rim to exit from mould is about 350 $^oC$ [23, 67]. This gives an average cooling rate of 12-23 K/min, which is rather small and combined with the long residence time, the production conditions could be considered favorable to the crystallization process.

It has been proposed that the thickness of slag crystalline film is correlated to the reduced glass transition temperature, $T_{rg}$ [68]:

$$T_{rg} = \frac{T_g}{T_m} \tag{20}$$

A slag with relatively close $T_g$ and $T_m$ values is expected to have relatively higher viscosity between these two temperatures, thus lowering the crystallization tendency. Turnbull proposes a simplification for $T_{rg}$ to equal to 2/3 of $T_o$. Turnbull further proposes the following relationship for crystallization rate by drawing a relation to the atomic migration in the melt [69]:

$$J = \frac{A_v}{\mu_o} \exp\left(-\frac{D^* T_{ro}}{T_r - T_{ro}}\right) \exp\left(-\frac{A}{T_r (1-T_r)^2}\right), \tag{21}$$

where $A_v$ is a constant of the order of $10^{32}$ Pa·s/(m$^3$·s), $\mu_o$ is a constant inversely proportional to the molar volume with the unit Pa·s. $D^*$ is the degree of deviation of the system from Arrhenius equation, which is 100 for silica-rich melts. $T_r$ and $T_{ro}$ are temperature dependent parameters:

$$T_r = T/T_m \tag{22}$$

$$T_{ro} = T_o/T \tag{23}$$

A is derived from the change in free energy:

$$A = \frac{16}{3} \frac{\pi \sigma^3}{k \alpha^2 T_m^3 \Delta S_v^2} \tag{24}$$

$\sigma$ is the interphase energy between liquid and nuclei, k is the Boltzmann constant, $\alpha$ is the reduced surface energy, $\Delta S_v$ is the entropy change per volume due to crystallization:

$$\Delta S_v = (S_{crystal} - S_{glass})/V_{crys} \tag{25}$$

where $V_{crys}$ is the volume of the devitrified glass. From equation 21, the first exponential is smaller if the VFT temperature is higher. From equation 24, the value of A is smaller if $T_m$ is smaller, hence reducing the second exponential in equation 21. Therefore from equation 20, slag with relatively low crystallization tendency has a relatively high $T_{rg}$ value.

As mentioned in section 2.2.1.2, DTA and FCT are both used to determine the temperatures at which phase changes take place in the slag. The cooling step is very useful for determining the onset of crystallization temperature, $T_{crys,onset}$, for each of the crystal phase that precipitates out of the liquid slag during defined cooling. The $T_{crys,onset}$ could help identify the paragenesis of phases [70].

DTA and FCT qualitatively describe the phase formation in the slag. Whereas confocal scanning laser microscopy, CSLM, is used to quantify the amount of crystals in order to construct the time-temperature-transformation (TTT) diagram. Mould powder of 5*5*0.4 cm is loaded into the heating chamber, and heated to e.g. 1400 °C. $T_m$ of the slag could be measured by in situ observation during heating. After achieving the maximum temperature, the sample is quenched to defined temperatures, and the crystal growth is observed.

Computer program divides the 5*5 cm screen into millions of grids, and count the number of crystallized grids. Time for 0.5, 50, and 95% crystallization could be acquired for the TTT diagram [71].

Single hot thermocouple technique, SHTT, has the same function as CSLM, but enables the observation of bigger samples. A small amount of the slag is loaded on a U-shaped platinum wire, stretched to uniform depth, and melted as shown in Figure 7a. Some researchers have used SHTT also as a means to measure the melting point of the slag. The slag is quenched to different temperatures, and photos are taken to record the crystal growth. The photos are processed with Photoshop to quantify the crystal growth to generate the TTT diagram [72].

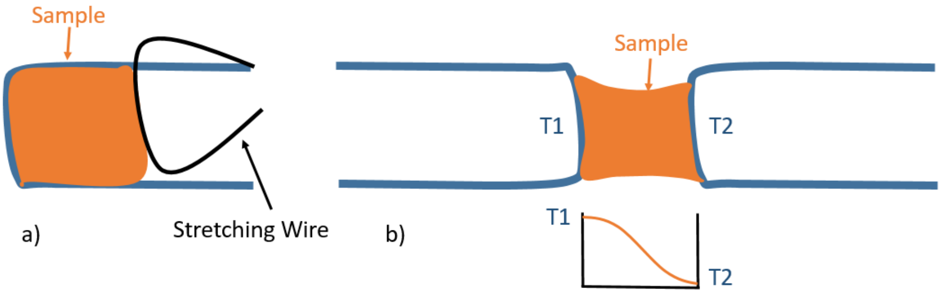

Figure 7. Heating wire design of a)SHTT and b)DHTT [72]

Double hot thermocouple technique, DHTT, is an excellent experimental technique to simulate the working conditions of the mould. A small amount of sample is melted and stretched between two U-shaped wires as shown in Figure 7b. T1 and T2 define the temperature gradient of the slag in the mould. The slag is maintained at this temperature gradient to observe the crystal growth, and photos are taken for analysis. The $T_{crys,onset}$ could be estimated by observing the initial crystal growth site, and correlating its location to the temperature gradient. The crystallization area is measured in dependence of time [73].

### 2.2.1.6. Optical basicity

Lowering the melting point, which could be done by increasing basicity in non-basic slags, lowers the crystallization tendency thermodynamically. This is suggested by equation 21, where a smaller $T_m$ results in a lower crystallization rate, J. However, increasing basicity increases the polarizability of the atoms in the glass matrix, which increases the crystallization tendency mechanistically. This is due to the ions of same element having different electronic polarizability (measured in $Å^3$) in amorphous state from crystalline state. The sum of the electronic polarizability of all the anions and cations in glass matrix (also for slag melts) is larger than those same ions in devitrified state. This is one of the driving forces behind devitrification of the glass. The polarizability of cations follow the same trend as Dietzel's field strength, with decreasing ionic radii and increasing positive charge indicating higher polarizability. This is the reason that boron-rich glass matrix has a lower crystallization tendency than silica-rich glass matrix. For anions, increasing ionic radii and increasing negative charge indicates higher polarizability. This is the reason that $CaF_2$-containing slags can have relatively low devitrification tendency. The oxygens (and fluorine) in the glass matrix must donate its electron density to surrounding cations. When the oxygens donate the maximum possible of electron density, they become non-bridging oxygens. The glass matrix is metastable as long as the number of non-bridging oxygens do not exceed the limit for possible glass network, and the electron density donated by anions readily satisfy the demand of cations. As the number of cations increases, the polarizability of the cations increases in the coulomb field of anions as they compete for more electron density (coordination number increases), and the glass matrix devitrifies [74].

To gauge the overall polarizability of glass and melts (dimensionless), optical basicity concept is developed to describe the chemistry of non-aqueous and non-protonic melts. Optical basicity, $\Lambda_{th}$, is the average charge born by the oxygen atom of the glass matrix, and the concept can be extended to system that includes $CaF_2$. It does not differentiate between bridging oxygen and non-bridging oxygen, and indicates the average polarizability of all the atoms in the glass matrix. Optical basicity is a relatively easy way to calculate parameter when considering the stability of the glass matrix of the slag. The calculation of $\Lambda_{th}$ of the slag is given in the following formula [34]:

$$\Lambda_{\mathrm{th}} = {\sum x_i n_i \wedge_i}\Big/{\sum x_i n_i} \tag{26}$$

where $x_i$ is the molar fraction of oxide i, $n_i$ is the mole of oxygen atom per mole of oxide i, and $\Lambda_i$ is the optical basicity of oxide i. The optical basicity of common commercial glasses is 0.5 to 0.7, while for mould slags it is normally between 0.8 and 1. It could be generalized that for non-basic mould slags, the high basicity of mould slag is associated with the higher amount of alkaline that is necessary for decreasing viscosity, but results in higher crystallization tendency due to the higher average polarizability of the atoms in the glass matrix, as the electronic negativity differences are greater [75].

In the modified NPL viscosity model, Shankar introduces a modified optical basicity, $\Lambda_{new}$, which is the optical basicity of all the basic oxides divided against the basicity of all the acidic oxides [76]:

$$\Lambda_{new} = ({\sum x_i n_i \wedge_i}\Big/{\sum x_i n_i})_{Basic}\Big/({\sum x_i n_i \wedge_i}\Big/{\sum x_i n_i})_{Acidic} \tag{27}$$

This is used to give an elegant solution for the constants A and B in equation 4 (see section 2.2.1.1) for the calculation of viscosity in the VFT-equation:

$$A = -0.3068 \cdot B - 6.7374 \tag{28}$$

$$B = -9.897 \cdot \Lambda_{new} + 31.347 \tag{29}$$

There are different values given for $\Lambda_i$ from literature sources as shown in Table 5, the values that have shown best correlation with crystallization tendency is in the column in the right.

Table 5. Compilation of $\Lambda_i$ values from various sources [21, 77-79]

| | Dietzel's field strength | $\Lambda_i$ accroding to Pauling | $\Lambda_i$ accroding to electron density | $\Lambda_i$ accroding to Slag Atlas | $\Lambda_i$ measured by refractive index | $\Lambda_i$ accroding to energy gap | most used $\Lambda_i$ value |
|---|---|---|---|---|---|---|---|
| $K_2O$ | 0,13 | 1,40 | 1,15 | 1,40 | | | 1,40 |
| $Na_2O$ | 0,19 | 1,15 | 1,10 | 1,15 | | | 1,20 |
| SrO | 0,28 | 1,07 | 1,04 | 1,10 | 1,10 | 1,18 | 1,05 |
| CaO | 0,33 | 1,00 | 1,00 | 1,00 | 1,00 | 0,95 | 1,00 |
| MnO | 0,40-0,49 | 0,59 | 0,95 | 1,00 | | | 0,95 |
| FeO | 0,43 | 0,51 | 0,93 | 1,00 | | | 0,93 |
| MgO | 0,48 | 0,78 | 0,92 | 0,78 | | | 0,85 |
| $Al_2O_3$ | 0,84-0,96 | 0,61 | 0,68 | 0,60 | | | 0,65 |
| $TiO_2$ | 1,04 | 0,61 | 0,64 | 0,61 | 0,96 | 0,91 | 0,65 |
| $B_2O_3$ | 1,34 | 0,42 | 0,42 | 0,42 | 0,43 | | 0,42 |
| $SiO_2$ | 1,57 | 0,48 | 0,47 | 0,48 | 0,48 | 0,52 | 0,48 |

There is a very strong correspondence between the optical basicity and Dietzel's field strength, and as a consequence with the role of the oxide in the glass matrix. SrO has a rather high basicity, while it has a relatively small effect in lowering viscosity and melting point as shown in Table 1. $B_2O_3$ has a particularly low optical basicity, and its addition in the recipe is expected to significantly lower the crystallization tendency.

## 2.3. $CaF_2$-free slag compositions

Some researchers have already tested chemical compositions for $CaF_2$-free mould slags. These can be divided into $B_2O_3$-containing and $B_2O_3$-free slags. The results are summarized below.

### 2.3.1. $B_2O_3$-containing recipes

$B_2O_3$ is an excellent substitute for fluorine, as it increases the superheat degree of the melt, which leads to a loosening of flux structure, resulting in a significant reduction in viscosity [13, 80]. The possible paragenesis of $C_{11}BS_{14}$ is considered an excellent substitute for cuspidine [81]. Boron-containing slag compositions developed by various authors are listed in Table 6.

Table 6. Chemical compositions of F-free Boron containing mould slags in wt% [16, 34, 81-106]

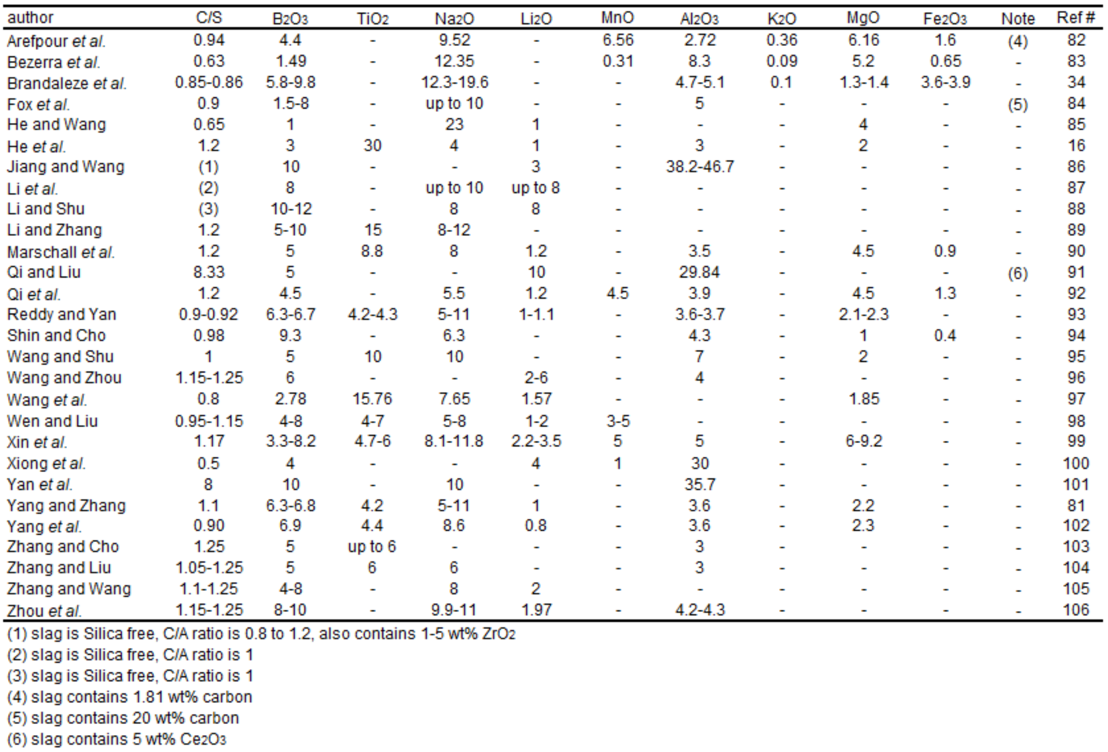

| author | C/S | $B_2O_3$ | $TiO_2$ | $Na_2O$ | $Li_2O$ | MnO | $Al_2O_3$ | $K_2O$ | MgO | $Fe_2O_3$ | Note | Ref # |
|---|---|---|---|---|---|---|---|---|---|---|---|---|
| Arefpour *et al.* | 0.94 | 4.4 | - | 9.52 | - | 6.56 | 2.72 | 0.36 | 6.16 | 1.6 | (4) | 82 |
| Bezerra *et al.* | 0.63 | 1.49 | - | 12.35 | - | 0.31 | 8.3 | 0.09 | 5.2 | 0.65 | - | 83 |
| Brandaleze *et al.* | 0.85-0.86 | 5.8-9.8 | - | 12.3-19.6 | - | - | 4.7-5.1 | 0.1 | 1.3-1.4 | 3.6-3.9 | - | 34 |
| Fox *et al.* | 0.9 | 1.5-8 | - | up to 10 | - | - | 5 | - | - | - | (5) | 84 |
| He and Wang | 0.65 | 1 | - | 23 | 1 | - | - | - | 4 | - | - | 85 |
| He *et al.* | 1.2 | 3 | 30 | 4 | 1 | - | 3 | - | 2 | - | - | 16 |
| Jiang and Wang | (1) | 10 | - | - | 3 | - | 38.2-46.7 | - | - | - | - | 86 |
| Li *et al.* | (2) | 8 | - | up to 10 | up to 8 | - | - | - | - | - | - | 87 |
| Li and Shu | (3) | 10-12 | - | 8 | 8 | - | - | - | - | - | - | 88 |
| Li and Zhang | 1.2 | 5-10 | 15 | 8-12 | - | - | - | - | - | - | - | 89 |
| Marschall *et al.* | 1.2 | 5 | 8.8 | 8 | 1.2 | - | 3.5 | - | 4.5 | 0.9 | - | 90 |
| Qi and Liu | 8.33 | 5 | - | - | 10 | - | 29.84 | - | - | - | (6) | 91 |
| Qi *et al.* | 1.2 | 4.5 | - | 5.5 | 1.2 | 4.5 | 3.9 | - | 4.5 | 1.3 | - | 92 |
| Reddy and Yan | 0.9-0.92 | 6.3-6.7 | 4.2-4.3 | 5-11 | 1-1.1 | - | 3.6-3.7 | - | 2.1-2.3 | - | - | 93 |
| Shin and Cho | 0.98 | 9.3 | - | 6.3 | - | - | 4.3 | - | 1 | 0.4 | - | 94 |
| Wang and Shu | 1 | 5 | 10 | 10 | - | - | 7 | - | 2 | - | - | 95 |
| Wang and Zhou | 1.15-1.25 | 6 | - | - | 2-6 | - | 4 | - | - | - | - | 96 |
| Wang *et al.* | 0.8 | 2.78 | 15.76 | 7.65 | 1.57 | - | - | - | 1.85 | - | - | 97 |
| Wen and Liu | 0.95-1.15 | 4-8 | 4-7 | 5-8 | 1-2 | 3-5 | - | - | - | - | - | 98 |
| Xin *et al.* | 1.17 | 3.3-8.2 | 4.7-6 | 8.1-11.8 | 2.2-3.5 | 5 | 5 | - | 6-9.2 | - | - | 99 |
| Xiong *et al.* | 0.5 | 4 | - | - | 4 | 1 | 30 | - | - | - | - | 100 |
| Yan *et al.* | 8 | 10 | - | 10 | - | - | 35.7 | - | - | - | - | 101 |
| Yang and Zhang | 1.1 | 6.3-6.8 | 4.2 | 5-11 | 1 | - | 3.6 | - | 2.2 | - | - | 81 |
| Yang *et al.* | 0.90 | 6.9 | 4.4 | 8.6 | 0.8 | - | 3.6 | - | 2.3 | - | - | 102 |
| Zhang and Cho | 1.25 | 5 | up to 6 | - | - | - | 3 | - | - | - | - | 103 |
| Zhang and Liu | 1.05-1.25 | 5 | 6 | 6 | - | - | 3 | - | - | - | - | 104 |
| Zhang and Wang | 1.1-1.25 | 4-8 | - | 8 | 2 | - | - | - | - | - | - | 105 |
| Zhou *et al.* | 1.15-1.25 | 8-10 | - | 9.9-11 | 1.97 | - | 4.2-4.3 | - | - | - | - | 106 |

(1) slag is Silica free, C/A ratio is 0.8 to 1.2, also contains 1-5 wt% $ZrO_2$
(2) slag is Silica free, C/A ratio is 1
(3) slag is Silica free, C/A ratio is 1
(4) slag contains 1.81 wt% carbon
(5) slag contains 20 wt% carbon
(6) slag contains 5 wt% $Ce_2O_3$

Some of the compositions have been developed for steel grades. However, most of these contain $Li_2O$ due to its excellence at reducing viscosity. A slag containing 1% $Li_2O$ has been tested for low carbon and medium carbon steel, which showed that between 5-11 wt% $Na_2O$ contents the crystallization tendency is satisfactory [93]. For slags developed for medium carbon steel, results showed that $Li_2O$ hinder the paragenesis of CS, $C_2AS$, and $Ca_{11}Si_4B_2O_2$, while promoting the paragenesis of low temperature phase $C_{11}BS_{14}$ [96]. Zhou *et al.* have developed slags for medium carbon steel that more than double the glass film layer when compared to the $CaF_2$-containing slag; the crystallization tendency is drastically increased when $Li_2O$ content is increased to 3 wt%. The main phases precipitated are $C_{11}BS_{14}$ and $C_{14}M_2S_4$ [106]. A $Li_2O$-free slag has been industrially tested for steel in the 0.6 wt% carbon range with success [83]. A slag containing less than 2 wt% $Li_2O$ has been developed for the continuous casting of peritectic steel [98].

Some compositions have been developed for special steel types or purposes. A substitute for a reference powder used in the steel industry has been tested, exhibiting better lubricating ability [82]. Fox *et al.* have industrially tested slag recipes for billet casting, and found that $B_2O_3$ has a significant effect on lowering $T_{br}$ [84], which agreed with the findings of Zhang and Wang [105]. Qi and Liu have developed a slag composition for Ce-bearing heat resistant steel, which is required to have very low $SiO_2$ content to avoid chemical reaction with the steel [91]. For high-Al steel, Xin *et al.* have given a range of recipes that exhibit low viscosity and satisfactory heat flux [99]. Xiong *et al.* have proposed a slag composition for the casting of high Al-TRIP steel [100].

Several compositions are clearly developed with a reasonable target viscosity and $T_m$ in mind. Marschall *et al.* have tested a composition with viscosity below 1 poise at 1300 °C [90]. Qi *et al.* have reported of a slag with viscosity of 2.7 poise at 1300 °C [92]. Several other F-free $B_2O_3$-containing slag compositions with viscosities of 2-3 poise at 1300 °C have been developed [34]. Shin and Cho have given a shear thinning slag composition [94].

Due to the usefulness of $TiO_2$ as a network former that is associated with not so significant increase in viscosity, the phase paragenesis in the CBS-$TiO_2$ system is of interest. He and Wang have examined the phase paragenesis of CTS and NCS chemical system, and showed that with increasing proportion of perovskite, critical cooling rate decreases [85]. The phase paragenesis in high-$TiO_2$ slag of the CTS system during industrial application has been investigated. The major phase is perovskite, and formation of CTS, TiN, Ti(C,N) are possible [16, 97]. Zhang and Liu have developed compositions showing lower crystallization tendencies than common industrial slags, and have found that its $TiO_2$ contents could be replaced by 2 wt% of $ZrO_2$, which removes the paragenesis of perovskite [104].

The glass matrix structure in a high-$TiO_2$-containing slag in relation to sodium and boron contents has been investigated. The boron is mostly in the $BO_3$ triangular configuration, but rising $Na_2O$ contents convert $BO_3$ triangles to $BO_4$ tetrahedrals. Rising $Na_2O$ and $B_2O_3$ contents both increase the number of NBO bonds. However, rising boron content increase the number of Si and Ti in $Q^3$ configuration, while rising sodium content has the opposite effect [89]. Zhang and Cho have investigated the volatility of $B_2O_3$ and $Na_2O$ content, which is increased with increasing $TiO_2$ content due to decrease in viscosity, and increased with increasing $ZrO_2$ content due to solid particles acting as nucleating site of bubble formation [103]. Wang and Shu have examined the viscosity of NTBS system by varying the $Na_2O$, $TiO_2$ and $B_2O_3$ contents of an industrial slag, and showed that experimental results agree with modified Riboud model to within 7% [95].

The phase paragenesis in the CASB chemical system is of interest. With rising $B_2O_3$ contents, the major phase shifts from $C_2AS$ to $C_3B$, and crystallization could not be observed above 15 wt% $B_2O_3$ [101]. Yang and Zhang have shown that the major phase precipitated shifts from CS to $C_{11}BS_{14}$ and $C_2MS_2$ with increasing C/S ratio, which is desirable. However, the critical cooling rate increases when C/S ratio is larger than one, which adversely affects GFA [81]. Wang *et al.* have shown that the onset of crystallization temperature of the slag is correlated to the C/S ratio, but it has no influence on the volatility of $Na_2O$ and $B_2O_3$ [97]. For $SiO_2$-free slags, the crystallization of $C_3B$ is promoted by rising boron content, and the crystallization of CA is promoted by rising alkali contents [87]; with rising $LiO_2$ content, the crystallization of the main phase $C_3B$ remains unchanged, but the other main phase shifts from $C_3A$ to $LiAlO_2$ [88]. As can be seen in Table 6, the boron content from various authors is concentrated within 4-10 wt% range. As a summary in Table 7 the phase paragenesis in CABS system is listed. The phase formations are given for slags containing 3 wt% $Al_2O_3$, 7 wt% $Na_2O$, 2 wt% $TiO_2$, and 3 wt % MgO.

Table 7. Phase formation in the CABS system [109, 110]

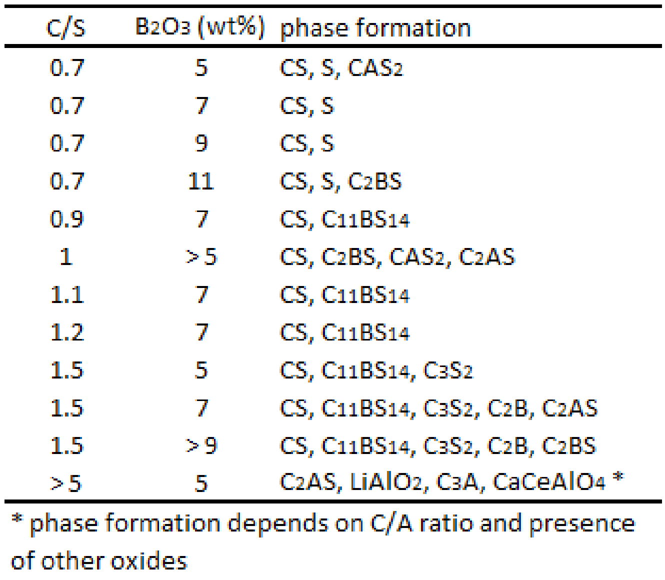

| C/S | $B_2O_3$ (wt%) | phase formation |
|---|---|---|
| 0.7 | 5 | CS, S, $CAS_2$ |
| 0.7 | 7 | CS, S |
| 0.7 | 9 | CS, S |
| 0.7 | 11 | CS, S, $C_2BS$ |
| 0.9 | 7 | CS, $C_{11}BS_{14}$ |
| 1 | >5 | CS, $C_2BS$, $CAS_2$, $C_2AS$ |
| 1.1 | 7 | CS, $C_{11}BS_{14}$ |
| 1.2 | 7 | CS, $C_{11}BS_{14}$ |
| 1.5 | 5 | CS, $C_{11}BS_{14}$, $C_3S_2$ |
| 1.5 | 7 | CS, $C_{11}BS_{14}$, $C_3S_2$, $C_2B$, $C_2AS$ |
| 1.5 | >9 | CS, $C_{11}BS_{14}$, $C_3S_2$, $C_2B$, $C_2BS$ |
| >5 | 5 | $C_2AS$, $LiAlO_2$, $C_3A$, $CaCeAlO_4$ * |

* phase formation depends on C/A ratio and presence of other oxides

As can be seen in Table 7, a C/S ratio of 0.7 in tandem with low $B_2O_3$ content results in the formation of anorthite, which is undesirable due to the devitrification tendency of anorthite. At C/S ratio of exactly 1, anorthite is a major phase across all $B_2O_3$ contents, which may suggest that this C/S ratio should be avoided entirely. As C/S ratio rises above 1, $C_{11}BS_{14}$ becomes the main phase, which has a low liquidus temperature. This is a desirable phase as it has been suggested as an excellent substitute for cuspidine. As the C/S ratio increases above 1.2, the phase formation becomes too complicated and therefore less desirable. The melting point is expected to reach a minimum at C/S ratio between 1.1 and 1.2 for the CABS system. However, with a $Li_2O$ content of 1 wt% this ratio is shifted up to between 1.2 and 1.3 [111]. At C/S ratio of 1.7, the paragenesis of $C_3A_2BS_8$ and $C_6A_{12}BS_8$ are possible, which is also considered a good substitute for cuspidine [13]. However, for slags containing less than 2 wt% $B_2O_3$, no paragenesis of ternary phases within the CBS system will take place [108]. At $B_2O_3$ content above 15 wt%, the crystallization tendency is very low, but the precipitation of $CaB_2O_4$ is possible [112].

For the slags with very high C/S ratios, the mineralogical composition is determined by the C/A ratio. At C/A ratios below 1, the primary phase is $C_2AS$. At C/A ratio above 1.5, the primary phase is $C_3A$. The C/A ratio of such low-$SiO_2$-containing slags are often controlled between 1.7 and 1.8, due to the efficiency of removing inclusion bodies [113]. In the presence of $LiO_2$, the paragenesis of $LiAlO_2$ having a high $T_m$ will take precedence over the phases of the CAS system [81]. Jiang and Wang have shown that the crystallization tendency is highest at C/A ratio of 1 for low-$SiO_2$-containing slags [86].

$Na_2O$ content has a significant effect on the phase formation and GFA of the CABS system. Rising $Na_2O$ content enlarges the primary field of $C_{11}BS_{14}$ at the expense of CS primary field, which is desirable. However, rising $Na_2O$ content also encourages the paragenesis of $CaTiO_3$ and $C_2MS_2$. $CaTiO_3$ has a high $T_m$, and compositions within the $C_2MS_2$ primary field are associated with lower GFA due to increasing devitrification tendency [114]. It has been suggested that the paragenesis of $CaTiO_3$ and $C_2MS_2$ could be restrained by limiting the content of $TiO_2$ to roughly within 4 wt%, and MgO within 3 wt%. However, a minimum in viscosity could be expected at $TiO_2$ contents of around 6 wt% [115]. At $Na_2O$ content above 9 wt%, paragensis of $NC_2S_3$ is possible, which is not undesirable as it is another possible substitute for cupsidine. At above 11 wt% $Na_2O$, the primary field of CS disappears completely, which is desirable. However, it has been suggested that with a too high sodium content the GFA decreases rapidly [103]. It also decreases the amount of MgO and $Al_2O_3$ that can exist as solid solutions within the crystal lattices, and results in the paragenesis of spinel [116].

### 2.3.2. $B_2O_3$-free mould fluxes

With regards to steel quality, boron-free slag compositions are of interest. $TiO_2$, RO, and $R_2O$ are possible substitutes for $CaF_2$. Several authors have proposed possible compositions as shown in Table 8.

Table 8. Chemistry of F-free Boron-free slag compositions in wt% [82, 83, 107, 117-126]

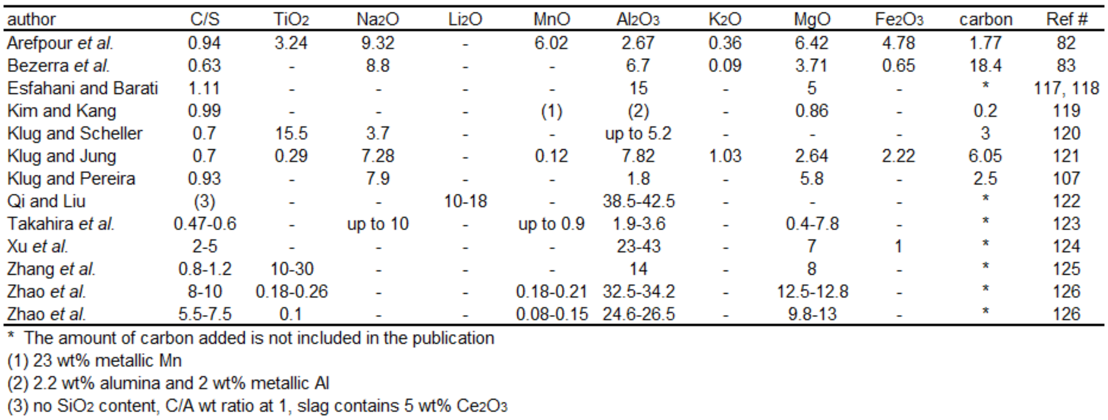

| author | C/S | $TiO_2$ | $Na_2O$ | $Li_2O$ | MnO | $Al_2O_3$ | $K_2O$ | MgO | $Fe_2O_3$ | carbon | Ref # |
|---|---|---|---|---|---|---|---|---|---|---|---|
| Arefpour *et al.* | 0.94 | 3.24 | 9.32 | - | 6.02 | 2.67 | 0.36 | 6.42 | 4.78 | 1.77 | 82 |
| Bezerra *et al.* | 0.63 | - | 8.8 | - | - | 6.7 | 0.09 | 3.71 | 0.65 | 18.4 | 83 |
| Esfahani and Barati | 1.11 | - | - | - | - | 15 | - | 5 | - | * | 117, 118 |
| Kim and Kang | 0.99 | - | - | - | (1) | (2) | - | 0.86 | - | 0.2 | 119 |
| Klug and Scheller | 0.7 | 15.5 | 3.7 | - | - | up to 5.2 | - | - | - | 3 | 120 |
| Klug and Jung | 0.7 | 0.29 | 7.28 | - | 0.12 | 7.82 | 1.03 | 2.64 | 2.22 | 6.05 | 121 |
| Klug and Pereira | 0.93 | - | 7.9 | - | - | 1.8 | - | 5.8 | - | 2.5 | 107 |
| Qi and Liu | (3) | - | - | 10-18 | - | 38.5-42.5 | - | - | - | * | 122 |
| Takahira *et al.* | 0.47-0.6 | - | up to 10 | - | up to 0.9 | 1.9-3.6 | - | 0.4-7.8 | - | * | 123 |
| Xu *et al.* | 2-5 | - | - | - | - | 23-43 | - | 7 | 1 | * | 124 |
| Zhang *et al.* | 0.8-1.2 | 10-30 | - | - | - | 14 | - | 8 | - | * | 125 |
| Zhao *et al.* | 8-10 | 0.18-0.26 | - | - | 0.18-0.21 | 32.5-34.2 | - | 12.5-12.8 | - | * | 126 |
| Zhao *et al.* | 5.5-7.5 | 0.1 | - | - | 0.08-0.15 | 24.6-26.5 | - | 9.8-13 | - | * | 126 |

* The amount of carbon added is not included in the publication
(1) 23 wt% metallic Mn
(2) 2.2 wt% alumina and 2 wt% metallic Al
(3) no $SiO_2$ content, C/A wt ratio at 1, slag contains 5 wt% $Ce_2O_3$

$TiO_2$ and MgO have been investigated as substitutes of boron in order to decrease viscosity, and the results show that the principle factor affecting viscosity is the degree of polymerization of Si [125]. The glass morphology in dependence of C/S ratios show a linear relationship between the decadic log of critical cooling rate and the decadic log of the nose temperature in the TTT diagram [117,118]. The density of low silica-content CMAS slags increases along with increase in optical basicity [124].

Several boron-free slags have been tested industrially for specific steel types. One slag has been industrially tested for low carbon steel casting, demonstrating similar properties as the F-bearing slag it intended to replace with only half the slag consumption per ton of steel. This composition shows no crystallization tendency whatsoever [107]. Kim and Kang have devised a slag composition for high-Mn-high-Al steel [119]. Klug and Scheller have developed a $TiO_2$-rich slag to match the heat flux of classic $CaF_2$-bearing flux with good results [120]. Klug and Jung have industrially tested a recipe for Cr-Mo-Ni bearing billet casting [121]. Qi and Liu have given a silica-free slag composition for the casting of $Ce_2O_3$-bearing steel [122]. Takihara *et al.*

has developed a slag composition that has $NC_2S_3$ as the crystallization target phase [123]. Zhao *et al.* has developed two ranges of low-$SiO_2$ slag for the casting of high-strength low-alloy ship plates [126]. Arefpour and Bezerra have developed boron-free counterparts to their boron-containing compositions listed in Table 6 [82, 83, 107].

## 3. Experimental Methods

In this section the process in which promising compositions are arrived and the experimental methods for testing the slags are described.

### 3.1. Chemical compositions

The ternary phase diagrams of glass-forming systems are consulted to have a reasonable starting point for a chemical composition. Then, to this composition several oxides are introduced. The melting points and viscosities of chemical compositions are estimated with the program FactSage.

C/S ratio is a significant determinant of the basicity of the slag. $Al_2O_3$ is an inexpensive alternative network former to $SiO_2$. Therefore, the CAS chemical system is chosen to form the basis of the slag chemical composition. In the CAS phase diagram shown in Figure 8, the lowest invariant points occur at 1170 °C and 1265 °C. So the compositions lying within the composition triangles S-CS-$CAS_2$ and CS-$CAS_2$-$C_2AS$ are promising. Considering the high viscosity associated with high $SiO_2$ and $Al_2O_3$ contents, and in order to arrive at the eutectic point at 1170 °C, the chemical composition enclosed within the red boundary in Figure 3 is likely to yield slags with both relatively low viscosity and melting point. For this region, the C/S ratio is between 0.76 and 0.88, which could be proposed as the boundaries for the slag composition. In this region, an exception to the generalization of Table 3 could already be observed. From point 1 to point 2 in Figure 3, with rising $Al_2O_3$ contents, the melting point of the composition actually decreases, although a significant corresponding increase in viscosity is expected. It is also possible that the 1335 °C invariant point of $C_3A$-$C_{12}A_7$-$C_2S$ and 1350 °C invariant point of CA-$C_{12}A_7$-$C_2S$ are also reasonable starting points for slag compositions.

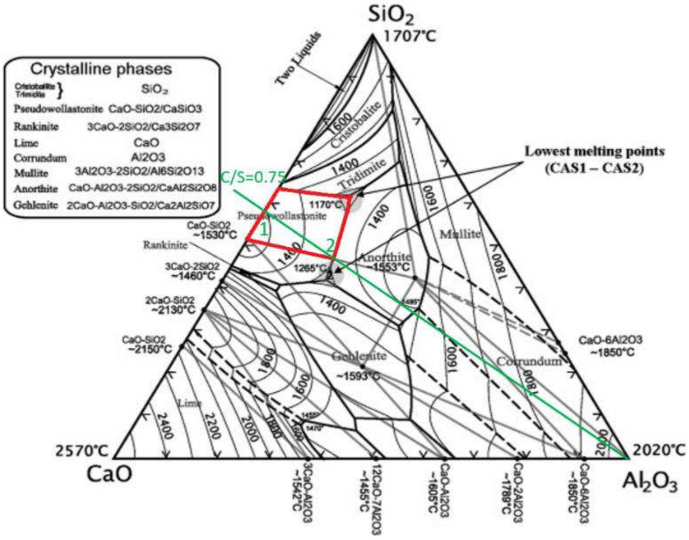

Figure 8. CAS phase diagram in weight scale [127].

MgO could lower viscosity of the slag melt; due to the alkaline mix effect, it being added at a ratio to CaO would maximize this effect. This ratio has to be determined with FactSage, and should be different for different composition triangles in the chemical systems. The invariant points in CMS and MAS phase diagrams are all rather high at least 1331 °C (trydimite-wollastonite-$CMS_2$) and 1355 °C (trydimite-MS-$M_2A_2S_5$). However, it is reasonable to assume that these invariant points can be brought much lower than 1250 °C in a multi-component system.

$TiO_2$ is a good network-former substitute for as the resulting glass melt will have lower viscosity, and is likely to be present in a successful composition, i.e. up to 20 wt%. In the CaO-$TiO_2$-$SiO_2$ phase diagram, a relatively low invariant point exists at 1318 °C (trydimite-CS-sphene), which makes its corresponding composition triangle a chemical region of interest. Being within this composition also avoids the paragenesis of perovskite, $CaTiO_3$, which has a higher melting point than sphene [128]. However, in the presence of significant amounts of MgO and alumina, this low-temperature invariant point no longer exists, as the paragenesis of sphene is no longer possible. In Figure 9a, the pseudo-ternary CaO-$TiO_2$-$SiO_2$ phase diagram with 5 wt% MgO and 10 wt% $Al_2O_3$ is shown. The primary fields have shifted significantly. There is no longer a primary field of sphene due to the expansion of the primary field of perovskite and the paragensis of a solid solution between $C_2MS$ and $C_2AS$. The invariant point marked with 1 has a melting point of 1250 °C. Due to the direction of the liquidus lines, compositions close to the invariant point 2 should have a lower melting point than point 1. Point 1 has a C/S ratio of 0.88, and point 2 has a C/S ratio of 0.76. This gives a reasonable range of C/S ratio for a composition with a low melting point and containing at least 5 wt% $TiO_2$. In Figure 9b, the pseudo-ternary CMS phase diagram with 10 wt% $TiO_2$ and 10 wt% $Al_2O_3$ is shown. Here the primary field of perovskite has expanded at the expense of the CS primary field, which is desirable as perovskite has a lower melting point compared to CS. The direction of the isotherms in the primary field of perovskite indicates that rising MgO content has only marginal effect on $T_m$. In both pseudo-ternary phase diagrams, the melting of CS becomes incongruent. Therefore the paragenesis of CS is suppressed when slag cools down in disequilibrium [129, 130].

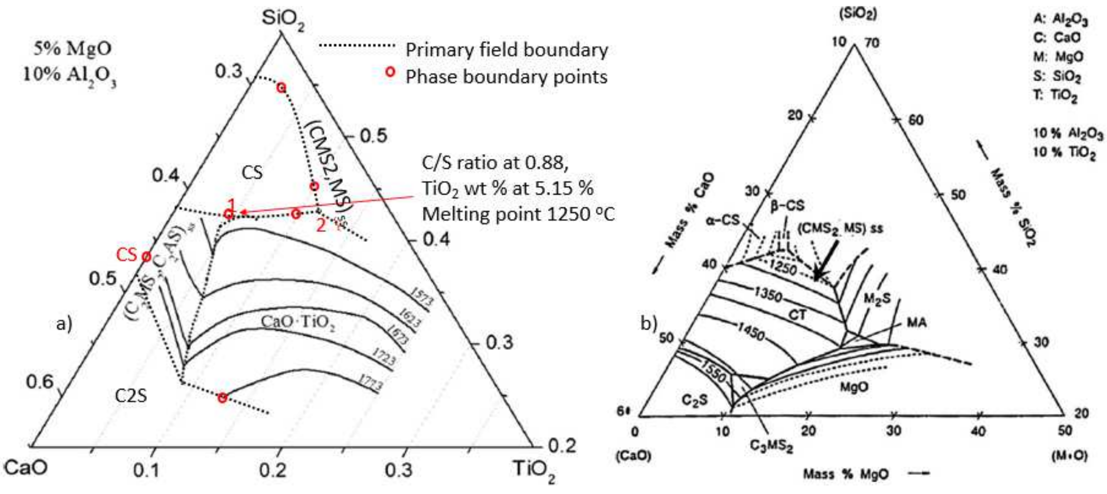

Figure 9. a) pseudo-ternary CTS system in weight scale (temperature in Kelvin) [129]; b) pseudo-ternary CMS system in weight scale (temperature in °C) [130]

$Na_2O$ is a network modifier that can greatly reduce the viscosity and $T_m$ of the slag. The paragenesis of ternary compounds in the NAS system, albeit and nepheline, is desirable due to their low melting point [131]. The eutectic point of $SiO_2$ and CS is reduced from 1436 °C to 1300 °C with the addition of 10 wt% $Na_2O$. However, rising content of $Na_2O$ does not necessarily equate to lower $T_m$ due to the possible paragenesis of high temperature phase. As can be seen in Figure 10, the red lines mark the proposed C/S ratio between 0.88 and 0.76 according to Figure 8. Compositions lying in composition triangle CS-$NC_3S_6$-$NC_2S_3$ have an invariant point at 1025 °C. As $Na_2O$ content rises, the chemical composition arrives within the composition triangle CS-$C_3S_2$-$NC_2S_3$, which has an invariant point above 1250 °C. Only when the $Na_2O$ content rises enough to enter the composition triangle $C_3S_2$-$NC_2S_3$-$NC_2S_2$, invariant point decreases. The sodium content of the slag most likely fall within one of these composition triangles, and thus the composition triangle CS-$C_3S_2$-$NC_2S_3$ should try to be avoided [132].

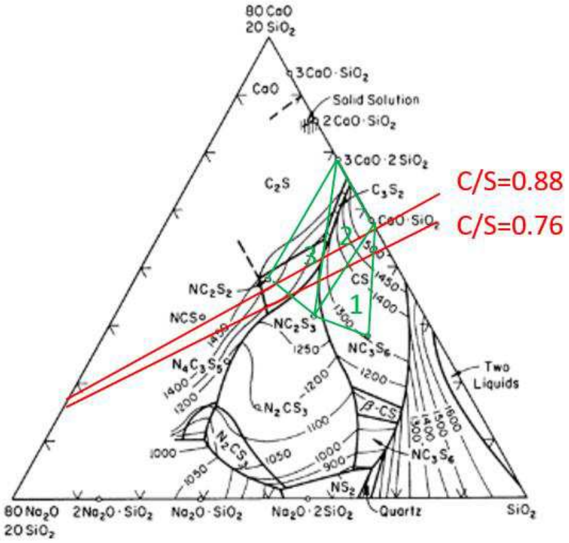

Figure 10. NCS phase diagram [132].

$K_2O$ could lower the viscosity, and should be introduced to the system at a ratio to $Na_2O$ to maximize this effect due to the alkali mix effect. This ratio could be calculated with FactSage. $K_2O$ also has the effect to significantly reduce all eutectic points. The eutectic point of $SiO_2$ and CS is reduced from 1436 °C to 1300 °C with the addition of 6 wt % $K_2O$. None of the ternary compounds in the KAS system has a high $T_m$. This is the same for the KCS system except for $K_2CaSiO_4$. However, the existence of this compound is actually questionable. The most possibly relevant invariant point lies within the conjugation triangle of CS-S-$KC_2S_6$ (1090 °C) [133].

$B_2O_3$ has the ability of significantly reducing the eutectic temperatures and viscosity of the melt. In the $CaO$-$SiO_2$-$B_2O_3$ ternary system, the invariant point of CS-$SiO_2$-$CaB_2O_4$ is only 1000 °C. As a result, boron-containing slags typically exhibit low $T_m$ [134, 135].

## 3.2 Evaluation of the glass formation ability

It is useful to examine the limits of the chemical system by consulting the known glass formation regions within well-investigated phase diagrams. The glass formation region without super-quenching in the CAS system is marked in Figure 11. The C/S ratios between 0.76 and 0.88 mark the composition range that correspond to low liquidus points. The devitrification process involves the precipitation of anorthite, and the region roughly corresponds to the primary field of anorthite. The devitrification is most severe close to the representing point of anorthite. Below 7.5 wt% $Al_2O_3$, the glass shows no devitrification, and therefore has a relatively low crystallization tendency. However, this composition region has higher viscosity than desired for mould fluxes. Significant addition of alkalis to the chemical system is required [136, 137].

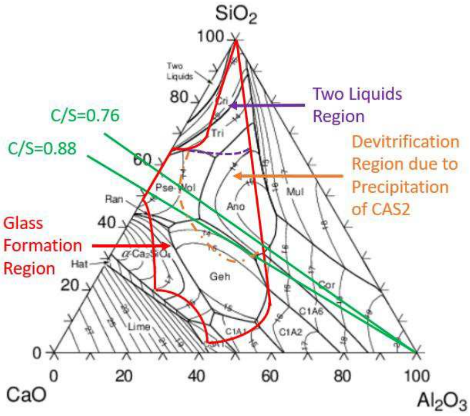

Figure 11. Glass formation region in the CAS system

The NCAS system is well studied thanks to application for the soda lime silica glass and glaze industry. With the addition of significant quantities of alkalis the glass formation region shifts significantly. One example where 30 wt% of lime is replaced by soda is shown in Figure 12. The glass formation region shifts significantly due to the high basicity of soda. The chemical compositions with C/S ratio below 0.82 no longer facilitate glass formation. It has also been reported that in this system compositions with an A/S weight ratio roughly around 0.1 exhibit low viscosities. Substituting $Na_2O$ and $K_2O$ mole for mole does not shift the glass formation region [134, 135, 138].

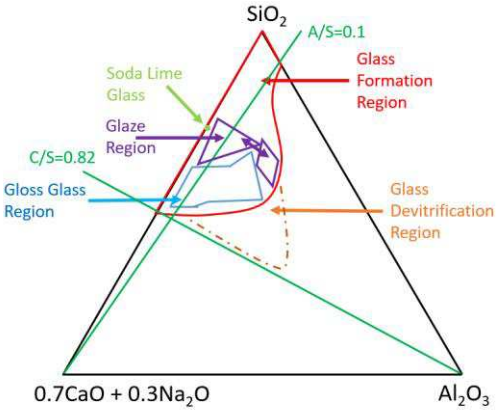

Figure 12. Glass formation region within the NCAS system

Another chemical system is considered using $B_2O_3$ as one of the main glass network formers. The viscosities of commercial borosilicate glass melts are around 12-15 poise at 1300 °C, which is slightly lower than that of the commercial container glass (15-18 poise at 1300 °C) [139]. The glass formation region in the $Na_2O$-$SiO_2$-$B_2O_3$ system is shown in Figure 13a. The two liquids region involves a not so well understood process during quenching when one part of the melt solidifies into glass first, resulting in a phase separation that leads to two different glass matrixes being present at the same time [140]. However, this phenomenon does not adversely affect GFA. The ideal weight ratio of $Na_2O/B_2O_3$ is 16/84 [141]. As the boron oxide content of the melt increases, alumina needs to be added to give a stabilizing effect to lessen the evaporation of boron. Therefore if the composition falls within the vycor glass region, the composition must be doped with alumina. When alumina is a main constituent of the slag, then the glass devitrification region in the NAS system as shown in Figure 13b becomes of concern. While nepheline is a desirable phase for the NCAS system, it is required that for the NABS system, the S/(N+A+S) weight ratio should be above 0.62, or nepheline will rapidly crystalize. This ratio is referred to as nepheline discriminator, ND [142]. As can be seen in Figure 13a, all of the vycor glass region would observe the nepheline discriminator if a small amount of alumina is added. As borosilicate compositions are nonbasic, alumina will act as a network modifier. In high-alumina borosilicate slag nepheline is the major crystallized phase [143].

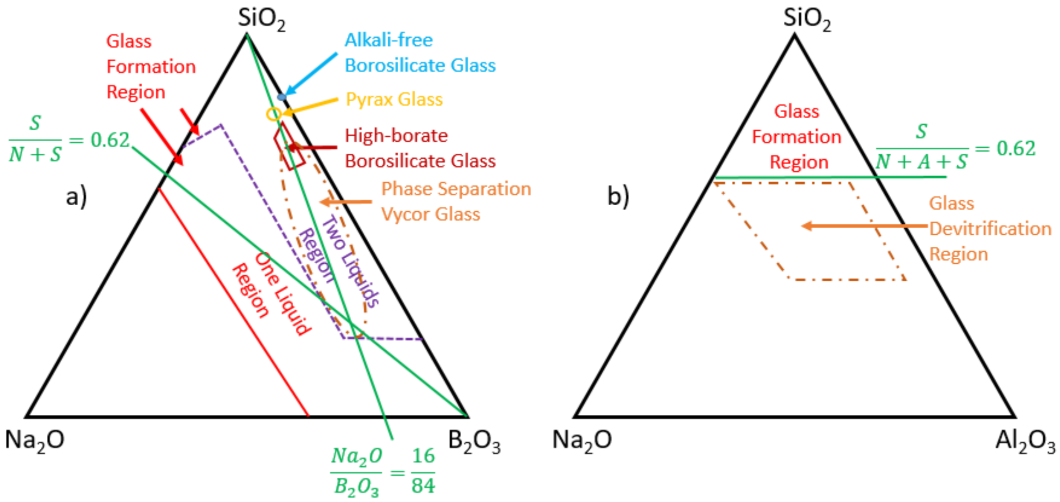

Figure 13. a) Glass formation region for NBS system and b) the devitrification region for the NAS system (both in weight scale)

Commercial high-MgO boroaluminate glasses within the MgO-$B_2O_3$-$Al_2O_3$ system give another possibility for slag composition. The glass formation region is shown in Figure 14. It is not necessary for this glass system to observe the $Na_2O/B_2O_3$ ratio of 16/84, but the nepheline discriminator should be observed if both silica and $Na_2O$ are present at more than 5 molar percent. The chemical composition of commercial alkaline-rich boroaluminate glass encompasses the one liquid region, which is known for very low viscosity (4-8 poise at 1300 °C). This is a nonbasic glass as the moles of nonbasic oxides still exceed that of the basic oxides. Therefore $Al_2O_3$ behaves as a network modifier [144].

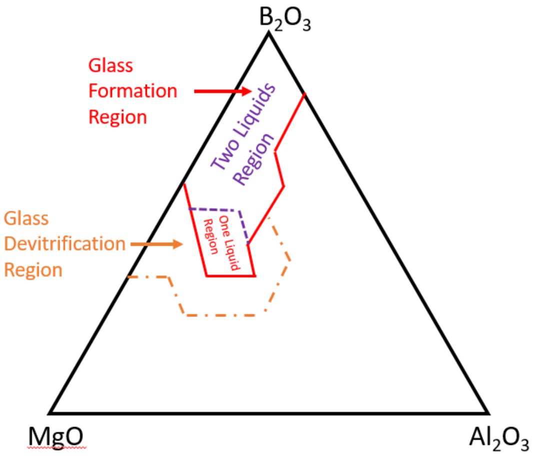

Figure 14. Glass formation region for MAB system (molar scale)

### 3.3. Development of new slag compositions

In the previous sections the range of possible chemical compositions has been narrowed. Two chemical systems are proposed. The first system, hereby called the soda-lime system, lies in the primary field of pseudowollastonite in the CAS diagram with a C/S ratio of 0.82 to 0.76 as shown in Figure 8. The alumina content of the slag should be below 7.5 wt% to avoid devitrification by the precipitation of anorthite and too high viscosity values. MgO content should be restricted to avoid the primary field of $C_2MS_2$, which increases the crystallization tendency of the slag. $Na_2O$ will be a major constituent of the compositions, and N/K ratio should be fixed to minimize viscosity due to the alkali mix effect. $B_2O_3$ could be included, with its contents likely between 1 to 4.4 wt%, as this has been stated as the most cost effective content for reducing viscosity [33]. The second system, hereby called the high-alkaline boroaluminate slag system, lies in the one-liquid region of the MAB system in Figure 14. The nepheline discriminator needs to be observed.

#### 3.3.1. Soda-lime-silicate system

With the chemical compositions having been a narrowed down range, FactSage7.2 is used to calculate the melting point and viscosity at 1300 °C within these limits. Calculation is done in unit of moles, as this is more intuitive when thinking of the changes in glass matrix network. For the convenience of FactSage calculation, the slag is viewed as a main body made up of CaO and $SiO_2$, with the other oxides added in as a modification to the glass matrix at a certain ratio to $SiO_2$. The $SiO_2$ content is set at 400 moles, and CaO content at 343 moles. The numbers are rather large in order to facilitate operation. For lowering the degrees of freedom, $Al_2O_3$ and $B_2O_3$ are first excluded from this part of the calculation.

A suitable possible section calculated with FactSage for the proposed slag system is given in Figure 15. The N/K molar ratio was calculated to be 3 to maximize the alkali mixing effect. The $MgO/TiO_2$ molar ratio is set 2/3, as through trial and error this ratio was found to produce a linear relationship for viscosity in terms of alkali versus earth alkaline contents (at least according to FactSage). In combination with the observed liquidus temperature lines, a suitable area for new slag composition is defined. The chemical compositions are listed in Table A1 of Appendix A.

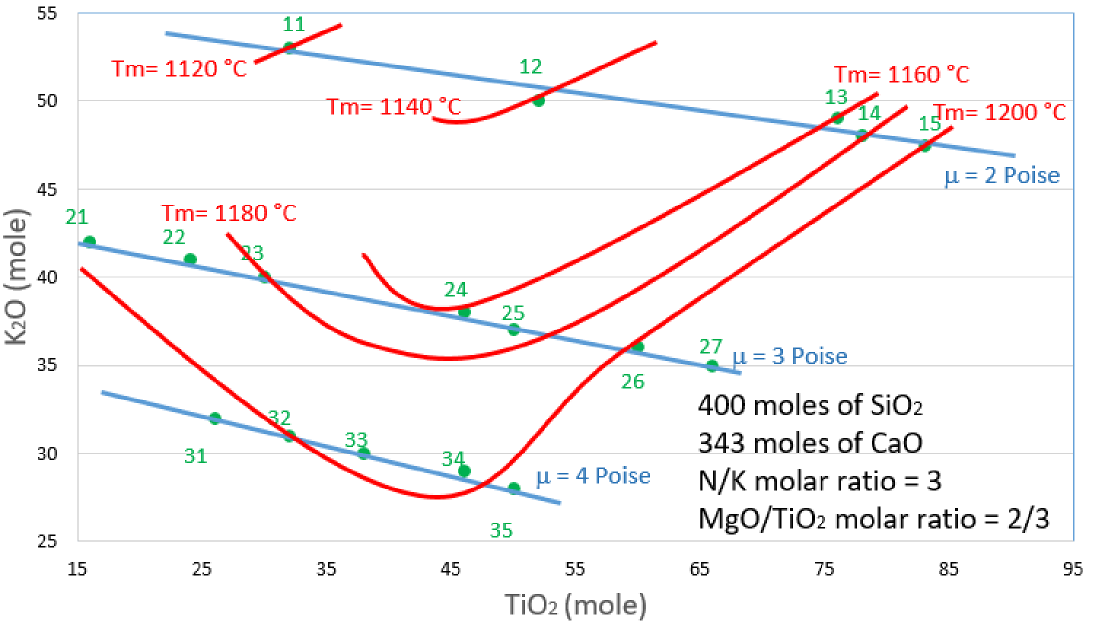

Figure 15. Liquidus temperatures and viscosities at 1300 °C for slags within the system $Na_2O$-$K_2O$-$CaO$-$MgO$-$TiO_2$-$SiO_2$

The chemical composition at point 24 in Figure 15 (serialized as E-2018-A002) has a melting point of 1160 °C and a viscosity of 3 poise at 1300 °C according to FactSage. Because the composition of A002 resembles a commercial soda lime glass, this system is called the soda-lime silicate slag system in this thesis.

With the introduction of $Al_2O_3$, $B_2O_3$, FeO, and MnO into the chemical system as molar ratios to $SiO_2$, further chemical compositions are calculated using FactSage based on E-2018-A002 to all have melting point at 1160 ± 1 °C, and viscosity of 0.299 ± 0.001 PaS at 1300 °C. For example, when alumina is introduced into the system, the $T_m$ and viscosity of the slag at 1300 °C rises, which is brought down by adding N and K at a molar ratio of 3. Adding MgO and $TiO_2$ at a molar ratio of 2/3 decreases viscosity but increases $T_m$, which allows the new compositions to have the same $T_m$ and viscosity according to FactSage.

### 3.3.2. High-alkaline boroaluminate slag system

In this system, alumina still has an effect in increasing viscosity and melting point of the glass. Therefore the starting point for generating a slag composition is chosen where the alumina content is at a minimum. The $MgO:B_2O_3:Al_2O_3$ molar ratio is 4:5:1. The optical basicity of this composition is 0.530. Therefore, this is a nonbasic slag. According to FactSage, the viscosity of such a melt at 1300 °C is already quite low at just above 4.5 poise, and $T_m$ is only 1256 °C.

Similar to the soda-lime system, other oxides such as $Na_2O$, $K_2O$, CaO, $TiO_2$, and $SiO_2$ are introduced to the system to bring the viscosity and $T_m$ down to meet the requirements. In FactSage calculation, $T_m$ can be brought down by substituting MgO with CaO mole for mole until the paragenesis of $Mg_2B_2O_5$ is no longer possible, and the composition falls within the primary field of $MgB_4O_7$. The substitution of MgO with CaO increases the optical basicity of the slag. However, the slag remain nonbasic, so the GFA and crystallization tendency are unlikely to be affected negatively.

Since $B_2O_3$ is a rather pricy raw material, it is desirable to substitute it with other cheaper network former. Alumina is not a viable candidate as this would move the composition away from the viscosity minimum. Silica is a great candidate as this would make the composition shift from alkaline rich boroaluminate glass to borosilicate glass as shown in Figure 10. The main chemical composition of the system is composed of (C+M):(B+S):A with a molar ratio of 4:5:1. This gives a basic to nonbasic oxide molar ratio of 2:3. Therefore in this case the alumina acts as a network modifier.

For lowering viscosity $Na_2O$ and $K_2O$ are considered. Calculating with FactSage, the alkali mixing effect is found to be not so pronounced like in the soda lime slag system. Therefore for the simplicity of the chemical system $K_2O$ is not included in this chemical system, and only $Na_2O$ is used to decrease viscosity. The basic to nonbasic oxide molar ratio of 2:3 is kept unchanged by the addition of $TiO_2$, which also lowers optical basicity. Due to this system being nonbasic, the nepheline discriminator is always observed.

### 3.4. Testing methods

The compositions showing the least degree of crystallization during quenching are selected for comprehensive testing on its viscosity and melting point, with rheometer, DTA, and FCT. If the viscosity and melting point of the slag meet the requirements, SHTT is conducted to construct the TTT diagram. Microscopy and XRD are conducted to identify the phase formation from FCT. The experimental flowsheet is shown in Figure 16.

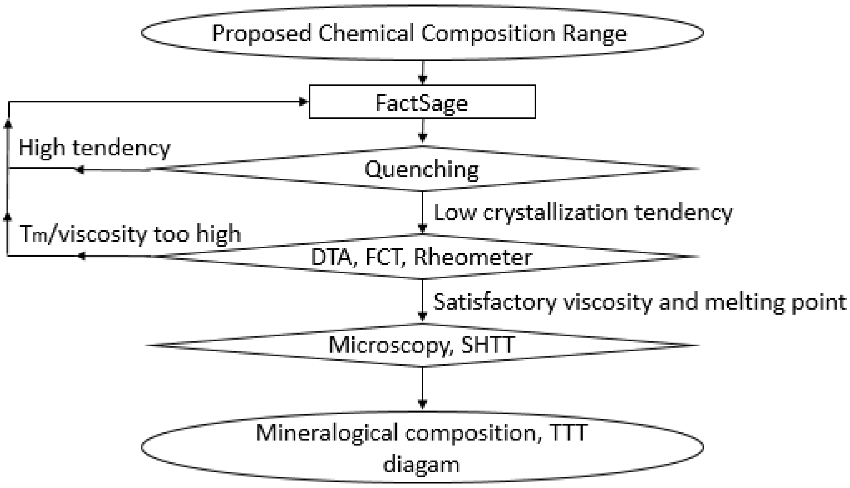

Figure 16. Experimental flowsheet

### 3.4.1. Sample preparation

The raw materials used are of high purity. The alkalis are in the form of carbonates. The slag compositions from FactSage are converted from moles to weight fractions. The weight of each raw material for the sample is calculated based on its purity and LOI due to $CO_2$. The powders are grinded and homogenized in a mill. For quenching test it is heated to 1400 °C in platinum crucibles for 15 minutes, then quenched on an iron plate of room temperature. The GFA of the quenched slag is visually evaluated by observing how much of its volume has crystallized. Slags with high GFA are milled to fine powder for subsequent testing.

### 3.4.2. Rheometer

A rotary rheometer is used to measure the viscosity of the slag and identify its breaking temperature. The Anton Paar FRS 1800 rheometer used is of the concentric cylinder type. For each trial, 34 g of post-quenching slag sample is loaded into a corundum crucible. The sample is heated to 1400 °C with the maximum heating rate. At 1400 °C the temperature is maintained for 15 min to homogenize the melt. Then the rotor is immersed into the melt, and the rotation speed is set to 7.21 rpm. Once the rheometer gets a consistent torque measurement from the melt, the sample is cooled with 5 K/min, and measurement values are recorded until the torque reaches 0.1 Nm. The viscosity of the sample is evaluated using the following relation:

$$\mu = \frac{M}{n} * K \tag{30}$$

where M is torque in N•m, n is the rpm, and K is a correction factor. For analysis the decadic logarithm of viscosity is plotted against the reciprocal of the decadic log of temperature, and $T_{br}$ can be determined using the method prescribed in Figure 3. Viscosity at 1300 °C is discerned from the obtained tabulated values.

### 3.4.3. Simultaneous thermal analysis

Simultaneous thermal analysis is used to determine the exothermal or endothermal effects taking place in a sample during heating and cooling in dependence of temperature, e.g. the liquidus or the crystal formation. The DTA apparatus used is Netzsch STA 449 F3. For each measurement, 100 mg of quenched slag is loaded for the test; an empty crucible is inserted as reference. Heating is conducted at 20 K/min until the temperature reaches 1400 °C. Then the furnace is cooled at 10 K/min to room temperature. The weight change of the slag is recorded during the experiment in order to investigate possible evaporation and therefore a modification to the chemical composition of the slag.

### 3.4.4. Furnace crystallization test

Furnace crystallization test is used to reduce the specific surface of the slag compared to the DTA. A further advantage is the possibility to investigate the sample after cooling to room temperature microscopically. Twenty-seven grams of quenched slag sample is weighted into a platinum crucible. A thermocouple is inserted into the slag sample to measure its temperature. Heating is conducted at 5 K/min until the temperature reaches 1350 $^{o}$C. After a dwell time of 15 min at maximum temperature, the furnace is cooled at 10 K/min to room temperature. The inert reference material used for the FCT is corundum. The principle behind the measurement is rather similar to DTA. The control of the temperature by the furnace is not as accurate as DTA by comparison. However, FCT results are reliable as there is less severe material loss in the case where the slag has high alkali or $B_2O_3$ contents.

The obtained solidified sample is cut in half. The half with the platinum wire is made into a polished section, since the crystallization around the wire is of interest. It is used for reflected light microscopy and SEM. The other half of the sample is milled for XRD measurement.

### 3.4.5 Mineralogical Investigations

The crystalline phases of the slag are analyzed using XRD after grinding the slag to analytical fineness. Based on the X-ray pattern, the mineralogical phases are identified. However, XRD could not measure accurately trace mineral phases. The presence of glass phase is indicated by an increase in the background.

From the polished section, at least two representative areas are selected and images of different magnifications were recorded with the reflected light microscope. These were then investigated with the scanning electron microscope, including energy dispersive X-ray spectroscopy. Together with the XRD results the mineralogical composition of each sample can be obtained. The representative SEM images give an assessment of the major and minor phases.

### 3.4.6. Single hot thermocouple technique

For slags with satisfactory results from rheometer, FCT, and DTA, TTT diagrams are constructed using SHTT. The slag is quenched, milled, and pressed into a thin section for sample preparation. A U-shaped platinum wire is inserted into the furnace chamber of the SHTT and heated to 1300 $^{o}$C. A suitable samples mass is positioned onto the wire. After total liquefaction it is stretched with a special stretching device within the U-shaped wire and then quenched to 700, 800, 900, and 1000 $^{o}$C respectively. It is assumed that the nose temperature is located between 800 and 900 $^{o}$C. Therefore, compositions showing a very rapid crystallization rate at 700 and 1000 $^{o}$C are discarded from further testing. A camera is used to take photos during the testing. These are analyzed in order to obtain the crystalline fraction of the slag area in dependence on the experimental time. For each investigated temperature, based on the crystalline area, the time for 0.5, 50, and 95% crystallinity, respectively, is obtained. Mean values out of at least 3 measurements are calculated to construct the TTT diagram.

# 4. Results and Discussion

## 4.1. Soda-lime-silicate slag system

### 4.1.1. Quenching results and selection of compositions

The composition at point 24 in Figure 15 exhibits high GFA from its quenching test (Figure 18a). The quenched slag is glassy exhibiting no devitrification; it has a very faint pink color due to its $TiO_2$ contents. This composition, serialized as E-2018- A002, seems promising. Nevertheless, the effects of $Al_2O_3$ on the system is studied by introducing it into composition A002 at A/S molar ratios of 3/40, 6/40, and 7.5/40, while maintaining the same $T_m$ and viscosity according to FactSage, in a series of compositions as listed in Table 9. The molar compositions are listed in Table B1 of Appendix B. The introduction of $Al_2O_3$ results in the increase in optical basicity, and therefore an increase in devitrification tendency. The quenching results of these compositions are shown in Figure 18.

Table 9. Compositions of soda-lime-silicate system with introduction of $Al_2O_3$

| slag serial | [wt%] | $SiO_2$ | CaO | $Na_2O$ | $K_2O$ | MgO | $TiO_2$ | $Al_2O_3$ | $\Lambda_{th}$ |
|---|---|---|---|---|---|---|---|---|---|
| E-2018-A002 | | 39.22 | 31.39 | 11.53 | 5.84 | 3.03 | 8.99 | 0 | 0.707 |
| E-2018-A003 | | 33.69 | 26.73 | 14.34 | 7.13 | 3.48 | 10.34 | 4.26 | 0.725 |
| E-2018-A004 | | 29.09 | 23.07 | 15.53 | 7.86 | 4.29 | 12.76 | 7.86 | 0.736 |
| E-2018-A005 | | 27.39 | 21.73 | 16.24 | 8.05 | 4.68 | 13.20 | 8.71 | 0.741 |
| E-2018-A008 | | 32.97 | 28.30 | 12.95 | 6.56 | 3.78 | 11.24 | 4.20 | 0.724 |
| E-2018-A009 | | 32.72 | 30.08 | 12.35 | 6.26 | 3.63 | 10.80 | 4.16 | 0.726 |
| E-2018-A010 | | 33.27 | 25.23 | 14.02 | 7.09 | 4.07 | 12.09 | 4.23 | 0.721 |
| E-2018-A015 | | 29.21 | 20.92 | 16.27 | 8.24 | 4.52 | 13.42 | 7.43 | 0.734 |
| E-2018-A016 | | 28.08 | 19.72 | 16.86 | 8.54 | 4.76 | 13.71 | 8.84 | 0.741 |

As can be seen in Figure 17, slag A005, A008, and A009 all exhibit low GFA. This is due to their C/S ratio being too high. C/S ratio needs to be decreased corresponding to $Al_2O_3$ contents if high GFA is to be maintained:

$$CaO_{(mol)} = \frac{6}{7} SiO_{2(mol)} - \frac{3}{5} Al_2O_{3(mol)} \tag{31}$$

Slag A010 (Figure 18g) and A015 (Figure 18h) both exhibit high enough GFA to warrant further investigation along with A002. They have A/S molar ratio of 0.075 and 0.015, respectively.

Figure 17. Quenched slags of a) A002, b) A003, c) A004, d) A005, e) A008, f) A009, g) A010, h) A015, and i) A016.

MnO and FeO are introduced into the chemical system at 0.4 or 0.8 wt% with A/S molar ratios being zero, 0.075, and 0.15. The compositions have the same $T_m$ and viscosity as A002 according to FactSage, and are listed in table 10. The molar compositions are listed in Table B2 of Appendix B. MnO and FeO contents does not have an effect on optical basicity, as slags A002, A019, and A020 share the same A/S molar ratio of 0 and $\Lambda_{th}$ of 0.707; as well as slags A010, A017, and A018 with A/S molar ratio of 0.075 and $\Lambda_{th}$ of 0.721; so do slags A015, A021, and A022 with A/S molar ratio of 0.15 and $\Lambda_{th}$ of 0.734. The quenched slags are shown in Figure 18. Their color is obsidian due to the MnO and FeO content. It could be observed from Figure 18c and 18d that MnO and FeO in the absence of $Al_2O_3$ significantly reduce GFA. Out of the compositions A018 clearly exhibits the highest GFA and is selected for further testing.

Table 10. Compositions of soda-lime-silicate system with introduction of FeO and MnO

| slag serial | [wt%] | $SiO_2$ | CaO | $Na_2O$ | $K_2O$ | MgO | $TiO_2$ | FeO | MnO | $Al_2O_3$ | $\Lambda_{th}$ |
|---|---|---|---|---|---|---|---|---|---|---|---|
| E-2018-A017 | | 33.19 | 25.17 | 13.69 | 6.93 | 4.03 | 11.98 | 0.40 | 0.39 | 4.22 | 0.721 |
| E-2018-A018 | | 33.12 | 25.11 | 13.37 | 6.77 | 3.99 | 11.85 | 0.79 | 0.78 | 4.21 | 0.721 |
| E-2018-A019 | | 38.61 | 30.90 | 10.66 | 5.40 | 3.43 | 10.20 | 0.40 | 0.40 | 0 | 0.707 |
| E-2018-A020 | | 38.46 | 30.78 | 10.35 | 5.23 | 3.42 | 10.16 | 0.80 | 0.79 | 0 | 0.707 |
| E-2018-A021 | | 29.15 | 20.88 | 15.94 | 8.08 | 4.47 | 13.28 | 0.39 | 0.39 | 7.42 | 0.734 |
| E-2018-A022 | | 29.11 | 20.85 | 15.63 | 7.92 | 4.41 | 13.12 | 0.78 | 0.77 | 7.41 | 0.734 |

Figure 18. Quenched slags of a) A017, b) A018, c) A019, d) A020, e) A021, and f) A022.

$B_2O_3$ is introduced into the soda-lime-silicate system at B/S molar ratio of 0.075 and 0.15 with A/S molar ratio being 0 and 0.075. The compositions have the same $T_m$ and viscosity as A002 according to FactSage, and are listed in table 11. The molar compositions are listed in Table B3 of Appendix B. $B_2O_3$ has the effect of significantly reducing optical basicity, and therefore the compositions have high GFA. However, slags A035 (Figure 19c) and A036 (Figure 19d) exhibit low GFA due to C/S ratio being too high. This shows that $B_2O_3$ has the same effect on C/S ratio as $Al_2O_3$ if high GFA is to be maintained:

$$CaO_{(mol)} = \frac{6}{7}SiO_{2(mol)} - \frac{3}{5}(Al_2O_{3(mol)} + B_2O_{3(mol)}) \tag{32}$$

The quenched slags of A033, A039, and A040 exhibit high GFA showing no devitrification tendency. Compositions A033 and A040 are selected for further testing.

Table 11. Boron-containing compositions of soda-lime-silicate system

| slag serial | [wt%] | $SiO_2$ | CaO | $Na_2O$ | $K_2O$ | MgO | $TiO_2$ | $Al_2O_3$ | $B_2O_3$ | $\Lambda_{th}$ |
|---|---|---|---|---|---|---|---|---|---|---|
| E-2018-A033 | | 32.61 | 23.35 | 14.48 | 7.33 | 3.84 | 11.41 | 4.15 | 2.83 | 0.707 |
| E-2018-A034 | | 32.48 | 24.63 | 14.04 | 7.10 | 3.73 | 11.07 | 4.13 | 2.82 | 0.708 |
| E-2018-A035 | | 32.28 | 26.43 | 13.40 | 6.78 | 3.57 | 10.62 | 4.11 | 2.80 | 0.710 |
| E-2018-A036 | | 32.10 | 27.81 | 12.93 | 6.55 | 3.45 | 10.25 | 4.09 | 2.79 | 0.711 |
| E-2018-A039 | | 37.95 | 28.78 | 11.77 | 5.96 | 3.08 | 9.16 | 0 | 3.30 | 0.690 |
| E-2018-A040 | | 37.23 | 26.66 | 12.27 | 6.21 | 2.81 | 8.35 | 0 | 6.47 | 0.675 |

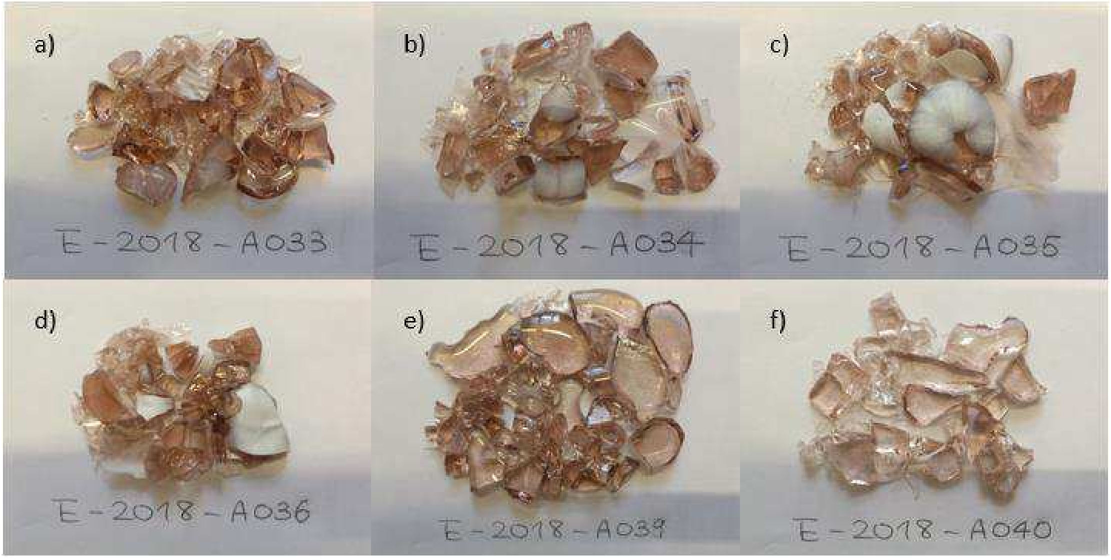

Figure 19. Quenched slags of a) A033, b) A034, c) A035, d) A036, e) A039, and f) A040.

In summary, the chemical compositions showing good GFA and moving onto further testing are shown in Table 12.

Table 12. Soda-lime-silicate slags selected for further testing

| slag serial | [wt%] | $SiO_2$ | CaO | $Na_2O$ | $K_2O$ | MgO | $TiO_2$ | FeO | MnO | $Al_2O_3$ | $B_2O_3$ | $\Lambda_{th}$ |
|---|---|---|---|---|---|---|---|---|---|---|---|---|
| E-2018-A002 | | 39.22 | 31.39 | 11.53 | 5.84 | 3.03 | 8.99 | 0 | 0 | 0 | 0 | 0.707 |
| E-2018-A010 | | 33.27 | 25.23 | 14.02 | 7.09 | 4.07 | 12.09 | 0 | 0 | 4.23 | 0 | 0.721 |
| E-2018-A015 | | 29.21 | 20.92 | 16.27 | 8.24 | 4.52 | 13.42 | 0 | 0 | 7.43 | 0 | 0.734 |
| E-2018-A018 | | 33.12 | 25.11 | 13.37 | 6.77 | 3.99 | 11.85 | 0.79 | 0.78 | 4.21 | 0 | 0.721 |
| E-2018-A033 | | 32.61 | 23.35 | 14.48 | 7.33 | 3.84 | 11.41 | 0 | 0 | 4.15 | 2.83 | 0.707 |
| E-2018-A040 | | 37.23 | 26.66 | 12.27 | 6.21 | 2.81 | 8.35 | 0 | 0 | 0 | 6.47 | 0.675 |

### 4.1.2. Viscosity and breaking temperature

The viscosities at 1300 °C and dynamic $T_{br}$ at cooling rate of 5 K/min of the slags listed in Table 12 are shown and summarized in Figure 20, which are compared to two $CaF_2$-containing common industrial slags. It could be seen that the $T_{br}$'s of the tested compositions are reasonably close to those of the industrial slags. However, a sharp increase in viscosity at temperatures below $T_{br}$ often indicates high crystallization tendency. From this perspective only composition A040 exhibits a similar viscosity profile as the industrial slags. Overall it could be observed that $Al_2O_3$-containg slags have relatively high $T_{br}$ associated with high $\Lambda_{th}$, while boron-containing ones have relatively low $T_{br}$ associated with low $\Lambda_{th}$.

In terms of viscosity, FactSage has under-predicted the viscosity of the promising composition A002 by 33%. While according to FactSage all the tested compositions should have a viscosity of 3 poise at 1300 °C, the viscosities of A010 and A015 have decreased by about 1.3 poise compared to A002, due to them having A/S weight ratio of 0.125 and 0.25 respectively. In literature it was suggested that a viscosity minima could be expected around A/S weight ratio of 0.1 (Figure 12) [135]. So the composition of A010 is relatively close to that minima. The viscosity of A015 is kept similar to that of slag A010 due to the addition of alkalis and $TiO_2$ despite doubling the A/S ratio. This shows that the composition prediction method for the CAS system shown with the help of Figure 15 is a valid one.

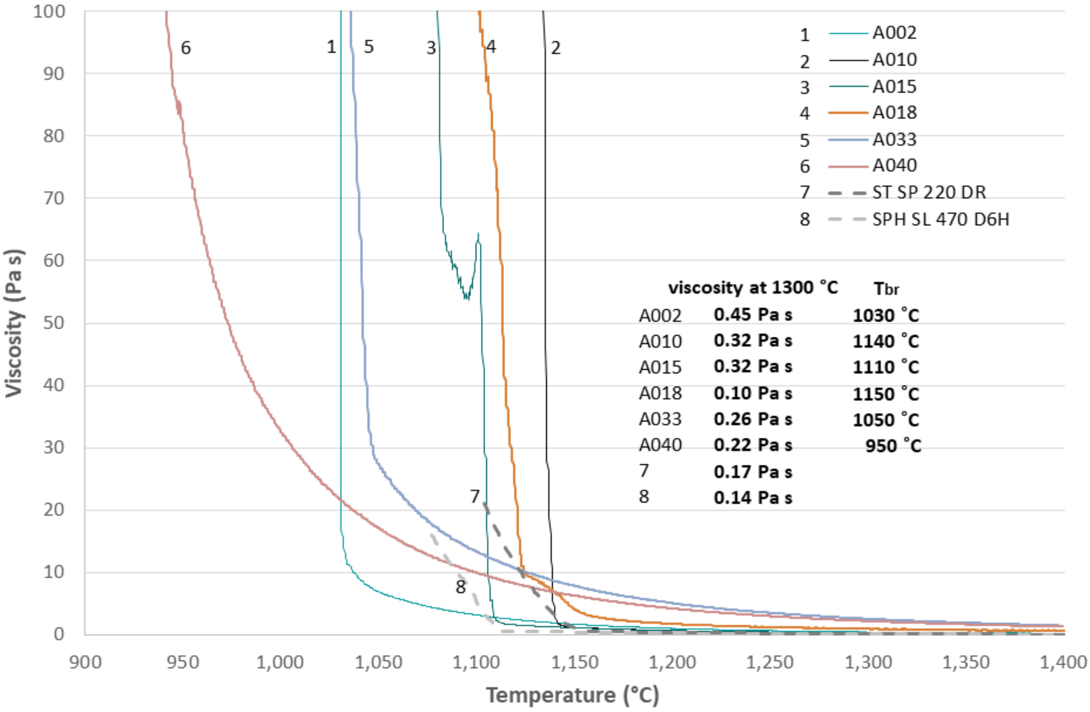

Figure 20. Viscosity of E-2018-A002 in dependence of temperature

The viscosity of slag A018 at 1300 °C is 1.0 poise, which is the only tested slag that has lower viscosity than the industrial slags. FactSage has over-predicted the viscosity by 200 %. The entropic consideration as prescribed in equation 6 could explain the low viscosity measured. Slag A018 has almost the exact composition as slag A010 except for the addition of 0.8 wt% of MnO and FeO. Therefore, the decrease in viscosity has not been expected to be this drastic. According to literature, for silicate melts the drop in viscosity was expected to be around 0.4-0.6 poise for adding two oxides at low percentages [33]. It would be interesting to further investigate whether small percentage contents of other intermediate basic oxides would have similar effects on viscosity.

The boron-containing slags A033 and A040 have viscosities of 2.57 and 2.21 poise respectively, which satisfy the requirements. According to literature the most cost-effect $B_2O_3$ content range for reduction in viscosity is between 1 and 4.4 wt% [36], of which the A040 exceeds. It is likely that FactSage under-predicts the viscosity of slags in this chemical system as boron content increases.

The viscosity results showed that FactSage has been inaccurate in its prediction for this NCAS system, making using its calculation as experimental control not very reasonable. This is perhaps due to the viscosity models utilized being not entirely suitable for this chemical system.

### 4.1.3. DTA and FCT

The chemical compositions of the FCT specimens were measured with SEM through analysis by area scans. Then the mean value was calculated and the results compared to the original compositions. There were hardly any discrepancies (Table D1, Appendix D). Therefore the slags are chemically stable. Nevertheless, this method is not suitable for accurately measuring the boron contents of the sample.

The DTA result for slag A002 is shown in Figure 21 and 22. The DTA results for the the other slags are presented in Appendix C.

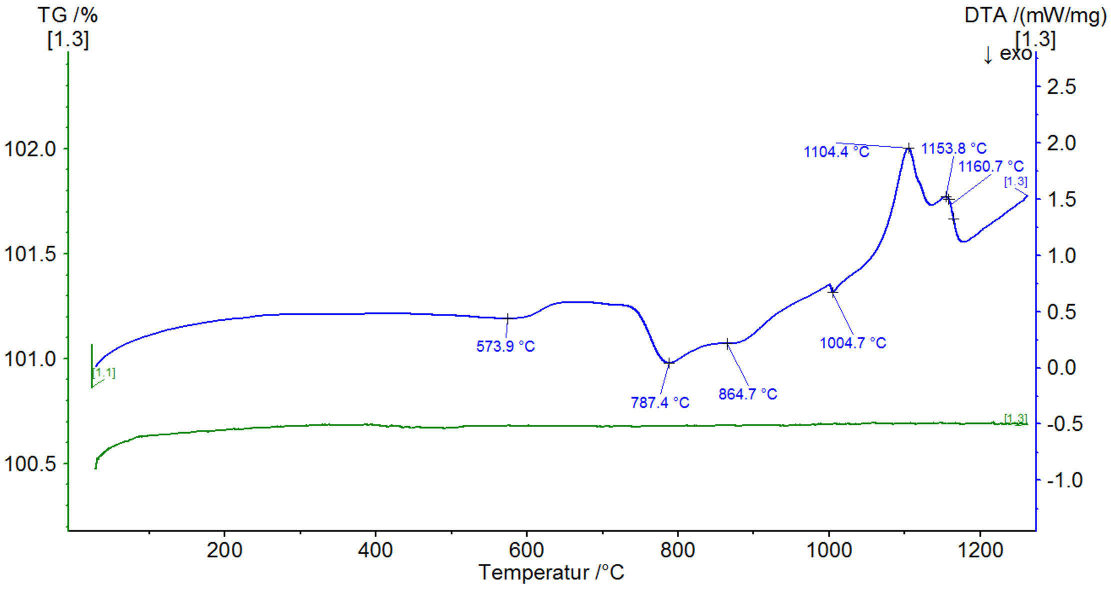

Figure 21. DTA heating curve for slag E-2018-A002

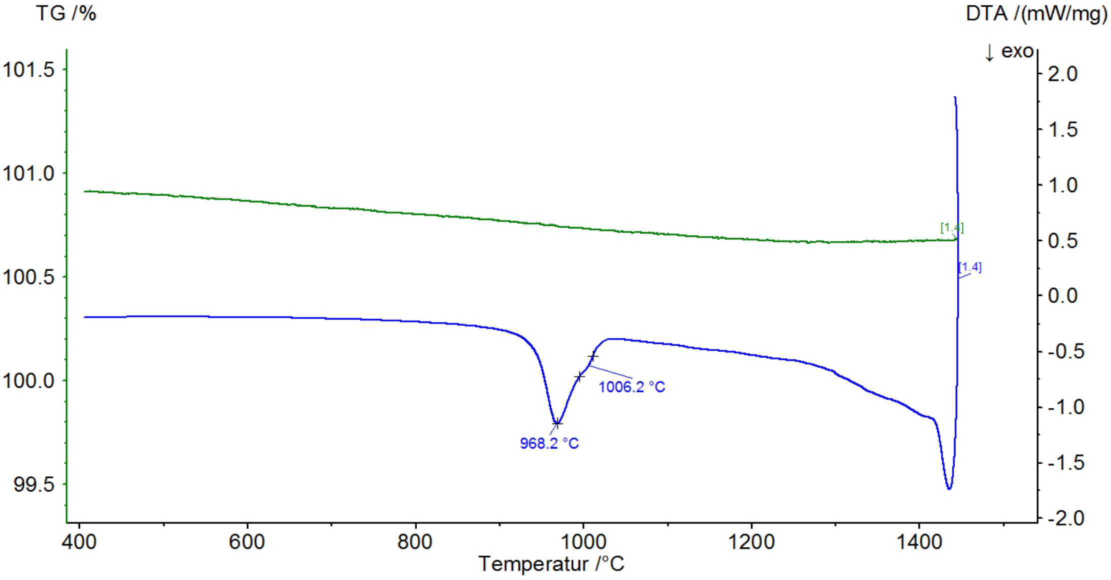

Figure 22. DTA cooling curve for slag E-2018-A002

In Figure 21, the heating curve shows that as the glassy slag is heated up, a series of four detectable phase changes take place, which indicate the devitrification of the slag. The nucleation maxima are at lower temperature than the crystallization maxima, which facilitates the devitrification process. It shows that at 1161 °C the sample is totally liquefied. This corresponds very well with the FactSage calculation of 1160 °C for the melting point. In Figure 22, the cooling curve shows that the onset of crystallization is 1006 °C, and the local minimum indicating the precipitation of the main phases is at 968 °C. There is no material loss indicated, so the sample is chemically stable. The FCT result for A002 is shown in Figure 23. It corresponds reasonably well with the DTA result, showing that the main phase precipitates at 1019 °C.

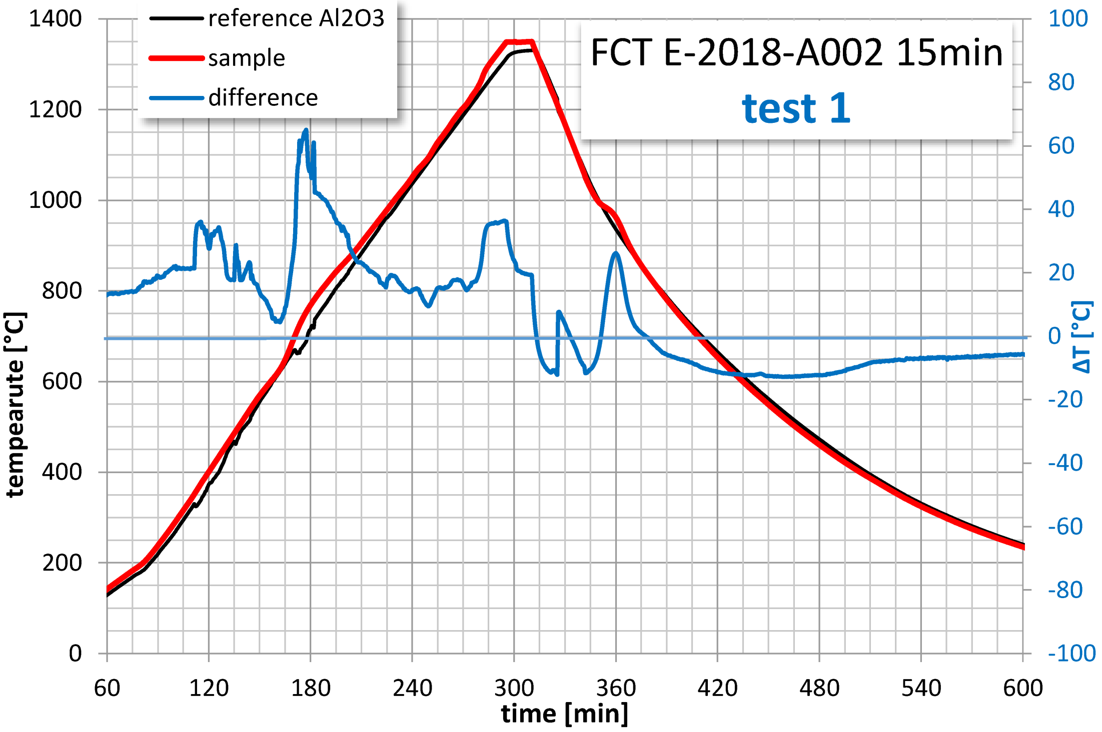

For slag A010, which has a molar A/S ratio of 0.075, solid phases are still present at 1339 °C, which does not meet the requirement of a liquidus temperature below 1260 °C. The cooling curve shows two local minima at 1116 and 875 °C respectively. This is corresponded by the FCT result (Figure D1, Appendix D), which shows the main phases precipitating at 1104 and 882 °C respectively. This suggests that the introduction of alumina has made the mineralogical composition of A010 more complex than A002.

For slag A015, which as an A/S molar ratio of 0.15, the last solid phase is detected at 1327 °C, which is similar to that of A010. There are three local minima indicating the precipitation of phases in the cooling curve. The first two minima are at 1069 and 884 °C respectively, which are similar to those found in A010. A third minimum is at 801 °C. This suggests that A010 and A015 share some main phases, but the rise in A/S molar ratios has made the mineralogical composition of A015 more complex with additional minor phases. The FCT result is shown in Figure D2 of Appendix D. It shows only one local minimum at 1075 °C, which suggests that the first minimum in the DTA cooling curve indicates the precipitation of main phases. This is not unreasonable because the exothermal heat zones are considerably smaller compared to the one at higher temperature, and therefore might not be detectable to FCT.

For slag A018, which has the nearly same chemical composition of A010 except for the addition of 0.8 wt% of MnO and FeO, the last crystalline phase is detected at 1341 °C, and the cooling curve has two local minima at 1089 and 888 °C respectively. The cooling curves of A010 and A018 are remarkably similar. This suggests that small percentages of MnO and FeO content do not have a significant impact on the main phases precipitated, which is expected. Nonetheless, they may have an effect on crystallization, suggested by the intensities of the peaks, especially at lower temperature. The FCT curve is shown in Figure D3 of Appendix D. It shows two local minima at 1061 and 845 °C respectively.

According to the DTA result of slag A033, which has both A/S and B/S molar ratios at 0.075, the last crystalline phase is detect at 1278 °C. Three local minima are present in the cooling curve. Two of these are at 1057 and 880 °C respectively, which are somewhat similar to those found in A010 and A015. A third minimum is found at 910 °C. This suggests that A010, A015, and A033 share some or all of the main phases, but the minor phases may be different. The FCT result is shown in Figure D4 of Appendix D, which shows two local minima at 910 and 810 °C respectively. There is discrepancy between the DTA and FCT, perhaps due to a 6 wt% loss in DTA while the FCT sample likely being chemically stable.

According to the DTA result of $Al_2O_3$-free slag A040, which has a B/S molar ratio of 0.15, the last of the crystal phase is present up to 1188 °C, which is satisfactory for the problem definition. The heating curve shows three small peaks at 155, 184, and 235 °C. These are likely volatile losses, which account for about 4 wt% of the sample. Therefore the true last solid temperature of the slag might be lower. There is a single local minima in the cooling curve at 953 °C, and the entire cooling curve is remarkably similar to that of slag A002. A chemical analysis has been performed on its FCT specimen, showing a composition of 38.05 % $SiO_2$, 27.47 % CaO, 3.19 % MgO, 8.99 % $TiO_2$, 12.56 % $Na_2O$, 4.96 % $K_2O$, and 5.32 % $B_2O_3$. This is very close to the original composition, and has the same C/S ratio. This shows that the boron content is chemically stable in slag A040 at least for the FCT sample.

Overall it could be observed that in DTA during heating, $Al_2O_3$-containg slags form crystalline phases that are still detectable above 1300 °C. They also likely have relatively high $T_{crys,\ onset}$ associated with high $\Lambda_{th}$. Boron-containing slags have more favorable melting behavior, and likely have relatively low $T_{crys,\ onset}$ associated with low $\Lambda_{th}$.

### 4.1.4. XRD and SEM

The mineralogical compositions of the FCT specimens were investigated with XRD and SEM. The XRD result for A002 is shown in Figure 24. The FCT specimen contains glassy phase as indicated by the background concave. The major phases detected are perovskite ($CaTiO_3$), calcium titanium silicate ($Ca_2TiSiO_6$), bredigite ($Ca_7MgSi_4O_{16}$), and combeite ($Na_2Ca_2Si_3O_9$). Perovskite is one of the major phases expected according to literature study. The paragenesis of $Ca_2TiSiO_6$ is likely due to insufficient amount of Ti. It is unknown if perovskite and $Ca_2TiSiO_6$

share the same Bravais lattice. The presence of perovskite is expected as there is no alumina content to shrink its primary field. A polymorph of belite, bredigite, is detected, which is desirable as belite has a high $T_m$. Combeite belongs to the pyroxenoid group. This is of the same silicate group as CS, meaning perhaps that in this complex chemical system, its paragenesis has taken the stead of the high $T_m$ phase CS, which is desirable. The XRD peaks of CS, $C_3S_2$, and $C_2S$ absolutely could not fit with A002.

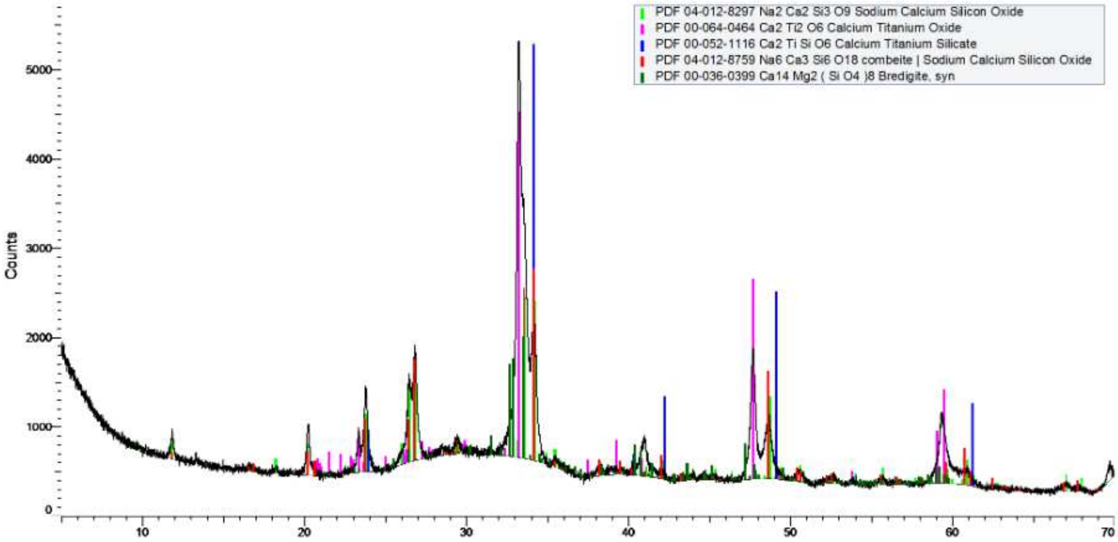

Figure 24. XRD result from FCT specimen of E-2018-A002

A representative SEM image of the FCT specimen is shown in Figure 25. Five phases could be visually distinguished from colors and grain boundaries. All five distinguishable phases have significant presence in the representative image, and could be considered the main phases. According to the chemical composition, the phase marked 1 is a glassy phase; the visual appearances are that of smooth and relatively continuous bodies. A solid solution of $Ca_2(Si,Ti)SiO_6$ is marked with 2. A dark colored phase is $NC_2S_3$, marked with 3. The lightest colored phase is marked with 4, which is bredigite in chemistry. A dark colored phase, which is marked by 5, can be observed at the center of many bredigite crystal grains, but also next to phase 3. The chemistry of this phase is indicative of $Ca_2SiTiO_6$, making it similar to phase 2. Due to being found at the center of bredigite crystals, the crystal growth of phases 4 and 5 should involve a diffusion mechanism between the two. The differences in local diffusion driving force may explain the difference in chemistry between phase 2 and 5. The residual glassy phase contains about 0.5 wt% $Al_2O_3$, which likely came from impurities, while the other phases are alumina-free. It would be interesting to investigate if doping the composition of A002 with small percentages of $Al_2O_3$ would actually increase the amount of glassy phase.

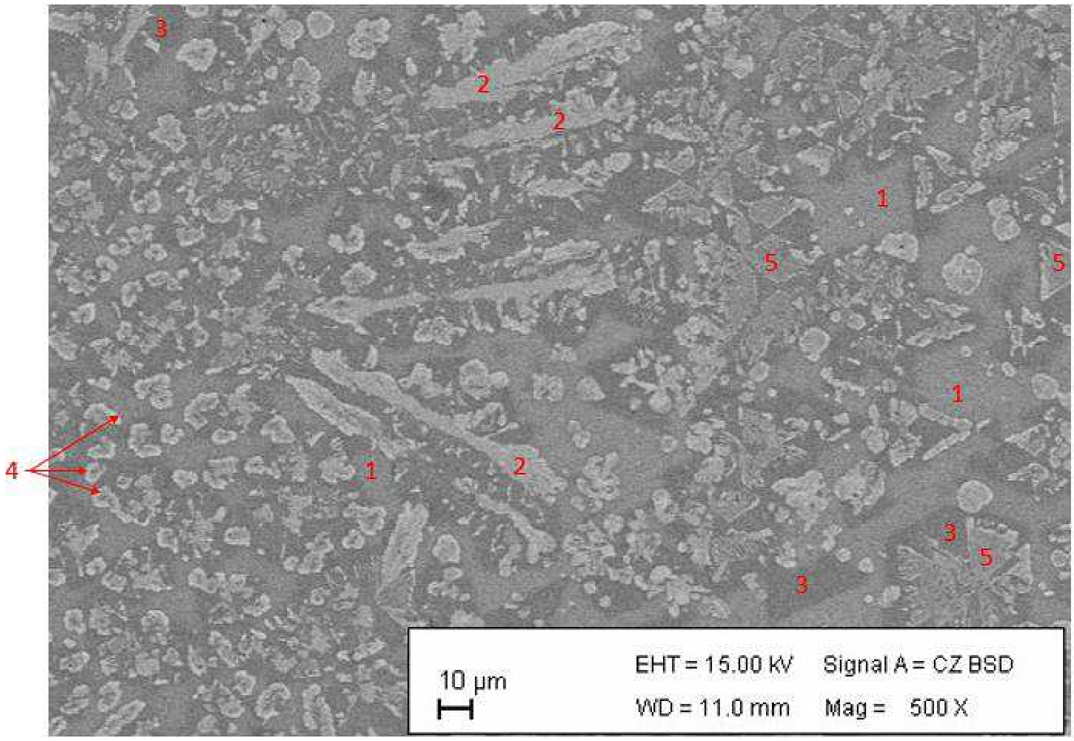

Figure 25. Representative SEM image of E-2018-A002, the phases as marked are:

1….. glassy phase
2….. $Ca_2(Si,Ti)SiO_6$
3….. $Na_2Ca_2Si_3O_9$
4….. bredigite
5….. $Ca_2TiSiO_6$

The XRD result for A010 is shown in Figure 26. The pattern is indicative of no residual glassy phase. The main phases detected are perovskite, $C_2S$, and combeite. The paragenesis of $C_2S$ is particularly undesirable, as it has a $T_m$ of 2130 °C. This explains the fact that last solid was observed at above 1300 °C during heating in DTA, and the high $T_{crys,onset}$ of composition A010. Minor phases detected include $Na_2TiO_3$ and kalsilite.

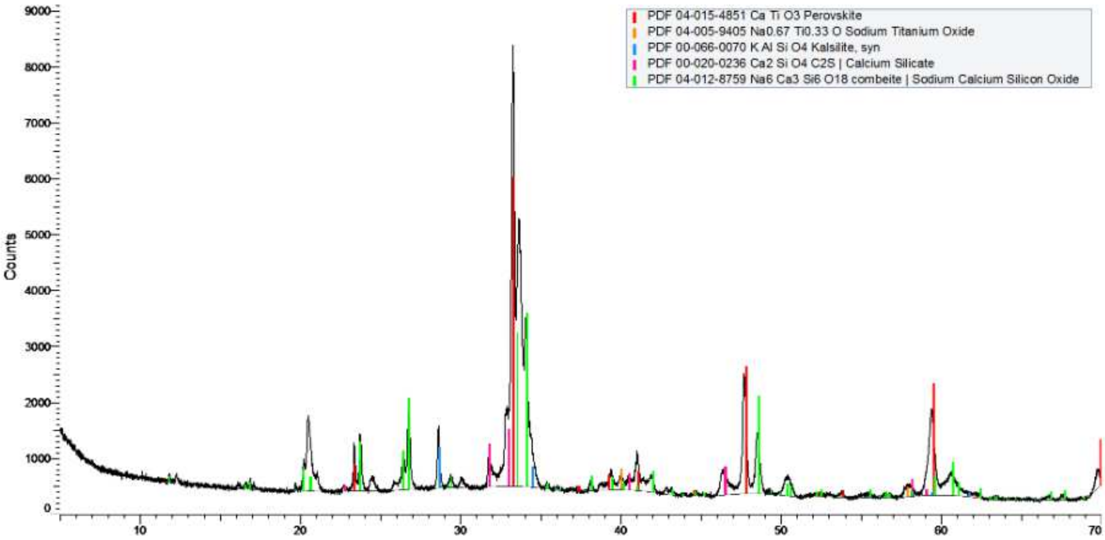

Figure 26. XRD result from FCT specimen of E-2018-A010

The representative SEM image of the FCT specimen for A010 is shown in Figure 27. Five phases could be discerned visually. Two phases exhibit clear dendritic crystal growth pattern in their paragenesis. Of these two the white colored phase, marked by 1, is perovskite having up to one-third of Ti substituted by Si. Therefore this is not a true perovskite phase, but probably a phase in between perovskite and sphene ($CaTiSiO_5$). However, the XRD peaks agree with perovskite more than with sphene. The light grey phase, which have needle-like crystals, are mostly sandwiched between the perovskite crystals. This phase, marked by 2, is $C_2S$, which is present in a relatively pure form. The mechanism of crystal growth likely involves the crystallization of the $C_2S$ phase first. $TiO_2$ diffuses out of $C_2S$, and perovskite crystallizes, which is followed by the diffusion of $Al_2O_3$ out of both $C_2S$ and perovskite. The grey phase, marked by 3, represents $Na_2TiO_3$ with a significant substitution of Na by K. An interstitial phase appears dark grey, marked by 4, is a modification of combeite with significant substitution of Na by K with the approximate formula of $Na_{1.5}K_{0.5}CaSi_2O_6$. This N/K ratio happens to be the designed N/K ratio for minimizing viscosity (section 3.3.1). Kalsilite, marked as 5, is present in small amount with crystal grain sizes below 10 micron. It could be observed that kalsilite crystals are mostly embedded within larger $Na_2TiO_3$ crystals, which suggests that kalsilite precipitates due to cooling out of $Na_2TiO_3$ due to the decreasing solubility.

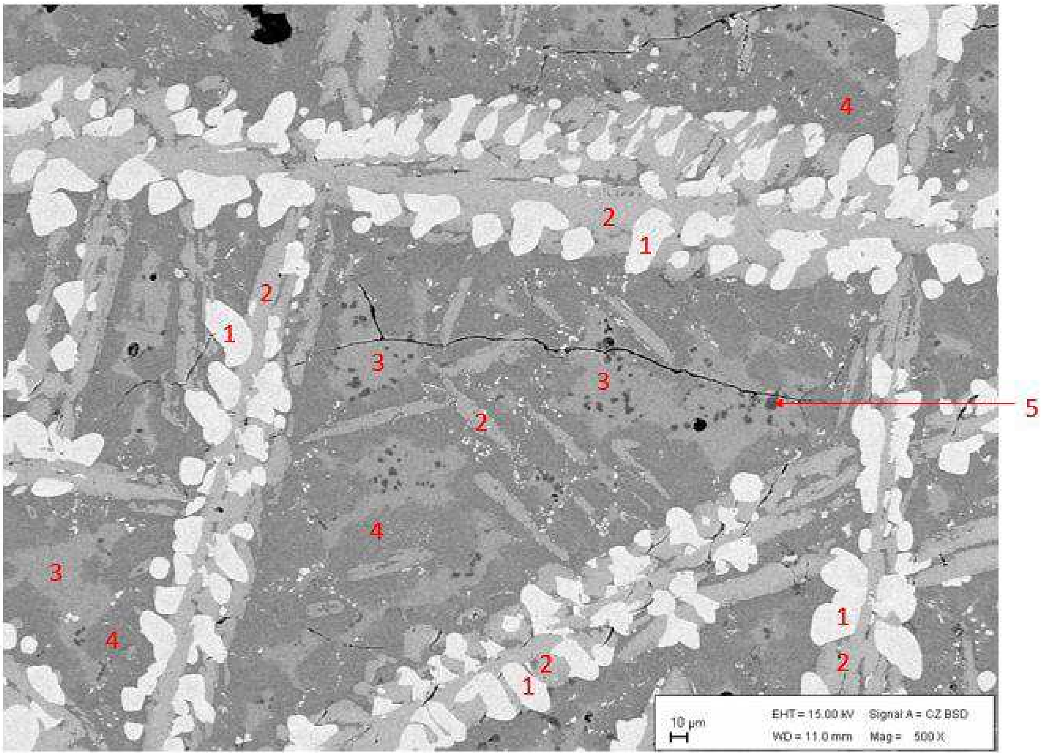

Figure 27. Representative SEM image of E-2018-A010, the phases as marked are:

1….. perovskite
2….. $Ca_2SiO_4$
3….. $Na_2TiO_3$
4….. combeite
5….. kalsilite

It was discussed in section 4.1.2 that according to DTA slag A010 and A015 would have different phases due to their A/S molar ratios being 0.075 and 0.15 respectively. This is confirmed by both the XRD result shown in Figure 28 and the representative SEM images shown in Figure 29. Combeite, a major phase in A010, could not be found in the FCT specimen of A015. However, the undesirable phase $C_2S$ is still a main phase. The XRD pattern is indicative of no glassy phase present.

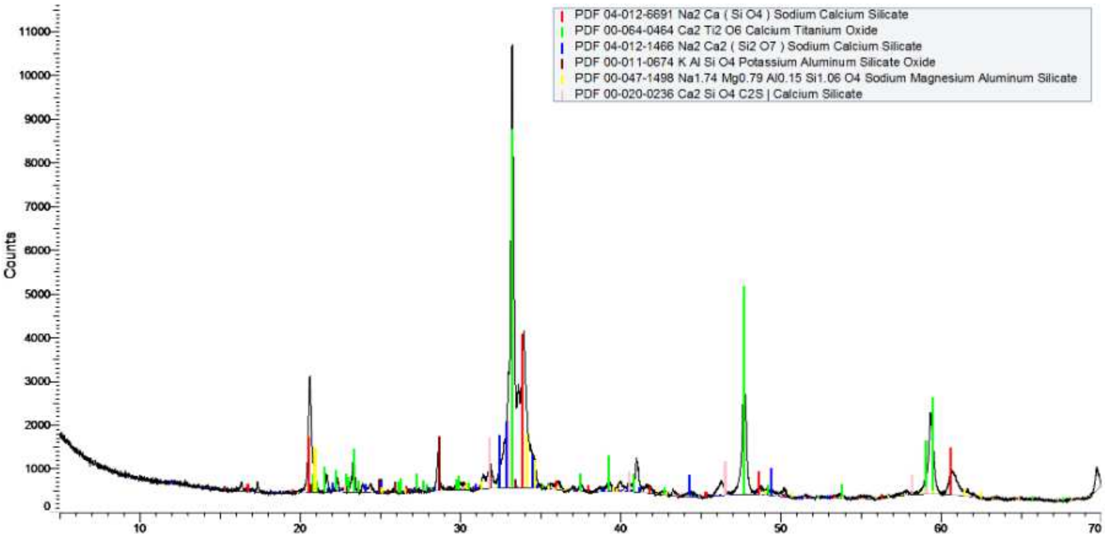

Figure 28. XRD result from FCT specimen of E-2018-A015

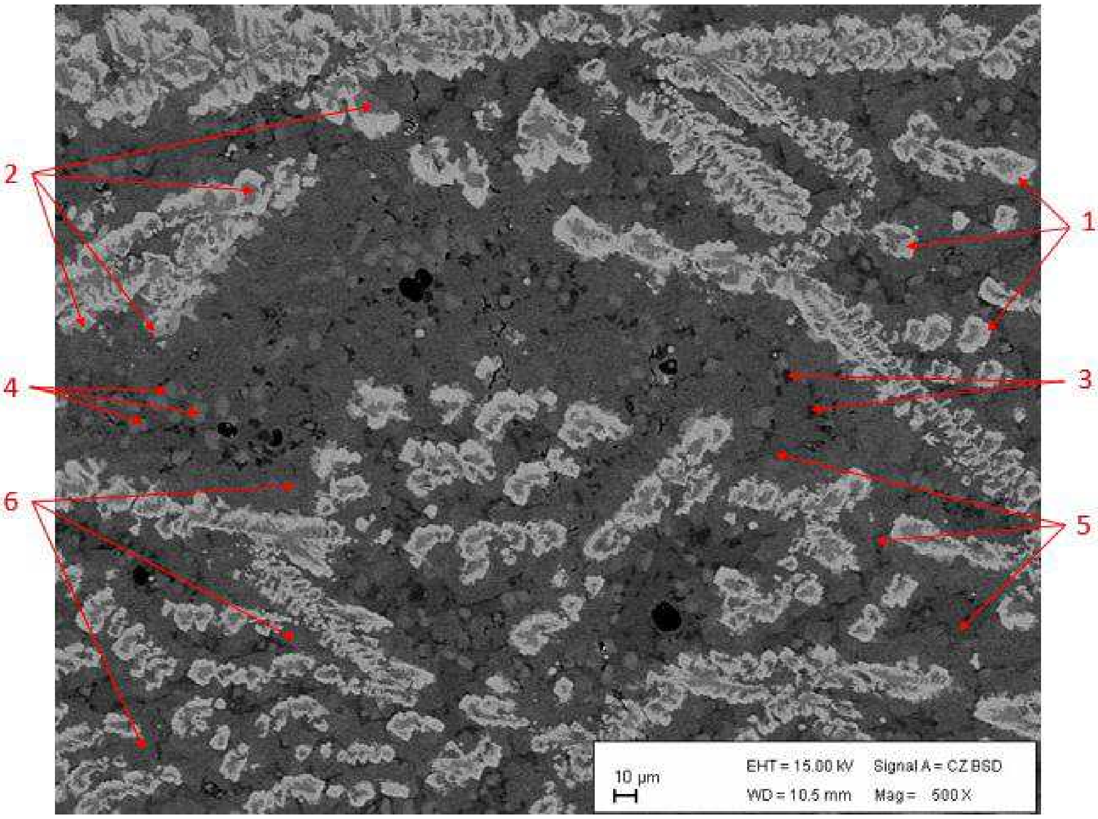

Figure 29. Representative SEM image of E-2018-A015, the phases as marked are:

| | |
|---|---|
| 1….. perovskite | 2….. $Ca_2SiO_4$ |
| 3….. kalsilite | 4….. sodium magnesium aluminum silicate |
| 5….. $Na_2CaSiO_4$ | 6….. $Na_2Ca_2Si_2O_7$ |

From Figure 29, similar dendritic growth of perovskite (marked as 1) and $C_2S$ (marked as 2) as seen in slag A010 was observed. However, the crystal sizes are considerably smaller compared to A010. This suggests that the crystallization process takes place at lower temperatures, as the material transport is reduced and results in smaller crystal sizes. This is confirmed by the DTA result. Four further phases could be distinguished, all of which have grain sizes below 10 microns. The phase with the darkest color, marked as 3, is kalsilite. A sodium magnesium aluminum silicate phase is marked as 4. Two phases with similar appearance in the SEM image fill the interstitial spaces. The slightly darker-colored phase, marked as 5, is $Na_2CaSiO_4$; the lighter colored crystal, marked as 6, is $Na_2Ca_2Si_2O_7$. Within the sample perovskite encircles the smaller dendritic crystals almost entirely.

It was discussed in section 4.1.2 that according to DTA slag A010 and A018 would have similar main phases due to their A/S molar ratios both being 0.075. This is confirmed by both the XRD result shown in Figure 30 and the representative SEM image shown in Figure 31. The XRD pattern is indicative of no glassy phase present.

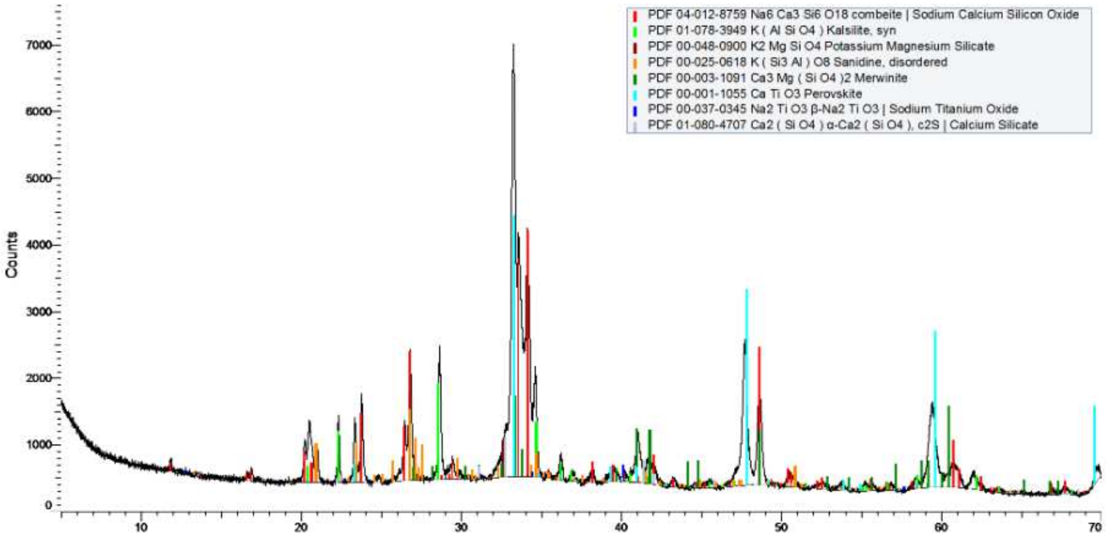

Figure 30. XRD result from FCT specimen of E-2018-A018

Also in this sample perovskite was formed in contact with the $C_2S$ crystals. $Na_2TiO_3$ and combeite are further phases, which are present in lesser amounts and smaller crystals. A minor phase, kalsilite, is marked as 5, which appears at the center of $Na_2TiO_3$ crystals. These phases were also found in the A010 FCT specimen.

Three phases not found in A010 are minor phases whose paragenesis is due to the MnO and FeO contents. One relatively more frequently formed phase, marked as 6, was an interstitial phase between large $Na_2TiO_3$ and combeite crystals. This phase is $K_2MgSiO_4$. A phase with needle-like crystals, marked as 7, is sanidine ($KSi_3AlO_8$), which is very undesirable as it greatly increases the devitrification tendency of the solidified melt [134, 135]. One minor phase with similar color to KMS is merwinite ($Ca_3MgSi_2O_8$), marked as 8. The phase bredigite found in A002, which has a chemical composition between merwinite and $C_2S$, could absolutely not be detected in this sample. It is unlikely that the paragenesis of these minor phases play a major role in the crystallization process, and A018 shares similar crystal growth mechanism with A010, as suggested by the DTA results.

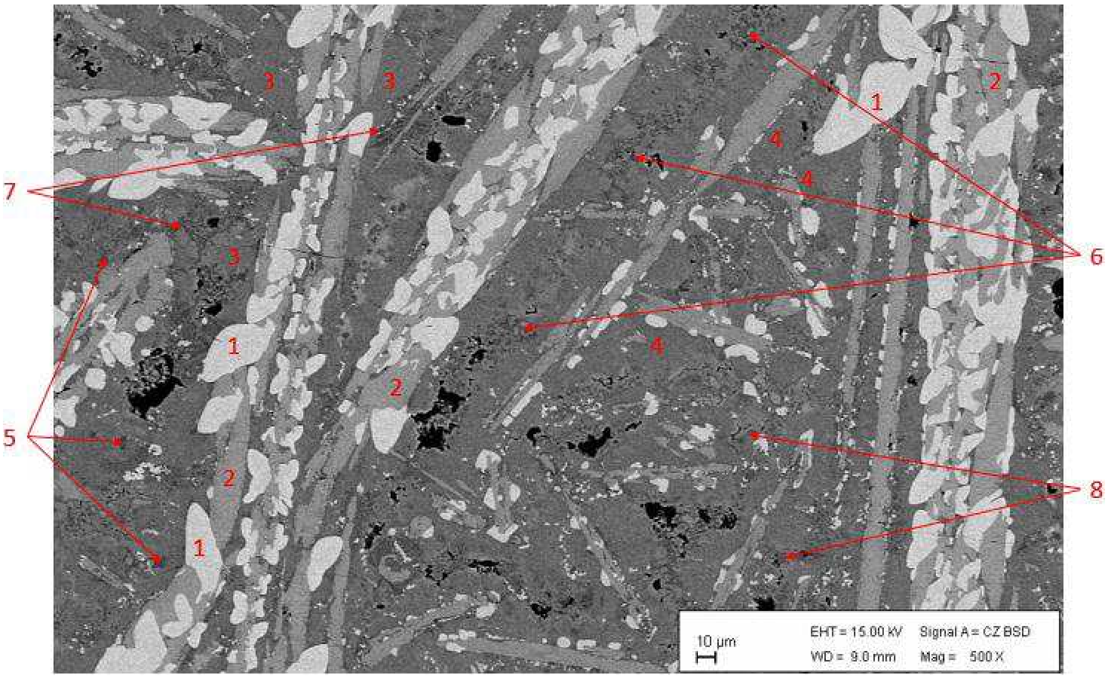

Figure 31. Representative SEM image of E-2018-A018, the phases as marked are:

1….. perovskite

2….. $Ca_2SiO_4$

3….. $Na_2TiO_3$

4….. combeite

5….. kalsilite

6….. $K_2MgSiO_4$

7….. sanidine

8….. merwinite

The XRD result of A033 is shown in Figure 32, which shows that the FCT specimen does not contain significant amount of residual glassy phase.

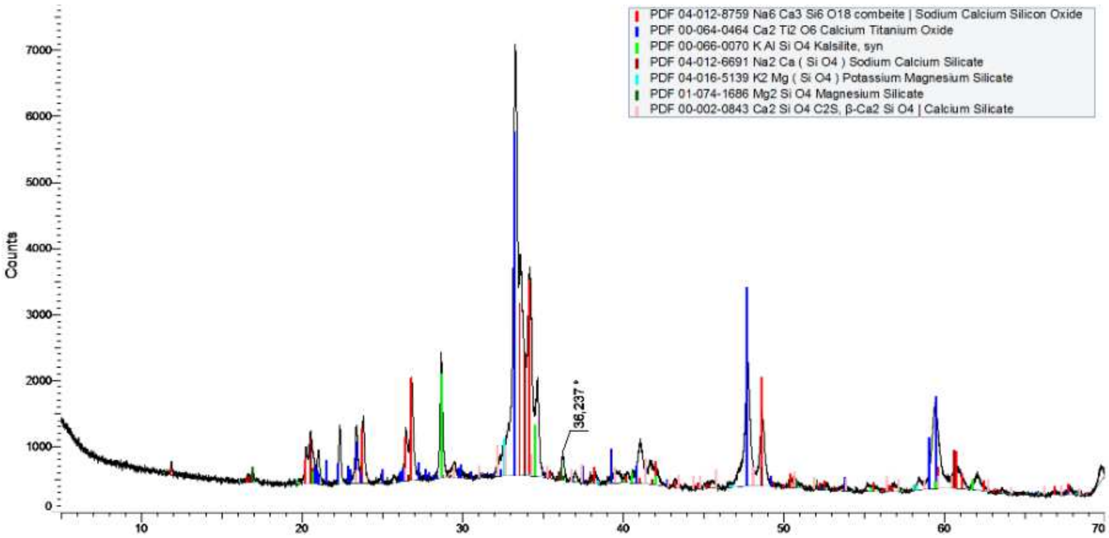

Figure 32. XRD result from FCT specimen of E-2018-A033

A representative SEM image of slag A033 is shown in Figure 33. The perovskite phase, marked as 1, encircles the other dendritic crystals almost entirely, similar to that of A015. It can be seen that the $C_2S$ crystals are at the center of the perovskite crystals. The crystal grains are relatively small at below 20 microns, suggesting that the crystallization takes place at a relatively low temperature, which agrees with the FCT result showing a relatively low $T_{crys,onset}$. The phase NCS, marked as 3, is also a major phase in A033. According to its chemical composition, this phase has significant substitution of Na by K, which is due to the composition being designed to have an N/K ratio of 3. The phase combeite, marked as 4, is one of the minor phases. The phase kasilite, marked by 5, has very limited presence, and the crystal grains are below 2 microns.

Two rare interstitial phases are present. One is $K_2MgSiO_4$, marked as 6. This phase seems to be formed at the end of the crystallization process, because it is located between combeite and NCS, and does not show well defined crystal grains. The other phase is forsterite, marked as 7, has approximately a square-shape. Its crystal grains are small at below 2 microns. No boric binary or ternary phases have been detected. This suggests that boron has been partly implemented into the crystal structures of the aforementioned phases, but was below the detection limit of the equipment. The DTA result was indicative of boron evaporation, but the FCT result was not, which is likely due to lower specific sample surface.

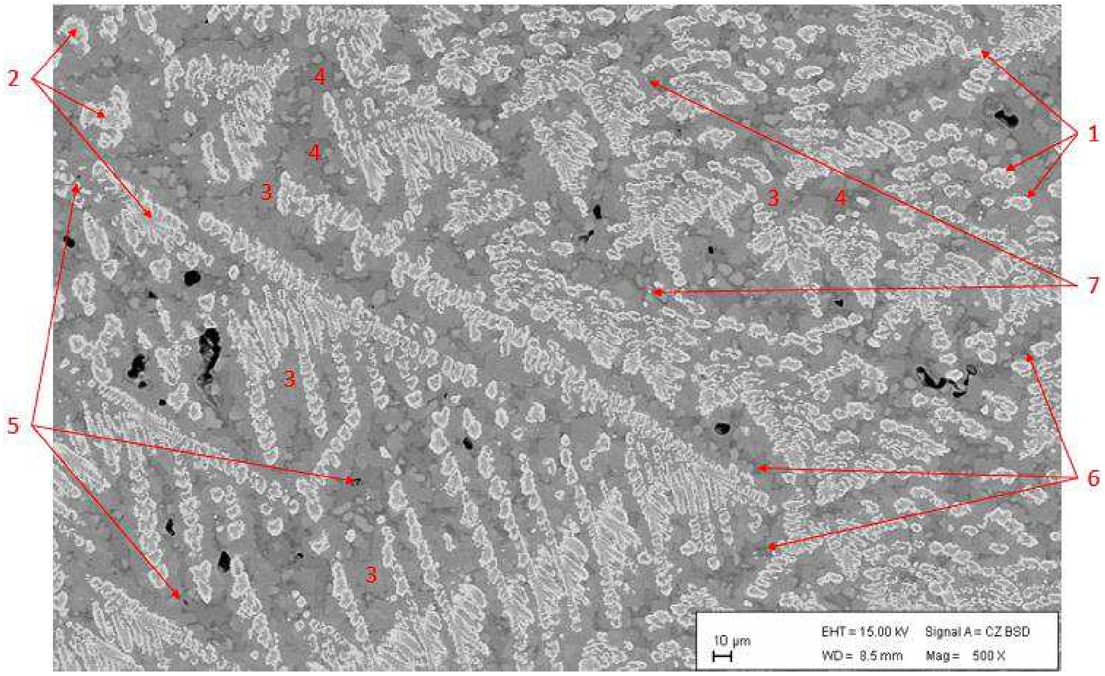

Figure 33. Representative SEM image of E-2018-A033, the phases as marked are:

1….. perovskite
2….. $Ca_2SiO_4$
3….. $Na_2CaSiO_4$
4….. combeite
5….. kalsilite
6….. $K_2MgSiO_4$
7….. forsterite

The XRD result for slag A040 is shown in Figure 34. A concave indicating the presence of significant glassy phase was obvious immediately after the FCT-test (Figure 35).

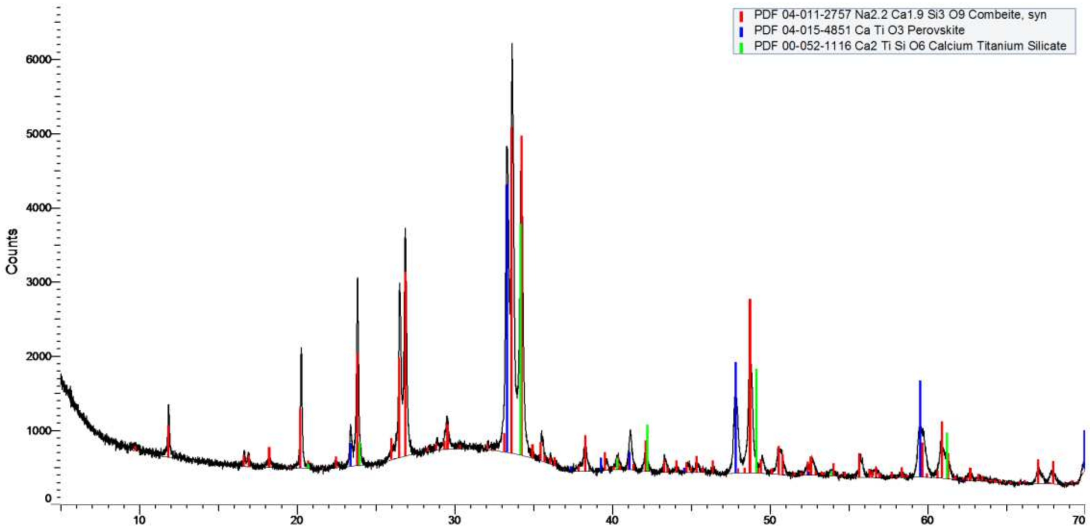

Figure 34. XRD result from FCT specimen of E-2018-A040

Figure 35. FCT sample of E-2018-A040

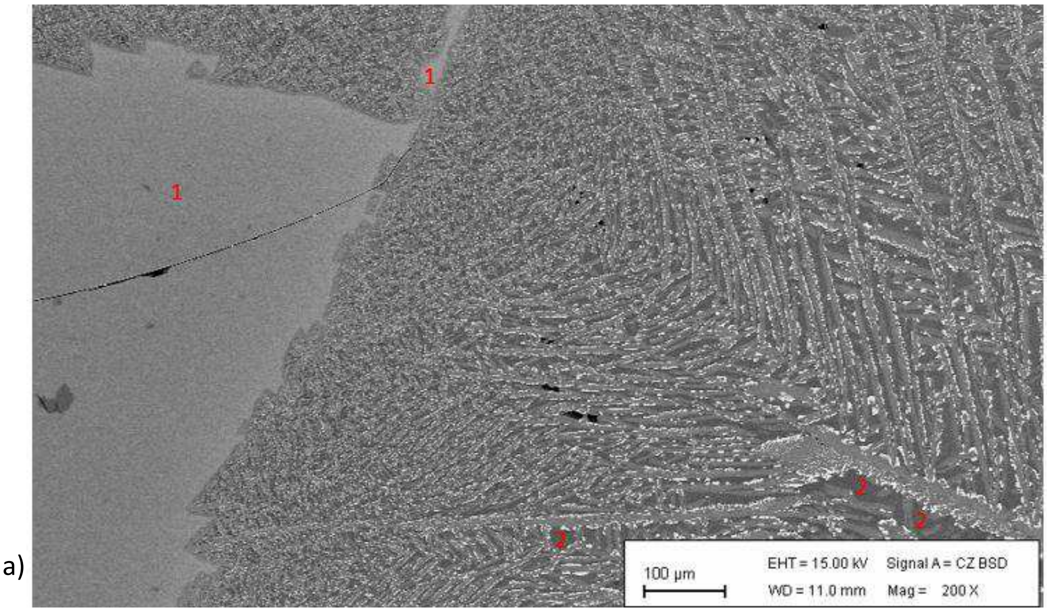

Figure 36a. Representative SEM image 1 of E-2018-A040, the phases as marked are:

1….. main glassy phase 2….. residual glassy phase b)

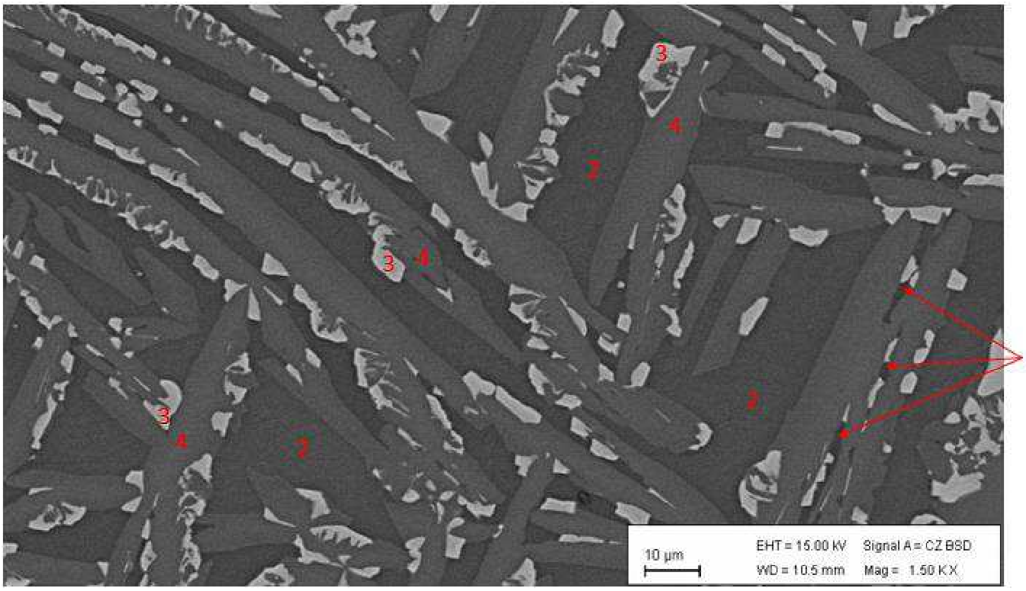

Figure 36b. Representative SEM image 2 of E-2018-A040, the phases as marked are:
2….. residual glassy phase 3….. perovskite
4….. calcium titanium silicate 5….. combeite

The presence of glassy phase in the FCT specimen is confirmed by the representative SEM image shown in Figure 36a. The main glassy phase with a continuous surface in the lower left corner, marked as 1, has the chemical composition of 7.5 wt% $Na_2O$, 3 % $K_2O$, 34 % CaO, 2 % MgO, 29.5 % $SiO_2$, 4.5 % $TiO_2$, and 19 % $B_2O_3$. SEM results indicate that this glassy phase is chemically homogeneous. The particle size of the glassy phase in the lower left corner is observed to be above 2 mm, indicating that slag A040 likely has low devitrification tendency. Residual glassy phase embedded close to the crystallized slag is also found in Figure 35 and Figure 36, marked as 2. It has the molar chemical composition of 5.5 wt% $Na_2O$, 8.5 % $K_2O$, 21.5 % CaO, 6 % MgO, 26.5 % $SiO_2$, 3 % $TiO_2$, and 28 % $B_2O_3$.

The crystalline phases of A040 FCT specimen are marked in Figure 36b. The white phase is perovskite, marked as 3. The needle-like crystal phase is calcium titanium silicate, marked as 4. This is the main crystal phase, which is found in slag A002; it shows dendritic crystal growth. Perovskite grows on the surface of the calcium titanium silicate. A minor phase, marked as 5, is combeite, which has the darkest color. These crystalline phases are boron-free, which explains the high concentration of boron in the residual glassy phase. The dendritic growth of the crystals no longer involves $C_2S$, which is desirable. The absence of $C_2S$ is likely the main reason for the low crystallization tendency.

Overall it could be observed that the presence of $C_2S$ is the most detrimental factor for increasing crystallization tendency. It appears that the paragenesis of $C_2S$ is connected to the presence of $Al_2O_3$, even if the molar A/S ratio is as low as 0.075. Optical basicity is a less influential factor, as slags A002 and A033 have the same $\Lambda_{th}$, but A033 has high crystallization tendency due to its $Al_2O_3$ contents. However, it still plays a role, as slag A015 likely exhibits more rapid crystallization than A010 due to its higher $\Lambda_{th}$.

### 4.1.5. SHTT and TTT-diagram

In the SHTT test the slag of composition A002 is observed to be completely liquidus at above 1130 °C, which agrees with the DTA result. The TTT-diagram for slag A002 is shown in Figure 37. The nose temperature is between 900 and 850 °C. The time of onset of crystallization ($t_{0.5}$) at 900 °C is at 3.6 ± 0.8 sec, and $t_{95}$ is 22 ± 3 sec, which are not remarkable in terms of low crystallization tendency. However, at 1000 and 750 °C, $t_{0.5}$ and $t_{95}$ become magnitudes larger.

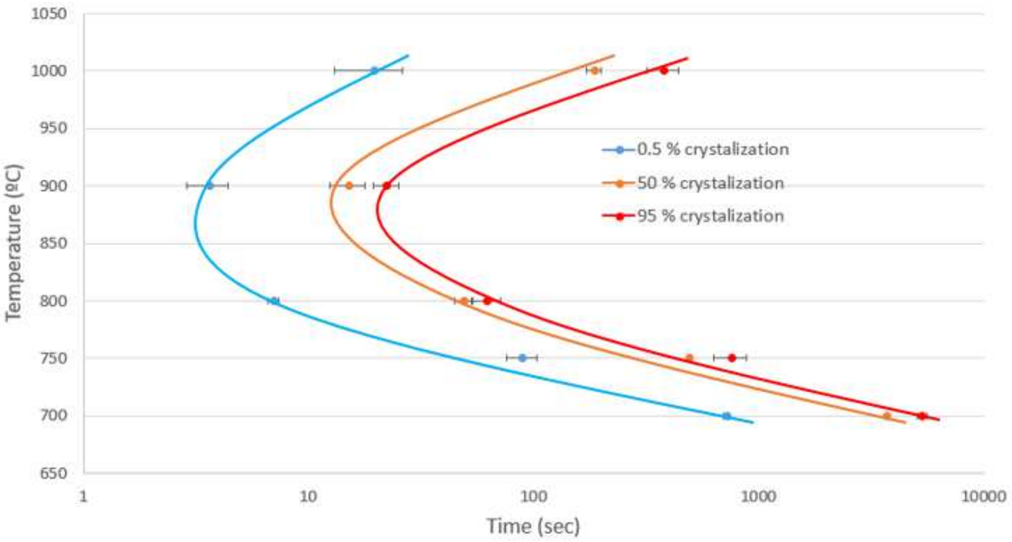

Figure 37. TTT diagram of E-2018-A002

The TTT-diagram for composition A040 is shown in Figure 38. The nose temperature is between 700 and 750 °C. The nose temperature is relatively low, which explains the relatively fine crystal grains in the A040 FCT specimen. At 700 °C, $t_{0.5}$ is 6.1 ± 1.3 sec, and $t_{95}$ is 44 ± 13 sec. This represents a 2-fold decrease in crystallization tendency when compared to slag A002. This decrease is due to the significant decrease in optical basicity as $B_2O_3$ is introduced into the system.

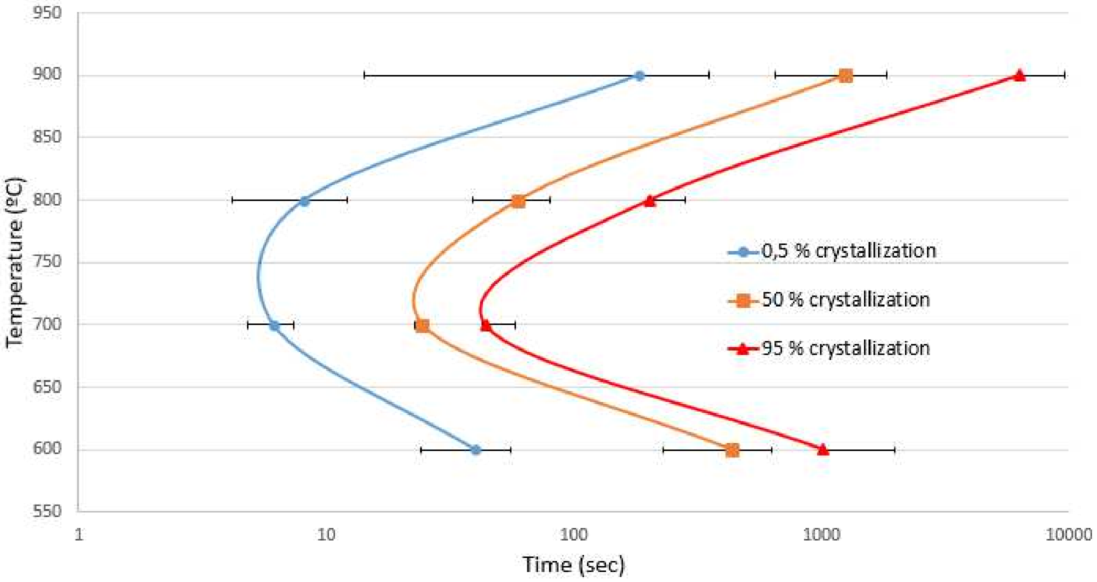

Figure 38. TTT diagram of E-2018-A040

For $Al_2O_3$-containing slags, the crystallization process is observed to be rapid even at 700 and 1000 °C. This is probably due to the precipitation of $C_2S$ crystals. It was observed, however, that slag A015 crystallizes the most rapid of all, possibly due to it having the highest optical basicity. Due to their rapid crystallization, it was unnecessary to construct TTT diagrams for these compositions. The last solids of slag A010, A015, and A018 are all observed during SHTT test to be dissolved at 1300 °C.

### 4.1.6. Summary for the soda-lime-silicate slag system

The effect of addition of $Al_2O_3$, $B_2O_3$, MnO and FeO on the proposed soda-lime-silicate slag system has been investigated. The results are certainly not conclusive, but some important information can be garnered. The properties of the investigated slags are summarized in Table 13.

Table 13. Properties of the investigated soda-lime-silicate slags

| slag | A/S mol/mol | B/S mol/mol | MnO and FeO wt% | $\Lambda_{th}$ [1] | $T_{br}$ ºC | last solid ºC | viscosity at 1300 ºC poise |
|---|---|---|---|---|---|---|---|
| A002 | 0 | 0 | 0 | 0.707 | 1038 | 1161 | 4.48 |
| A040 | 0 | 0.15 | 0 | 0.675 | 953 | 1188 | 2.21 |
| A010 | 0.075 | 0 | 0 | 0.721 | 1148 | 1339 | 3.18 |
| A015 | 0.15 | 0 | 0 | 0.734 | 1116 | 1327 | 3.24 |
| A018 | 0.075 | 0 | 0.8 | 0.721 | 1157 | 1341 | 0.97 |
| A033 | 0.075 | 0.075 | 0 | 0.707 | 1152 | 1278 | 2.57 |

| slag | mineralogical composition of FCT specimen |
|---|---|
| A002 | glassy phase, bredigite, $Ca_2TiSiO_6$, $Ca_2(Ti,Si)SiO_6$, $NC_2S_3$ |
| A040 | two glassy phases, perovskite, $Ca_2TiSiO_6$, combeite |
| A010 | perovskite, $C_2S$, $Na_2TiO_3$, combeite in form of $Na_{1.5}K_{0.5}CaSi_2O_6$, kalsilite |
| A015 | perovskite, $C_2S$, $Na_{1.74}Mg_{0.79}Al_{0.15}Si_{1.06}O_4$, NCS, $NC_2S_2$, kalsilite |
| A018 | perovskite, $C_2S$, $Na_2TiO_3$, combeite, kalsilite, $K_2MgSiO_4$, sanidine, merwinite |
| A033 | perovskite, $C_2S$, NCS, combeite, kalsilite, $K_2MgSiO_4$, $M_2S$ |

Slag A002 exhibits satisfactory properties, except for its viscosity at 1300 °C being too high. It shows low crystallization tendency, as evidenced by its FCT specimen containing residual glassy phase. The paragenesis of bredigite instead of $C_2S$ is likely favorable to lowering crystallization tendency and $T_m$, as the compositions showing precipitation of $C_2S$ all exhibit high crystallization tendency. The solidified slag does not exhibit dendritic growth pattern, and the crystal grains are of relatively small sizes, showing that the driving force of diffusion is relatively low. It would be worthwhile to alter the chemical composition of A002 to reduce its viscosity to achieve a satisfactory composition. The effects of the addition of other oxides on A002 are summarized in the following:

The addition of $Al_2O_3$ into this system has produced few desirable results. GFA is negatively impacted if the C/S ratio is not adjusted according to the alumina content as prescribed in equation 31. When compared to slag A002, slags A010 and A018 experience an increase of $T_{br}$

by 110 °C, and an increase of temperature of last crystals by 180 °C, due to having an A/S molar ratio of 0.075. This is due to the formation of $C_2S$, which also results in significant increase in crystallization tendency, as evidenced by the dominant feature of dendritic growth of $C_2S$ and perovskite in the FCT specimen of alumina-containing slags. However, the increase in A/S molar ratio from 0.075 to 0.15 does not appear to have a significant impact on $T_m$ and $T_{br}$.

The one property favorably affected by the addition of $Al_2O_3$ is viscosity, as A010 and A015 have viscosity at 1300 °C reduced by about 1.2 poise compared to A002. However, this benefit is moot as alumina content must be reduced to the point that the crystallization of $C_2S$ is not preferred. It would be interesting to investigate doping composition A002 with an A/S molar ratio of 1/80, which would result in an $Al_2O_3$ content of almost exactly 0.8 wt% (Table 15), to observe the mineralogy and whether a reduction in viscosity due to entropy considerations is possible.

The addition of MnO and FeO has no significant impact on optical basicity, which should mean that they have no significant impact on GFA. However, the addition of MnO and FeO in the absence of $Al_2O_3$ was found to negatively affect GFA. When acting as a network former, $Al_2O_3$ is known from literature study to have the effect of stabilizing the glass matrix, which could be the reason for this phenomenon.

MnO and FeO does not exhibit a notable effect on $T_{br}$ and $T_m$, which is due to them not significantly altering mineralogy with only 0.8 wt% content. It was hypothesized that Mn and Fe would be incorporated into the lattices of major crystal phases as a solid solution. This was not the case however, and three minor phases including sanidine, are present in A018 while being absent in A010, although they are minor phases. It is not clear how this will affect the crystallization tendency of the slag, as the crystallization mechanism of A018 is dominated by $C_2S$-formation. However, sanidine of feldspar group is an indicator of high devitrification tendency according to literature [134, 135].

It would be interesting to dope slag A002 with 0.8 wt% of FeO, MnO, and $Al_2O_3$ to observe the change in viscosity and mineralogy. The addition of $Al_2O_3$ alongside FeO and MnO will result in high GFA, and the formation of sanidine should not be possible in an Al-deficient slag.

Slag A033 has similar composition to A010, and has a $B_2O_3$ introduced with a B/S molar ratio of 0.075. The boron content brings down the eutectic point of the composition. A significant reduction of 0.6 poise in viscosity at 1300 °C is experienced. GFA is negatively impacted if the C/S ratio is not adjusted according to the alumina content as prescribed in equation 32.

However, comparing A010 and A033, $T_{br}$ has not been affected by the boron content. This is likely due to the crystallization mechanism still being dominated by the $C_2S$ phase formation, which is caused by the alumina content. The dendritic growth of perovskite and $C_2S$ is still dominant in the A033 FCT specimen.

Slag A002 and A033 have the same optical basicity at 0.707. However, A033 has higher crystallization tendency compared to A002. This suggests that optical basicity is a less important indicator of crystallization tendency compared to phase formation.

Slag A040 shows a reduction of viscosity from 4.48 to 2.21 poise at 1300 °C when compared to A002. The $t_{0.5}$ and $t_{95}$ at respective nose temperatures are doubled, indication of a significant reduction in crystallization tendency. The nose temperature of slag A002 is between 850 and 900 °C, while for slag A040 it is between 700 and 750 °C. This suggests that the phases involved in the nucleation step of crystal growth are perhaps different. This is supported by the fact that the dominant crystals in A040 are the dendritic perovskite and $Ca_2TiSiO_6$. The undesirable phase $C_2S$ is totally avoided, which results in low crystallization tendency. It is likely that as $B_2O_3$ content rises, the crystallization tendency would further decrease due to the drop in optical basicity. According to literature study the paragenesis of phases $C_2BS$ and $C_{11}BS_{14}$ should have been possible in A040, as the FCT specimen has 5.3 wt% $B_2O_3$ content [109, 110].

## 4.2. High-alkaline boroaluminate slag system

### 4.2.1 Quenching results and selection of compositions

The proposed slag compositions within the high-alkaline boroaluminate slag system are listed in Table 14. For the molar compositions please refer to Table B4 in Appendix B. The quenched slags are shown in Figure 39, all of which exhibit high GFA, as no crystallization could be observed. The high GFA is likely due to the very low optical basicity of the compositions.

Table 14. High-alkaline boroaluminate slag system

| slag serial [wt%] | $SiO_2$ | CaO | $Na_2O$ | MgO | $TiO_2$ | $Al_2O_3$ | $B_2O_3$ | $\Lambda_{th}$ |
|---|---|---|---|---|---|---|---|---|
| E-2018-A0123 | 0 | 15.36 | 0 | 14.19 | 0 | 15.36 | 54.49 | 0.541 |
| E-2018-A0124 | 0 | 15.05 | 2.09 | 12.83 | 4.04 | 14.95 | 51.04 | 0.552 |
| E-2018-A0125 | 0 | 13.70 | 4.12 | 12.03 | 7.97 | 17.30 | 44.88 | 0.559 |
| E-2018-A0126 | 0 | 11.40 | 6.08 | 12.10 | 11.76 | 19.24 | 39.42 | 0.585 |
| E-2018-A0130 | 8.76 | 15.37 | 2.71 | 12.46 | 5.24 | 14.86 | 40.60 | 0.567 |
| E-2018-A0131 | 13.44 | 15.81 | 2.22 | 12.69 | 4.29 | 15.21 | 36.35 | 0.570 |
| E-2018-A0132 | 17.68 | 15.42 | 2.92 | 12.63 | 5.64 | 15.00 | 30.72 | 0.580 |
| E-2018-A0137 | 22.32 | 17.12 | 0 | 13.74 | 0 | 16.47 | 30.36 | 0.571 |
| E-2018-A0138 | 26.37 | 17.14 | 0 | 13.89 | 0 | 16.57 | 26.03 | 0.576 |

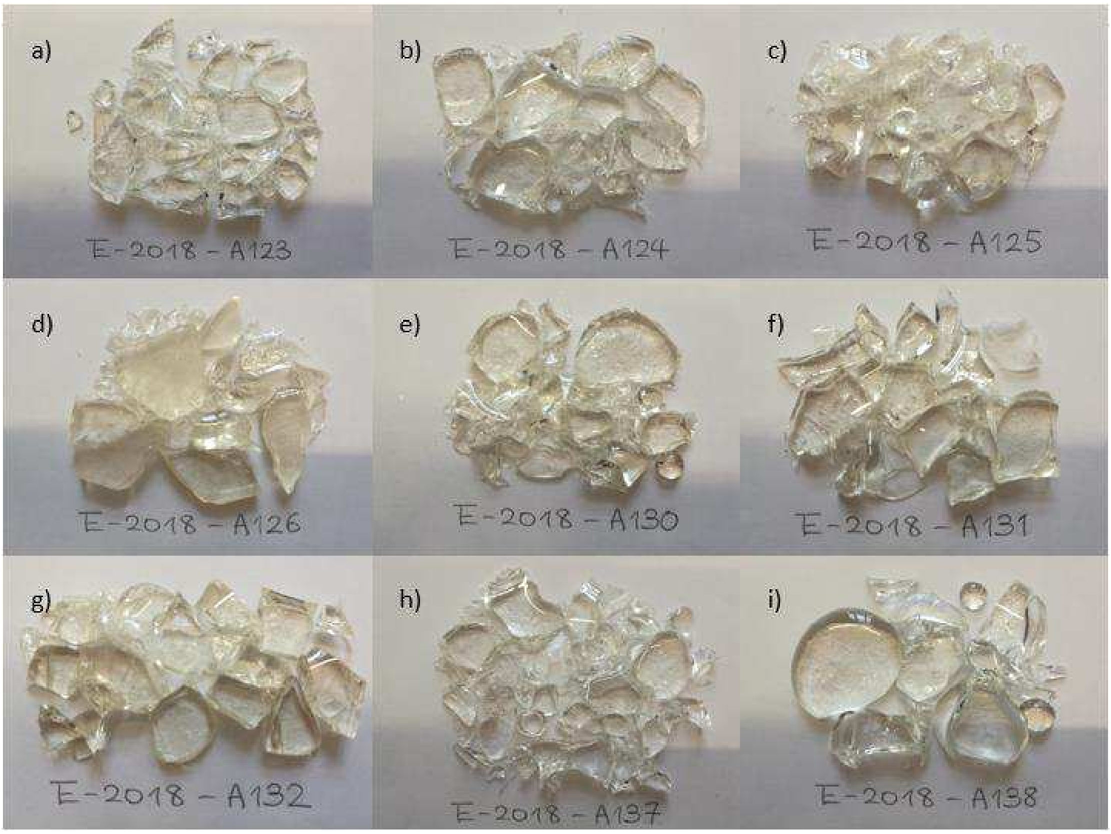

Figure 39. Quenched slags of a) A123, b) A124, c) A125, d) A126, e) A130, f) A131, g) A132, h) A137, and i) A138.

Although all the quenching results are promising, only compositions A124 and A138 are selected for further testing. The testing of the slag compositions has proved difficult. During FCT the melted slags have been observed to creep up the sides of the platinum crucible. The cooled FCT specimens were completely stuck to the crucible and could not be separated. Therefore polished sections have not been produced for A124 and A138. The rheometer test has not been carried out for fear of destroying the set up. The sample loaded onto the SHTT is seen to vaporize volatiles at a rapid rate, and meaningful TTT-diagrams could not be constructed.

### 4.2.2. DTA and FCT

The result of the DTA for composition A124 is shown in Figure D11 and D12 of Appendix D. The last solid is detected at 1024 $^{o}$C, which is much lower than the FactSage prediction of 1160 $^{o}$C. This deviation may be due to the considerable evaporation observed, which accounts for 18 wt% of the sample loaded. The retarded slag shows very low crystallization tendency in the cooling curve of DTA with no obvious local minima. Therefore there is no onset of crystallization temperature. This is expected due to the high boron contents. The FCT result is shown in Figure D6 of Appendix D. There is a local minimum at 602 $^{o}$C during cooling. However, the FCT specimen was totally glassy post-cooling, so this local minimum is not indicative of crystallization.

The boron content of slag A138 is 26 wt%, about half of the boron content of A124. The boron content was replaced by silica. The result of the DTA experiment for A138 is shown in Figure D13 and D14 in Appendix D. Also for the sample, an intense evaporation was observed. According to the cooling curve, of the retarded sample there is a tiny minimum likely indicative of crystallization. The onset of crystallization temperature is 694 $^{o}$C. However, no local minimum is observed in the FCT result shown in Figure D7 of Appendix D. The FCT specimen was visually totally glassy. The difference might be attributable to a 12 wt% sample loss during DTA due to evaporation.

In both cases, it seems that the slags remain chemically stable below 800 $^{o}$C. If boron could not be harmful to product quality, it would make sense to investigate the slag after the evaporation of volatile components, since neither of the retarded slags showed any signs of crystallization.

## 5. Summary

The goal of this master thesis is to develop $CaF_2$-free mould slag compositions having melting points below 1250 °C, a viscosity below 3 poise at 1300 °C, and relatively low crystallization tendency. Following results could be found for the investigated slags:

A boron-free composition (A002) within the soda-lime-silicate system has been found to be relatively satisfactory. Its chemical composition in wt% is 39.22% $SiO_2$, 31.39% CaO, 11.53% $Na_2O$, 5.84% $K_2O$, 3.03% MgO, and 8.99% $TiO_2$. Its $T_m$ is 1161 °C, but its viscosity at 1300 °C is 4.48 poise. Its nose temperature is 900 °C, at which point $t_{0.5}$ is 3.6 ± 0.8 sec, and $t_{95}$ is 22 ± 3 sec. Improvements are needed in regards to viscosity.

Alumina content at A/S molar ratio of 0.075 and 0.015 results in the paragenesis of $C_2S$ as a major phase, which significantly raises the temperature where the last crystalline phases liquefies and also the crystallization tendency. Viscosity is significantly lowered at 1300 °C compared to A002.

The addition of small amounts of MnO and FeO did not affect the temperature of last solid, but the paragenesis of sanidine, merwinite, and $K_2MgSiO_4$ as minor phases is detected. The viscosity was significantly lowered. MnO and FeO seems to reduce GFA in the absence of $Al_2O_3$.

$B_2O_3$ content at $B_2O_3/SiO_2$ molar ratio of 0.075 significantly reduces viscosity and the temperature of last solid. The paragenesis of boron-containing phases is not detected.

A boron-containing composition within the soda-lime-silicate system has been found to satisfy the criteria. Its chemical composition in wt% is 37.23% $SiO_2$, 26.66% CaO, 12.27% $Na_2O$, 6.21% $K_2O$, 2.81% MgO, 8.35% $TiO_2$, and 6.47% $B_2O_3$. Its $T_m$ is 1188 °C, and its viscosity at 1300 °C is 2.21 poise. Its nose temperature is 700 °C, at which point $t_{0.5}$ is 6.1 ± 1.3 sec, and $t_{95}$ is 44 ± 13 sec. This mould slag may be used in the continuous casting of steel, if the boron content does not negatively affect steel quality due to possible redox reaction with alloying elements.

## 6. Outlook

The results from soda-lime-silicate system has shown some promising results. Development should focus on reducing the viscosity of slag A002 at 1300 °C, as this composition is $B_2O_3$-free and exhibits relatively low crystallization tendency. Another focus should be on reducing the boron content of A040, as this composition has satisfied the requirements set out in the problem definition. The following slag compositions (molar compositions in Table B5, Appendix B) are proposed in order to find a more satisfying composition:

Table 15. Proposed slag compositions for further investigation

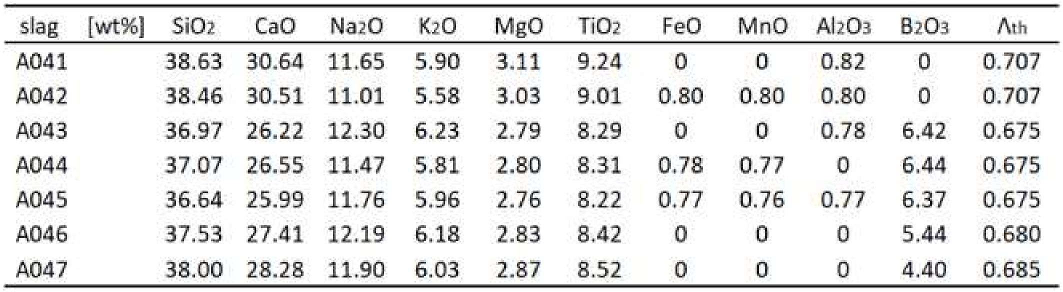

| slag | [wt%] | $SiO_2$ | CaO | $Na_2O$ | $K_2O$ | MgO | $TiO_2$ | FeO | MnO | $Al_2O_3$ | $B_2O_3$ | $\Lambda_{th}$ |
|---|---|---|---|---|---|---|---|---|---|---|---|---|
| A041 | | 38.63 | 30.64 | 11.65 | 5.90 | 3.11 | 9.24 | 0 | 0 | 0.82 | 0 | 0.707 |
| A042 | | 38.46 | 30.51 | 11.01 | 5.58 | 3.03 | 9.01 | 0.80 | 0.80 | 0.80 | 0 | 0.707 |
| A043 | | 36.97 | 26.22 | 12.30 | 6.23 | 2.79 | 8.29 | 0 | 0 | 0.78 | 6.42 | 0.675 |
| A044 | | 37.07 | 26.55 | 11.47 | 5.81 | 2.80 | 8.31 | 0.78 | 0.77 | 0 | 6.44 | 0.675 |
| A045 | | 36.64 | 25.99 | 11.76 | 5.96 | 2.76 | 8.22 | 0.77 | 0.76 | 0.77 | 6.37 | 0.675 |
| A046 | | 37.53 | 27.41 | 12.19 | 6.18 | 2.83 | 8.42 | 0 | 0 | 0 | 5.44 | 0.680 |
| A047 | | 38.00 | 28.28 | 11.90 | 6.03 | 2.87 | 8.52 | 0 | 0 | 0 | 4.40 | 0.685 |

Slag A041 and A042 are developments of slag A002 with the same optical basicity as A002. A041 introduces $Al_2O_3$ at a small dosage of 0.8 wt% into A002, in order to examine whether the paragenesis of $C_2S$ will take place, and if small amount of $Al_2O_3$ will lead to a significant reduction in viscosity due to entropy consideration. For A042, 0.8 wt% each of MnO, FeO, and $Al_2O_3$ are introduced into A002, in order to examine whether the reduction of viscosity as observed for A018 could be repeated, and to examine the effect of MnO and FeO on GFA and crystallization tendency. A successful composition would result in a boron-free slag in the soda-lime-silicate system.

If boron presents no negative impact on steel quality, further investigations into A040 may prove useful. Slag A043 to A045 are developments of slag A040 with the same optical basicity as A040. It would be interesting to compare the viscosities of these slags in order to investigate the effect of small contents of $Al_2O_3$, FeO, and MnO on A040. These three compositions are very similar to A040, so that they likely have similar mineralogical compositions and low crystallization tendency.

Slag A046 reduces the B/S ratio to 0.125. It has a basic to non-basic molar ratio of 1.025, making it a basic slag so that Ti acts as network former. It would be interesting to examine the changes in mineralogy and crystallization tendency compared to A040. In the literature study it was suggested that the optimum $B_2O_3$ content for reducing viscosity is up to 4.4 wt%. Slag A047 is designed to examine a slag with this particular boron content.

## List of References

1. Wolf M.M., “Making, Shaping and Treating of Steel: Casting Volume”, Association of Iron and Steel Engineers, 11th ed., (2003), Chapter 1, pp. 1-38.
2. Fredriksson H., Åkerlind U., “Materials Processing During Casting”, Wiley, 1st ed., (2006), pp. 1-138.
3. Sahai Y., Emi T., “Tundish Technology for Clean Steel Production”, World Scientific Publishing Company, 1st ed., (2007).
4. Thomas B.G., “Making, Shaping and Treating of Steel: Casting Volume”, Association of Iron and Steel Engineers, 11th ed., (2003), Chapter 14, pp. 1-41.
5. Mills K.C., Fox A.B., Thackray R.P., Li Z., “ Performance and Properties of Mould Fluxes”, Ironmaking and Steelmaking, Vol. 32, No. 1, 2005, pp. 26-34.
6. Mills K.C., “Making, Shaping and Treating of Steel: Casting Volume”, Association of Iron and Steel Engineers (AISE), Pittsburgh, 11th ed., (2003), Chapter 8, pp. 1-41.
7. Thomas, B.G., 2002. Modeling of the continuous casting of steel—past, present, and future. Metallurgical and materials transactions B, 33(6), pp.795-812.
8. Sridhar, S., Mills, K.C., Afrange, O.D.C., Lörz, H.P. and Carli, R., 2000. Break temperatures of mould fluxes and their relevance to continuous casting. Ironmaking & steelmaking, 27(3), pp.238-242.
9. Cho, J., Shibata, H., Emi, T. and Suzuki, M., 1998. Radiative heat transfer through mold flux film during initial solidification in continuous casting of steel. ISIJ international, 38(3), pp.268-275.
10. Choi, S.Y., Lee, D.H., Shin, D.W., Choi, S.Y., Cho, J.W. and Park, J.M., 2004. Properties of F-free glass system as a mold flux: viscosity, thermal conductivity and crystallization behavior. Journal of non-crystalline solids, 345, pp.157-160.
11. Cho, J.W., Emi, T., Shibata, H. and Suzuki, M., 1998. Heat transfer across mold flux film in mold during initial solidification in continuous casting of steel. ISIJ international, 38(8), pp.834-842.
12. Cruz, A., Chavez, F., Romero, A., Palacios, E. and Arredondo, V., 2007. Mineralogical phases formed by flux glasses in continuous casting mould. Journal of materials processing technology, 182(1-3), pp.358-362.
13. He, S.P., Huang, Q.Y., Zhang, G.X., Lu, Y.J. and Qian, W.A.N.G., 2011. Solidification properties of Cao-Sio2-Tio2 based mold fluxes. Journal of Iron and Steel Research, International, 18(7), pp.15-52.
14. Zhou, L., Wang, W., Lu, B., Wen, G. and Yang, J., 2015. Effect of basicity and B2O3 on viscosity, melting and crystallization behaviors of low fluorine mold fluxes for casting medium carbon steels. Metals and Materials International, 21(1), pp.126-133.
15. Romo-Castañeda, J., Cruz-Ramírez, A., Romero-Serrano, A., Vargas-Ramírez, M. and Hallen-López, M., 2011. Thermodynamic modeling of mineralogical phases formed by continuous casting powders. Thermochimica acta, 512(1-2), pp.129-133.
16. Bezuidenhout, G.A., 1999. The effect of alumina pick-up on mould flux behaviour in continuous casting.
17. Fruehan R. J., “The Making, Shaping and Treating of Steel”, Association of Iron and Steel Engineers, Pittsburgh, 11th ed., (1998), pp. 79-104.

18. Seo, M.D., Shi, C.B., Wang, H., Cho, J.W. and Kim, S.H., 2015. Non-isothermal melt crystallization of cuspidine in CaO–SiO2–CaF2 based glasses. Journal of Non-Crystalline Solids, 412, pp.58-65.
19. Görnerup, M., Hayashi, M., Däcker, C.Å. and Seetharaman, S., 2004, January. Mould fluxes in continuous casting of steel–characterization and performance tuning. In Proc. 7th Int. Conf. on Molten Slags, Fluxes and Salts, Cape Town (pp. 745-752). The South African Institute of Mining and Metallurgy.
20. Verlag Stahleisen, “Slag Atlas”, Germany, 2nd ed., (October 1995).
21. Mills, K. Mold powder for continuous casting. IAS (Instituto Argentino de Siderurgia) seminar, San Nicolas, Argentina, August 2003.
22. Persson, M., Seetharaman, S., and Seetharaman, S. Kinetic Studies of Fluoride Evaporation from Slags. *ISIJ Int*, 2007, vol. 47, pp. 1711-1717.
23. Carli, R., Righi, C., and Giacobbe, A. Mold fluxes fluoride content, some technological considerations. *13th IAS seminar*.
24. RUSŇÄKOVÄ, V., Kijac, J., Grimplini, G. and RUSŇÁK, G., 2010. ANALYSIS OF SLAG IN MOLD UNDER STANDARD CONDITIONS AND IN CASE OF STICKER TEMPERATURE ALARM OCCURENCE. ACTA METALLURGICA SLOVACA, 16(3), pp.172-180.
25. Fox, A.B., Mills, K.C., Lever, D., Bezerra, C., Valadares, C., Unamuno, I., Laraudogoitia, J.J. and Gisby, J., 2005. Development of fluoride-free fluxes for billet casting. ISIJ international, 45(7), pp.1051-1058.
26. Kim, G.H. and Sohn, I., 2012. Influence of Li2O on the viscous behavior of CaO–Al2O3–12 mass% Na2O–12 mass% CaF2 based slags. ISIJ international, 52(1), pp.68-73.
27. Saraswat, R., Maijer, D.M., Lee, P.D. and Mills, K.C., 2007. The effect of mould flux properties on thermo-mechanical behaviour during billet continuous casting. ISIJ international, 47(1), pp.95-104.
28. Wang, Y., Sakamaki, T., Skinner, L.B., Jing, Z., Yu, T., Kono, Y., Park, C., Shen, G., Rivers, M.L. and Sutton, S.R., 2014. Atomistic insight into viscosity and density of silicate melts under pressure. Nature Communications, 5, p.3241.
29. Zhang, Z., Wen, G., Tang, P. and Sridhar, S., 2008. The influence of Al2O3/SiO2 ratio on the viscosity of mold fluxes. ISIJ international, 48(6), pp.739-746.
30. Kalisz, D., 2014. Modeling physicochemical properties of mold slag. Archives of Metallurgy and Materials, 59(1), pp.149-155.
31. Bezuidenhout, Gert Adrian. "The effect of alumina pick-up on mould flux behaviour in continuous casting." (1999).
32. Jiang, Z.H. and Zhang, Q.Y., 2014. The structure of glass: A phase equilibrium diagram approach. Progress in Materials Science, 61, pp.144-215.
33. Le Losq, C. and Neuville, D.R., 2017. Molecular structure, configurational entropy and viscosity of silicate melts: Link through the Adam and Gibbs theory of viscous flow. Journal of Non-Crystalline Solids, 463, pp.175-188.
34. Brandaleze, E., Di Gresia, G., Santini, L., Martin, A., and Benavidez, E. Science and Technology of Casting Process. Chapter 7. Mould flux in steel continuous casting process. 2012, pp. 205-333.
35. Doweidar, H., 1990. Consideration of the boron oxide anomaly. Journal of materials science, 25(1), pp.253-258.

36. Dingwell, D.B., Knoche, R., Webb, S.L. and Pichavant, M., 1992. The effect of B2O3 on the viscosity of haplogranitic liquids. American Mineralogist, (5-6), pp.457-461.
37. Zhen, Y.L., Zhang, G.H. and Chou, K.C., 2014. Influence of Al2O3/TiO2 ratio on viscosities and structure of CaO–MgO–Al2O3–SiO2–TiO2 melts. ISIJ international, 54(4), pp.985-989.
38. Limbach, R., Karlsson, S., Scannell, G., Mathew, R., Edén, M. and Wondraczek, L., 2017. The effect of TiO2 on the structure of Na2O-CaO-SiO2 glasses and its implications for thermal and mechanical properties. Journal of Non-Crystalline Solids, 471, pp.6-18.
39. Kukharenko, S.A., Shilo, A.E., Itsenko, P.P. and Kutsai, A.N., 2010. The effect of titanium dioxide on the structure of silicate multicomponent glasses. Journal of Superhard Materials, 32(6), pp.396-405.
40. LaCourse, W.C. and Cormack, A.N., 1991. Structural influences on the mixed alkali effect in glasses. Tran. Am. Crystallogr. Assoc, 27, pp.211-224.
41. Brook, H.C., Chadwick, A.V., Mosslemans, J.F.W. and Greaves, G.N., 1999. EXAFS study of a “mixed-alkali” type effect in sodium-calcium borate glass. Radiation Effects and Defects in Solids, 150(1-4), pp.403-407.
42. Müller, R., Zanotto, E.D. and Fokin, V.M., 2000. Surface crystallization of silicate glasses: nucleation sites and kinetics. Journal of non-crystalline solids, 274(1-3), pp.208-231.
43. Iida, T., Sakai, H., Kita, Y. and Shigeno, K., 2000. An equation for accurate prediction of the viscosities of blast furnace type slags from chemical composition. ISIj International, 40(Suppl), pp.S110-S114.
44. Iida, T., Sakai, H., Kita, Y. and Murakami, K., 2000. Equation for estimating viscosities of industrial mold fluxes. High Temperature Materials and Processes, 19(3-4), pp.153-164.
45. Urbain, G., 1987. Viscosity estimation of slags. Steel research, 58(3), pp.111-116.
46. Dong, X.J., Sun, H.Y., She, X.F., Xue, Q.G. and Wang, J.S., 2014. Viscosity and viscosity estimation model of fully liquid slags in TiO2–Al2O3–CaO–SiO2 and TiO2–Al2O3–CaO–SiO2–MgO systems with high TiO2 concentration and low mass ratio of CaO to SiO2. Ironmaking & steelmaking, 41(2), pp.99-106.
47. Mills, K.C. and Sridhar, S., 1999. Viscosities of ironmaking and steelmaking slags. Ironmaking & Steelmaking, 26(4), pp.262-268.
48. Mills, K.C., Chapman, L., Fox, A.B. and Sridhar, S., 2001. Round robin program for slag viscosity estimation. Scand. J. Metallurgy, 30(6), pp.396-404.
49. Kekkonen, M., Oghbasilasie, H. and Louhenkilpi, S., 2012. Viscosity models for molten slags.
50. Ray, H.S. and Pal, S., 2004. Simple method for theoretical estimation of viscosity of oxide melts using optical basicity. Ironmaking & steelmaking, 31(2), pp.125-130.
51. Shankar, A., Görnerup, M., Lahiri, A.K. and Seetharaman, S., 2007. Estimation of viscosity for blast furnace type slags. Ironmaking & steelmaking, 34(6), pp.477-481.
52. Kozmidis-Petrović, A.F., 2015. Dynamic fragility and reduced glass transition temperature as a pair of parameters for estimating glass forming ability. Journal of Non-Crystalline Solids, 417, pp.1-9.
53. Sridhar, S., Mills, K.C., Afrange, O.D.C., Lörz, H.P. and Carli, R., 2000. Break temperatures of mould fluxes and their relevance to continuous casting. Ironmaking & steelmaking, 27(3), pp.238-242.

54. Reddy, R., Chaubal, P., Pistorius, P.C. and Pal, U. eds., 2017. Advances in Molten Slags, Fluxes, and Salts: Proceedings of the 10th International Conference on Molten Slags, Fluxes, and Salts 2016. Springer.
55. Marschall, I., Kölbl, N., Harmuth, H. and Xia, G., 2013. Investigation of continuous casting slag films sampled on site and comparison with laboratory results. Journal for Manufacturing Science & Production, 13(1-2), pp.103-114.
56. KIRCHER, V., MARSCHALL, I., KÖLBL, N. and HARMUTH, H., IMPACT OF AN INCREASE OF Al2O3, TiO2 and ZrO2 ON MOLD SLAG PROPERTIES.
57. Zhou, L., Wang, W. and Zhou, K., 2016. A Study of the Heat Transfer Behavior of Mold Fluxes with Different Amounts of Al2O3. Metals, 6(6), p.139.
58. Nabiałek, M., 2016. Reduced glass-transition temperature versus glass-forming ability in amorphous alloys. Archives of Metallurgy and Materials, 61(4), pp.1957-1962.
59. Hartlep, T. and Ripoll, J.F., 2008. Rayleigh-Bénard convection at Pr= 120 and Ra= 106 in a large aspect ratio domain. In Center for Turbulence Research Proceedings of the Summer Program (pp. 411-416).
60. Stewart, B., McDonald, M., Hopkins, M. and Burniston, R., 2009. Understanding the role of mould slag and slag film in surface quality of continuously cast semis. la metallurgia italiana, (7).
61. Gu, K., Wang, W., Wei, J., Matsuura, H., Tsukihashi, F., Sohn, I. and Min, D.J., 2012. Heat-transfer phenomena across mold flux by using the inferred emitter technique. Metallurgical and Materials Transactions B, 43(6), pp.1393-1404.
62. Diao, J., Xie, B. and Xiao, J.P., 2009. Experimental investigation into radiative heat transfer characteristics for mould fluxes containing transition oxides. Ironmaking & Steelmaking, 36(8), pp.610-614.
63. Guang-Hua, W.E.N., Hui, L.I.U. and Ping, T.A.N.G., 2008. CCT and TTT diagrams to characterize crystallization behavior of mold fluxes. Journal of Iron and Steel Research, International, 15(4), pp.32-37.
64. Zhou, L., Wang, W., Ma, F., Li, J., Wei, J., Matsuura, H. and Tsukihashi, F., 2012. A kinetic study of the effect of basicity on the mold fluxes crystallization. Metallurgical and materials transactions B, 43(2), pp.354-362.
65. Takeuchi, A., Kato, H. and Inoue, A., 2010. Vogel–Fulcher–Tammann plot for viscosity scaled with temperature interval between actual and ideal glass transitions for metallic glasses in liquid and supercooled liquid states. Intermetallics, 18(4), pp.406-411.
66. Harmuth, H. Montanuniversitaet of Leoben. Fundamental of Glass Lectures 2015.
67. Stulov, V.V., 2018. Temperature Differences in the Mold of a Continuous-Casting Machine with a New Cooling System. Steel in Translation, 48(2), pp.78-81.
68. Baird, J.A., Van Eerdenbrugh, B. and Taylor, L.S., 2010. A classification system to assess the crystallization tendency of organic molecules from undercooled melts. Journal of pharmaceutical sciences, 99(9), pp.3787-3806.
69. Semykina, A., Nakano, J., Sridhar, S., Shatokha, V. and Seetharaman, S., 2011. Confocal scanning laser microscopy studies of crystal growth during oxidation of a liquid FeO-CaO-SiO2 slag. Metallurgical and Materials Transactions B, 42(3), pp.471-476.

70. Mills, K.C., Courtney, L., Fox, A.B., Harris, B., Idoyaga, Z. and Richardson, M.J., 2002. The use of thermal analysis in the determination of the crystalline fraction of slag films. Thermochimica acta, 391(1-2), pp.175-184.
71. Klug, J.L., Hagemann, R., Heck, N.C., Vilela, A.C.F. and Scheller, P.R., 2012. Fluorine-free mould slags for slab casting: utilisation of the hot thermocouple technique to build TTT diagrams. Tecnologia em Metalurgia e Materiais, 9(1), pp.30-37.
72. Köbl, N. Montanuniversitaet of Leoben. Laboratory testing method 2 Lectures 2015.
73. Kölbl, N., Harmuth, H., & Marschall, I. (2018). Modified DHTT Equipment for Crystallization Studies of Mold Slags. Metallurgical and Materials Transactions B, 1-11.
74. Elisabeth Bordes-Richard, Pierre Courtine. Optical basicity: a scale of acidity/basicity of solids and its application to oxidation catalysis.. J.L.G. Fierro. Metal Oxides: Chemistry and Applications, CRC Press LLC (Boca Raton, FL, United States), pp.319-352, 2006, Chemical Industries (Volume 108). <hal-00103593>
75. Cha, Y.J., Kim, J.H., Yoon, J.H., Lee, B.S., Choi, S., Hong, K.S., Jeong, E.D., Komatsu, T. and Kim, H.G., 2015. Synthesis, electronic polarizability and β-BaB2O4 crystallization in BaO–B2O3–TeO2 glasses. Journal of Non-Crystalline Solids, 429, pp.143-147.
76. Shankar, A., Görnerup, M., Lahiri, A.K. and Seetharaman, S., 2007. Estimation of viscosity for blast furnace type slags. Ironmaking & steelmaking, 34(6), pp.477-481.
77. Fukushima, T., Benino, Y., Fujiwara, T., Dimitrov, V. and Komatsu, T., 2006. Electronic polarizability and crystallization of K2O–TiO2–GeO2 glasses with high TiO2 contents. Journal of Solid State Chemistry, 179(12), pp.3949-3957.
78. Rodriguez, C.P., McCloy, J.S., Schweiger, M.J., Crum, J.V. and Winschell, A.E., 2011. Optical basicity and nepheline crystallization in high alumina glasses (No. PNNL-20184; EMSP-RPT-003). Pacific Northwest National Lab.(PNNL), Richland, WA (United States).
79. Yang, Y., Wu, P., Men, G. and McLean, A., 2012. Hot Metal Desulphurization Using Waste Residues from the Aluminum Industry.
80. Huang, X.H., Liao, J.L., Zheng, K., Hu, H.H., Wang, F.M. and Zhang, Z.T., 2014. Effect of B2O3 addition on viscosity of mould slag containing low silica content. Ironmaking & Steelmaking, 41(1), pp.67-74.
81. Yang, J., Zhang, J., Sasaki, Y., Ostrovski, O., Zhang, C., Cai, D. and Kashiwaya, Y., 2016. In-situ Study of Crystallisation Behaviour of CaO–SiO2–Na2O–B2O3–TiO2–Al2O3–MgO–Li2O Fluorine-free Mould Fluxes with Different CaO/SiO2 Ratios. ISIJ International, 56(4), pp.574-583.
82. Arefpour, A., Monshi, A., Khayamian, T., Saidi, A. Investigation of viscosity's effects on continuous casting of steel mould powders containing $B_2O_3$, $Li_2O$, $TiO_2$, $Fe_2O_3$, ZnO and $Na_2O$. *Engineering*, 2012, 4, pp. 435-444.
83. Bezerra, M.C.C., Valadares, C.A.G., Rocha, I.P., Bolota, J.R., Carboni, M.C., Scripnic, I.L.M., Santos, C.R., Mills, K., Lever, D. Impact of fluorine free mould flux use on continuous casting process. *37th steelmaking seminar ABM*, Porto Alegre, Brazil, 2006.
84. Fox, A., Mills, K., Lever, D., Bezerra, M.C.C., Valadares, C.A.G., Unamuno, I., Laraudogoitia, J.L., Gisby, J. Devleopment of fluoride-free fluxes for billet casting. Contribution to *XXXVI Steelmaking Seminar–International*. May 2005. Vitória-ES-Brazil.

85. He, S., Long, X., Xu, J., Wu, T., Wang, Q. Effects of crystallization behavior of mould fluxes on properties of liquid slag film. *Ironmaking & Steelmaking*, Volume 39, 2012(8), pp. 593-598.
86. Jiang, B., Wang, W., Sohn, I., Wei, J., Zhou, L., Lu, B. A kinetic study of the effect of ZrO2 and CaO/Al2O3 ratios on the crystallization behavior of a CaO-Al2O3-based slag system. *Metallurgical and Materials Transactions B*, June 2014, 45(3), pp. 1057-1067.
87. Li, J., Kong, B., Gao, X., Liu, Q., Shu, Q. and Chou, K., 2018. Investigation the influences of B2O3 and R2O on the structure and crystallization behaviors of CaO–Al2O3 based F-free mold flux. *Metallurgical Research & Technology*, 115(3), p.304.
88. Li, J., Kong, B., Galdino, B., Xu, J., Chou, K., Liu, Q. and Shu, Q., 2017. Investigation on properties of fluorine-free mold fluxes based on CaO–Al2O3–B2O3 system. *steel research international*, 88(9), p.1600485.
89. Li, Z., Sun, Y., Liu, L., Zhang, Z. Modification of the Structure of Ti-Bearing Mold Flux by the Simultaneous Addition of $B_2O_3$ and $Na_2O$. Metallurgical and Materials Transactions E March 2016, Volume 3, Issue 1, pp 28–36.
90. Marshall, I., Yang, X., Harmuth, H. Fundamental investigations for the design of fluorine free mold powder compositions. Advances in Molten Slags, Fluxes, and Salts: Proceedings of the *10th International Conference on Molten Slags, Fluxes and Salts*, 2016, pp.299-306.
91. Qi J, Liu C, Jiang M. Properties investigation of CaO–Al2O3–SiO2–Li2O–B2O3–Ce2O3 mould flux with different w (CaO)/w (Al2O3) for heat-resistant steel continuous casting[J]. Canadian Metallurgical Quarterly, 2017, 56(2): 212-220.
92. Qi X, Wen G H, Tang P. Investigation on heat transfer performance of fluoride-free and titanium-bearing mold fluxes[J]. Journal of Non-Crystalline Solids, 2008, 354(52-54): 5444-5452.
93. Zhiming Yan, Ramana G. Reddy, Xuewei Lv, Zhengde Pang & Wenchao He (2018) Structure-based viscosity model development for titania aluminosilicate slags, Ironmaking & Steelmaking, DOI: 10.1080/03019233.2018.1510876
94. Shin S H, Yoon D W, Cho J W, et al. Controlling shear thinning property of lime silica based mold flux system with borate additive at 1623 K[J]. Journal of Non-Crystalline Solids, 2015, 425: 83-90.
95. Wang, Z., Shu, Q., Chou, K. Viscosity of fluoride free mold fluxes containing B2O3 and TiO2. Steel research int. 84, 2013(8), pp. 766-776.
96. Wang W, Yan X, Zhou L, et al. Influences of Basicity and Li2O on the Properties of Fluorine-Free Mold Flux for the Casting of Medium Carbon Steels[J]. Metallurgical and Materials Transactions B, 2016, 47(2): 963-973.
97. Q Wang, Y J Lu, S P He, K C Mills & Z S Li (2011) Formation of TiN and Ti(C,N) in TiO2 containing, fluoride free, mould fluxes at high temperature, Ironmaking & Steelmaking, 38:4, pp. 297-301, DOI: 10.1179/1743281210Y.0000000007
98. Wen G, Sridhar S, Tang P, et al. Development of fluoride-free mold powders for peritectic steel slab casting[J]. ISIJ international, 2007, 47(8): 1117-1125.
99. Xin Q, Wen G H, Ping T. Viscosity and viscosity estimate model of fluoride-free and titanium-bearing mold fluxes[J]. Journal of Iron and Steel Research, International, 2010, 17(6): 6-10.

100. Xiong Y U, Wen G H, Ping T, et al. Characteristics of heat flux through slag film of mold slag used for high Al-TRIP steel casting[J]. Journal of Iron and Steel Research, International, 2010, 17(5): 11-16.
101. Yan W, Chen W, Yang Y, et al. Evaluation of B2O3 as replacement for CaF2 in CaO–Al2O3 based mould flux[J]. Ironmaking & Steelmaking, 2016, 43(4): 316-323.
102. Wang, L., Zhang, J., Sasaki, Y., Ostrovski, O., Zhang, C. and Cai, D., 2017. Stability of Fluorine-Free CaO-SiO 2-Al 2 O 3-B 2 O 3-Na 2 O Mold Fluxes. Metallurgical and Materials Transactions B, 48(2), pp.1055-1063.
103. Zhang, Z., Sridhar, S., Cho, J.W. An investigation of the evaporation of B2O3 and Na2O in F-free mold slags. ISIJ International, 2011(51), No.1, pp. 80-87.
104. Zhang, Z., Li, J., Liu, P. Crystallization behaviour in Fluoride-free mold fluxes containing TiO2/ZrO2. *Journal of Iron and Steel Research, International*. 2011, 18(5), pp. 31-37.
105. Zhang L, Wang W, Xie S, et al. Effect of basicity and B2O3 on the viscosity and structure of fluorine-free mold flux[J]. Journal of Non-Crystalline Solids, 2017, 460: 113-118.
106. Zhou L, Wang W, Wei J, et al. Melting and heat transfer behavior of fluorine-free mold fluxes for casting medium carbon steels[J]. ISIJ International, 2015, 55(4): 821-829.
107. Klug J L, Pereira M, Nohara E L, et al. F-free mould powders for low carbon steel slab casting–technological parameters and industrial trials[J]. Ironmaking & Steelmaking, 2016, 43(8): 559-563.
108. Li, G.R., Wang, H.M., Dai, Q.X., Zhao, Y.T. and Li, J.S., 2007. Physical Properties and Regulating Mechanism of Fluoride-Free and Harmless B 2 O 3-Containing Mould Flux. Journal of Iron and Steel Research International, 14(1), pp.25-28.
109. Wang, Z., Shu, Q. and Chou, K., 2013. Study on structure characteristics of B2O3 and TiO2-bearing F-free mold flux by Raman spectroscopy. High Temperature Materials and Processes, 32(3), pp.265-273.
110. Zhang, Z.T., Wen, G.H. and Zhang, Y.Y., 2011. Crystallization behavior of F-free mold fluxes. International Journal of Minerals, Metallurgy, and Materials, 18(2), pp.150-158.
111. Wang, L., Cui, Y., Yang, J., Zhang, C., Cai, D., Zhang, J., Sasaki, Y. and Ostrovski, O., 2015. Melting Properties and Viscosity of SiO2 ‐ CaO ‐ Al2O3 ‐ B2O3 System. steel research international, 86(6), pp.670-677.
112. Li, J., Kong, B., Galdino, B., Xu, J., Chou, K., Liu, Q. and Shu, Q., 2017. Investigation on properties of fluorine ‐ free mold fluxes based on CaO ‐ Al2O3 ‐ B2O3 system. steel research international, 88(9), p.1600485.
113. Wang, Z., Shu, Q. and Chou, K., 2015. Crystallization Kinetics of CaO-SiO2 (CaO/SiO2= 1)-TiO2-10 mass% B2O3 Glassy Slag by Differential Thermal Analysis. ISIJ International, 55(4), pp.709-716.
114. Shu, Q., Wang, Z., Klug, J.L., Chou, K. and Scheller, P.R., 2013. Effects of B2 O 3 and Ti O 2 on Crystallization Behavior of Slags in Al2 O 3–C a O–M g O–N a2 O–S i O 2 System. steel research international, 84(11), pp.1138-1145.
115. Gao, Y., Bian, L. and Liang, Z., 2015. Influence of B2O3 and TiO2 on viscosity of titanium ‐ bearing blast furnace slag. steel research international, 86(4), pp.386-390.
116. AB, F., Gisby, J., RC, A., PD, L. and Sridhar, S., 2004. Dissolution of ZrO2, Al2O3, MgO and MgAl2O4 particles in a B2O3 containing commercial fluoride-free mould slag. ISIJ international, 44(5), pp.836-845.

117. Esfahani S, Barati M. Effect of slag composition on the crystallization of synthetic CaO–SiO2–Al2O3–MgO slags: Part I—Crystallization behavior[J]. Journal of Non-Crystalline Solids, 2016, 436: 35-43.
118. Esfahani, S., Mostaghel, S. and Barati, M., 2016. Effect of slag composition on the crystallization of synthetic CaO-SiO2-Al2O3-MgO slags: Part II-Measurement and prediction of critical cooling rate. Journal of Non-Crystalline Solids, 436, pp.29-34.
119. Kim M S, Kang Y B. Development of a multicomponent reaction rate model coupling thermodynamics and kinetics for reaction between high Mn-high Al steel and CaO-SiO 2-type molten mold flux[J]. Calphad, 2018, 61: 105-115.
120. Klug J L, Freitas S L, Pereira M, et al. Fluorinefree mould powders for billet casting–technological parameters[C]//41st Steelmaking Seminar–International. 2010: 415-424.
121. Klug J L, Silva D R, Freitas S L, et al. Fluorine-Free Mould Powders for Billet Casting–Technological Parameters and Industrial Tests[J]. Steel research international, 2012, 83(8): 791-799.
122. Qi J, Liu C, Jiang M. Role of Li2O on the structure and viscosity in CaO-Al2O3-Li2O-Ce2O3 melts[J]. Journal of Non-Crystalline Solids, 2017, 475: 101-107.
123. Takahira, N., Hanao, M. and Tsukaguchi, Y., 2013. Viscosity and solidification temperature of SiO2–CaO–Na2O melts for fluorine free mould flux. ISIJ international, 53(5), pp.818-822.
124. Xu, J., Zhang, J., Jie, C., Tang, L., Chou, K. Measuring and modeling of density for selected CMAS slag with low silica. *Journal of Iron and Steel Research, International*. 2012, 19(7), pp. 26-32.
125. Zhang S, Zhang X, Liu W, et al. Relationship between structure and viscosity of CaO–SiO2–Al2O3–MgO–TiO2 slag[J]. Journal of Non-Crystalline Solids, 2014, 402: 214-222.
126. Zhao S, He S P, Guo Y T, et al. Effect on cleanliness of molten steel with different slag systems for low alloy ship plate[J]. Ironmaking & Steelmaking, 2016, 43(10): 790-798.
127. Harmuth, H. Montanuniversitaet of Leoben, Non basic refractory lecture 2015.
128. Zhanmin, C., Xiaoyan, S. and Zhiyu, Q., 2008. Thermodynamic Modeling Software FactSage and Its Application [J]. Chinese Journal of Rare Metals, 2, pp.216-219.
129. Shi, J., Sun, L., Qiu, J., Zhang, B. and Jiang, M., 2017. Phase equilibria of CaO-SiO2-5wt% MgO-10wt% Al2O3-TiO2 system at 1300° C and 1400° C relevant to Ti-bearing furnace slag. Journal of Alloys and Compounds, 699, pp.193-199.
130. Longbottom, R.J., Monaghan, B.J. and Mathieson, J.G., 2013. Development of a bonding phase within titanomagnetite-coal compacts. ISIJ international, 53(7), pp.1152-1160.
131. Zhang, Z., Xiao, Y., Voncken, J., Yang, Y., Boom, R., Wang, N., Zou, Z. Thermodynamic assessment of the CaO-Na2O-SiO2 slag system. Department of Materials Science and Engineering, Delft University of Technology, 2628 CD, Delft, the Netherlands.
132. Pelton, A.D. and Wu, P., 1999. Thermodynamic modeling in glass-forming melts. Journal of Non-Crystalline Solids, 253(1-3), pp.178-191.
133. Arroyabe, E., Tessadri, R., Többens, D.M. and Kahlenberg, V., 2011. Does K2CaSiO4 Exist? A Phase-Analytical Study in the System K2O–CaO–SiO2 with Implications for the Characterization of Residual Materials. Journal of the American Ceramic Society, 94(8), pp.2652-2655.

134. the complete book on glass and ceramics technology (2nd revised edition), by the NIIR Board of Consultants and Engineers. 2012
135. Bansal, N.P. and Doremus, R.H., 2013. Handbook of glass properties. Elsevier.
136. Ohgaki, T., Higashida, A., Soga, K. and Yasumori, A., 2007. Eu-Doped CaAl2Si2O8 Nanocrystalline Phosphors Crystallized from the CaO–Al2O3–SiO2 Glass System. Journal of The Electrochemical Society, 154(5), pp.J163-J166.
137. Neuville, D.R., Cormier, L., Montouillout, V. and Massiot, D., 2007. Local Al site distribution in aluminosilicate glasses by 27Al MQMAS NMR. Journal of Non-Crystalline Solids, 353(2), pp.180-184.
138. Jiang, Z.H. and Zhang, Q.Y., 2014. The structure of glass: A phase equilibrium diagram approach. Progress in Materials Science, 61, pp.144-215.
139. Hrma, P., 2006. High-temperature viscosity of commercial glasses. Ceramics Silikaty, 50(2), p.57.
140. Swamy, V., Jung, I.H. and Decterov, S.A., 2009. Thermodynamic modeling of the Al2O3–B2O3–SiO2 system. Journal of Non-Crystalline Solids, 355(34-36), pp.1679-1686.
141. Harmuth, H. Montanuniversitaet of Leoben, Non basic refractory lecture 2015.
142. Rodriguez, C.P., McCloy, J.S., Schweiger, M.J., Crum, J.V. and Winschell, A.E., 2011. Optical basicity and nepheline crystallization in high alumina glasses (No. PNNL-20184; EMSP-RPT-003). Pacific Northwest National Lab.(PNNL), Richland, WA (United States).
143. Li, H., Hrma, P., Vienna, J.D., Qian, M., Su, Y. and Smith, D.E., 2003. Effects of Al2O3, B2O3, Na2O, and SiO2 on nepheline formation in borosilicate glasses: chemical and physical correlations. Journal of Non-Crystalline Solids, 331(1-3), pp.202-216.
144. Varshneya, A.K., 2013. Fundamentals of inorganic glasses. Elsevier.

## Appendix A. Selected FactSage Calculations

Table A1. Chemical compositions used to construct Figure 15 in section III.iii.1

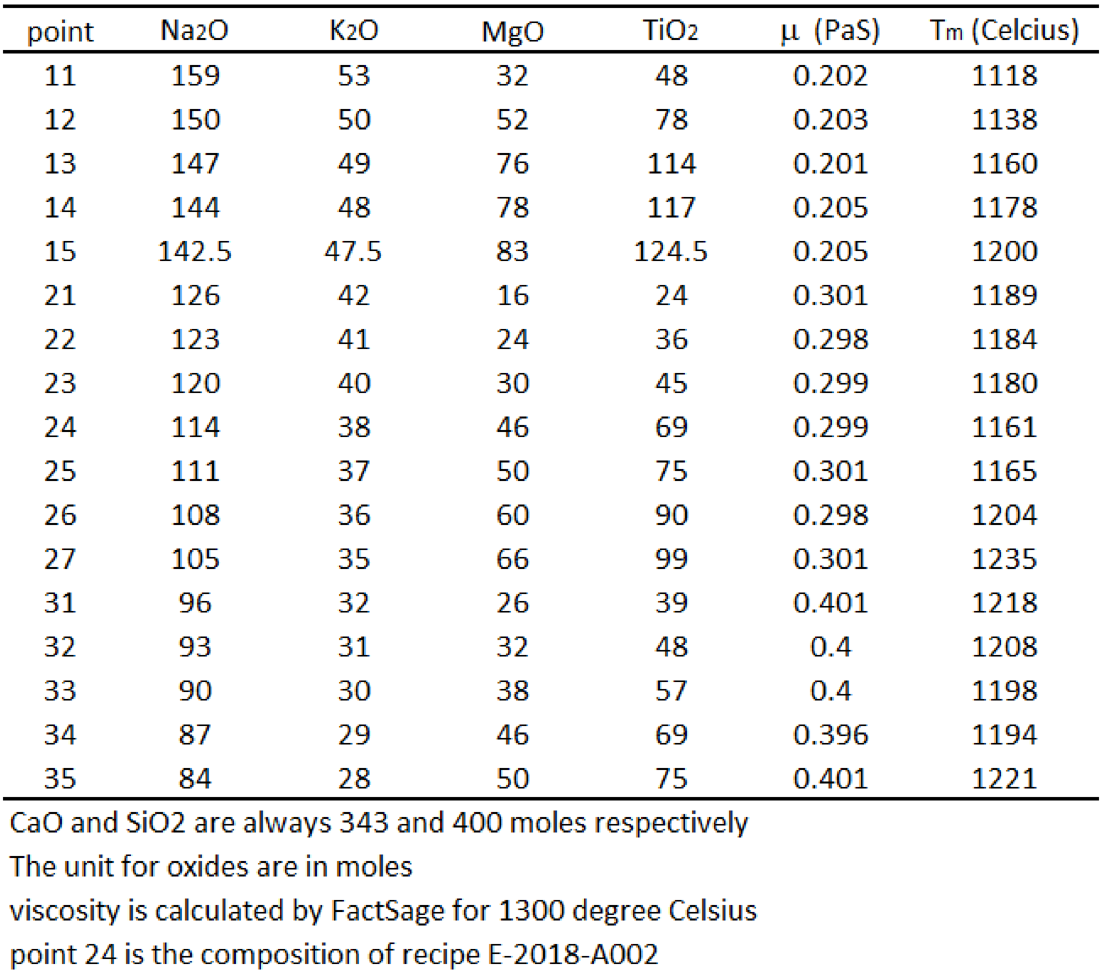

| point | $Na_2O$ | $K_2O$ | MgO | $TiO_2$ | $\mu$ (PaS) | $T_m$ (Celcius) |
|---|---|---|---|---|---|---|
| 11 | 159 | 53 | 32 | 48 | 0.202 | 1118 |
| 12 | 150 | 50 | 52 | 78 | 0.203 | 1138 |
| 13 | 147 | 49 | 76 | 114 | 0.201 | 1160 |
| 14 | 144 | 48 | 78 | 117 | 0.205 | 1178 |
| 15 | 142.5 | 47.5 | 83 | 124.5 | 0.205 | 1200 |
| 21 | 126 | 42 | 16 | 24 | 0.301 | 1189 |
| 22 | 123 | 41 | 24 | 36 | 0.298 | 1184 |
| 23 | 120 | 40 | 30 | 45 | 0.299 | 1180 |
| 24 | 114 | 38 | 46 | 69 | 0.299 | 1161 |
| 25 | 111 | 37 | 50 | 75 | 0.301 | 1165 |
| 26 | 108 | 36 | 60 | 90 | 0.298 | 1204 |
| 27 | 105 | 35 | 66 | 99 | 0.301 | 1235 |
| 31 | 96 | 32 | 26 | 39 | 0.401 | 1218 |
| 32 | 93 | 31 | 32 | 48 | 0.4 | 1208 |
| 33 | 90 | 30 | 38 | 57 | 0.4 | 1198 |
| 34 | 87 | 29 | 46 | 69 | 0.396 | 1194 |
| 35 | 84 | 28 | 50 | 75 | 0.401 | 1221 |

CaO and SiO2 are always 343 and 400 moles respectively

The unit for oxides are in moles

viscosity is calculated by FactSage for 1300 degree Celsius

point 24 is the composition of recipe E-2018-A002

# Appendix B. Slag Molar Compositions

Table B1. Slag molar compositions corresponding to Table 9 in section IV.i.1

| slag serial [moles] | $SiO_2$ | CaO | $Na_2O$ | $K_2O$ | MgO | $TiO_2$ | $Al_2O_3$ | Σ |
|---|---|---|---|---|---|---|---|---|
| E-2018-A002 | 400 | 343 | 114 | 38 | 46 | 69 | 0 | 1010 |
| E-2018-A003 | 400 | 343 | 165 | 54 | 61.6 | 92.4 | 30 | 1146 |
| E-2018-A004 | 400 | 343 | 207 | 69 | 88 | 132 | 60 | 1299 |
| E-2018-A005 | 400 | 343 | 230 | 75 | 102 | 145 | 75 | 1370 |
| E-2018-A008 | 400 | 368 | 152.4 | 50.8 | 68.4 | 102.6 | 30 | 1172.2 |
| E-2018-A009 | 400 | 394 | 146.4 | 48.8 | 66.2 | 99.3 | 30 | 1184.7 |
| E-2018-A010 | 400 | 325 | 163.4 | 54.4 | 72.9 | 109.4 | 30 | 1155.1 |
| E-2018-A015 | 400 | 307 | 216 | 72 | 92.2 | 138.3 | 60 | 1285.5 |
| E-2018-A016 | 400 | 301 | 232.8 | 77.6 | 101 | 147 | 75 | 1334.4 |

Table B2. Slag molar compositions corresponding to Table 10 in section IV.i.1

| slag serial [moles] | $SiO_2$ | CaO | $Na_2O$ | $K_2O$ | MgO | $TiO_2$ | FeO | MnO | $Al_2O_3$ | Σ |
|---|---|---|---|---|---|---|---|---|---|---|
| E-2018-A017 | 400 | 325 | 159.9 | 53.3 | 72.4 | 108.6 | 4 | 4 | 30 | 1157.2 |
| E-2018-A018 | 400 | 325 | 156.6 | 52.2 | 71.8 | 107.7 | 8 | 8 | 30 | 1159.3 |
| E-2018-A019 | 400 | 343 | 107.1 | 35.7 | 53 | 79.5 | 3.5 | 3.5 | 0 | 1025.3 |
| E-2018-A020 | 400 | 343 | 104.3 | 34.7 | 53 | 79.5 | 7 | 7 | 0 | 1028.5 |
| E-2018-A021 | 400 | 307 | 212.1 | 70.7 | 91.4 | 137.1 | 4.5 | 4.5 | 60 | 1287.3 |
| E-2018-A022 | 400 | 307 | 208.2 | 69.4 | 90.4 | 135.6 | 9 | 9 | 60 | 1288.6 |

Table B3. Slag molar compositions corresponding to Table 11 in section IV.i.1

| slag serial [moles] | $SiO_2$ | CaO | $Na_2O$ | $K_2O$ | MgO | $TiO_2$ | $Al_2O_3$ | $B_2O_3$ | Σ |
|---|---|---|---|---|---|---|---|---|---|
| E-2018-A033 | 400 | 307 | 172.2 | 57.4 | 70.2 | 105.3 | 30 | 30 | 1172.1 |
| E-2018-A034 | 400 | 325 | 167.6 | 55.8 | 68.4 | 102.6 | 30 | 30 | 1179.4 |
| E-2018-A035 | 400 | 351 | 161 | 53.6 | 66 | 99 | 30 | 30 | 1190.6 |
| E-2018-A036 | 400 | 371 | 156 | 52 | 64 | 96 | 30 | 30 | 1199 |
| E-2018-A039 | 400 | 325 | 120.3 | 40.1 | 48.4 | 72.6 | 0 | 30 | 1036.4 |
| E-2018-A040 | 400 | 307 | 127.8 | 42.6 | 45 | 67.5 | 0 | 60 | 1049.9 |

Table B4. Slag molar compositions corresponding to Table 15 in section IV.ii.1

| slag serial [moles] | $SiO_2$ | CaO | $Na_2O$ | MgO | $TiO_2$ | $Al_2O_3$ | $B_2O_3$ | Σ |
|---|---|---|---|---|---|---|---|---|
| E-2018-A0123 | 0 | 175 | 0 | 225 | 0 | 100 | 500 | 1000 |
| E-2018-A0124 | 0 | 183 | 23 | 217 | 34.5 | 100 | 500 | 1057.5 |
| E-2018-A0125 | 0 | 180 | 49 | 220 | 73.5 | 125 | 475 | 1122.5 |
| E-2018-A0126 | 0 | 161.5 | 78 | 238.5 | 117 | 150 | 450 | 1195 |
| E-2018-A0130 | 100 | 188 | 30 | 212 | 45 | 100 | 400 | 1075 |
| E-2018-A0131 | 150 | 189 | 24 | 211 | 36 | 100 | 350 | 1060 |
| E-2018-A0132 | 200 | 187 | 32 | 213 | 48 | 100 | 300 | 1080 |
| E-2018-A0137 | 230 | 189 | 0 | 211 | 0 | 100 | 270 | 1000 |
| E-2018-A0138 | 270 | 188 | 0 | 212 | 0 | 100 | 230 | 1000 |

Table B5. Slag molar compositions corresponding to Table 15 in section VI

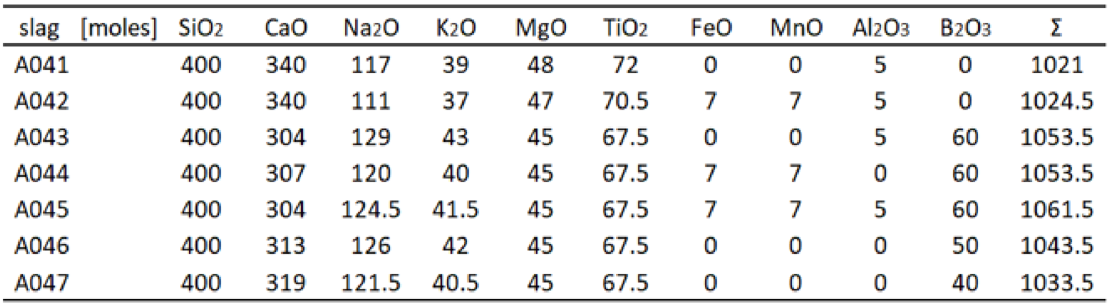

| slag [moles] | $SiO_2$ | CaO | $Na_2O$ | $K_2O$ | MgO | $TiO_2$ | FeO | MnO | $Al_2O_3$ | $B_2O_3$ | Σ |
|---|---|---|---|---|---|---|---|---|---|---|---|
| A041 | 400 | 340 | 117 | 39 | 48 | 72 | 0 | 0 | 5 | 0 | 1021 |
| A042 | 400 | 340 | 111 | 37 | 47 | 70.5 | 7 | 7 | 5 | 0 | 1024.5 |
| A043 | 400 | 304 | 129 | 43 | 45 | 67.5 | 0 | 0 | 5 | 60 | 1053.5 |
| A044 | 400 | 307 | 120 | 40 | 45 | 67.5 | 7 | 7 | 0 | 60 | 1053.5 |
| A045 | 400 | 304 | 124.5 | 41.5 | 45 | 67.5 | 7 | 7 | 5 | 60 | 1061.5 |
| A046 | 400 | 313 | 126 | 42 | 45 | 67.5 | 0 | 0 | 0 | 50 | 1043.5 |
| A047 | 400 | 319 | 121.5 | 40.5 | 45 | 67.5 | 0 | 0 | 0 | 40 | 1033.5 |

# Appendix C. DTA Results

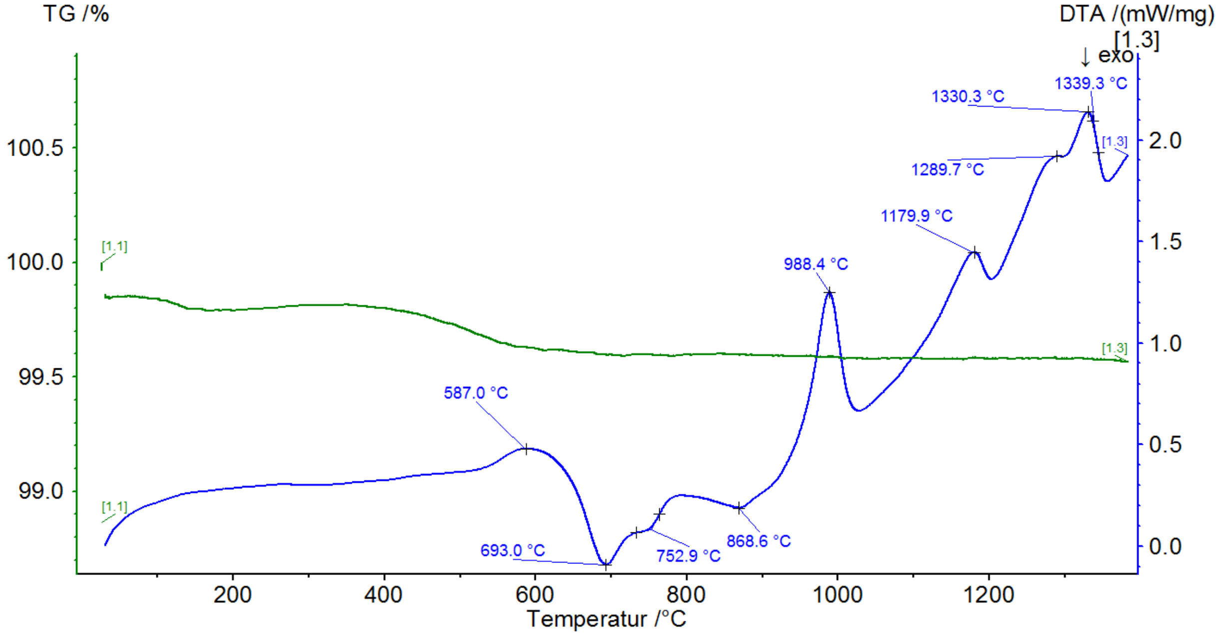

Figure C1. DTA heating curve for slag E-2018-A010

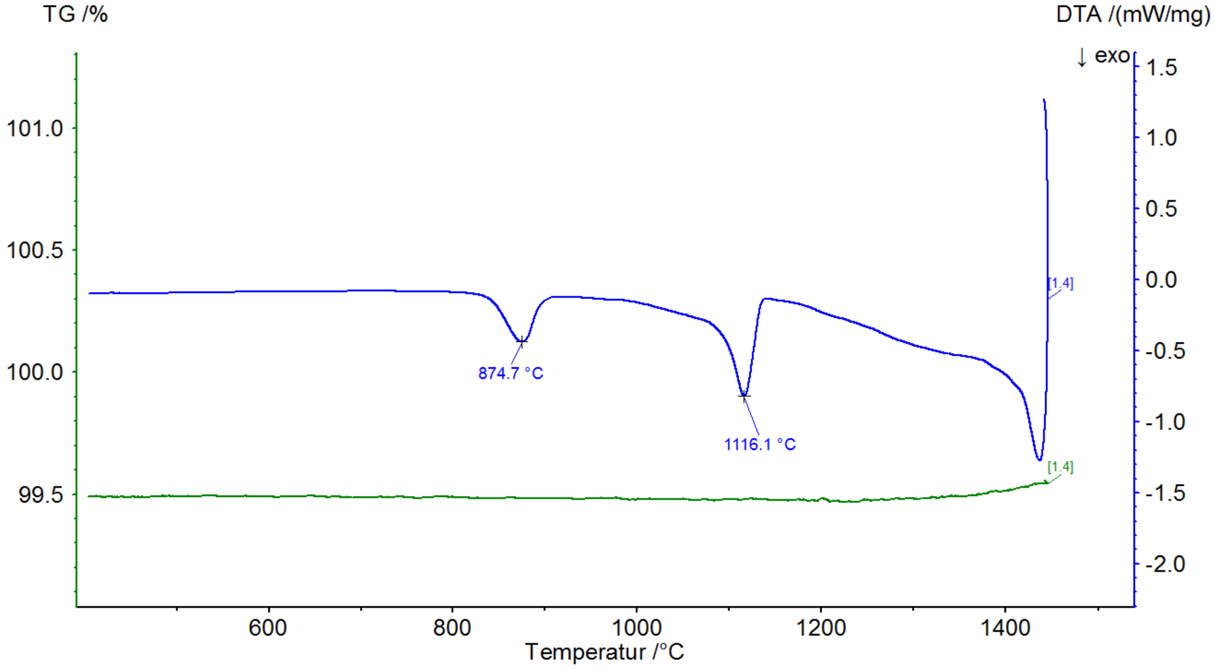

Figure C2. DTA cooling curve for slag E-2018-A010

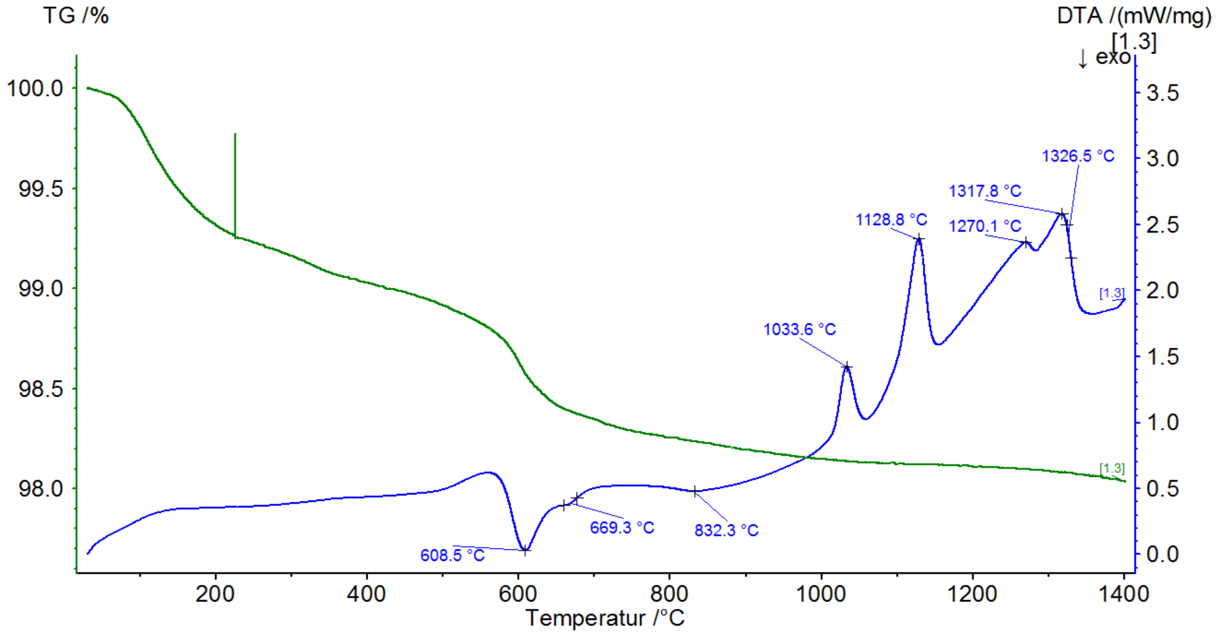

Figure C3. DTA heating curve for slag E-2018-A015

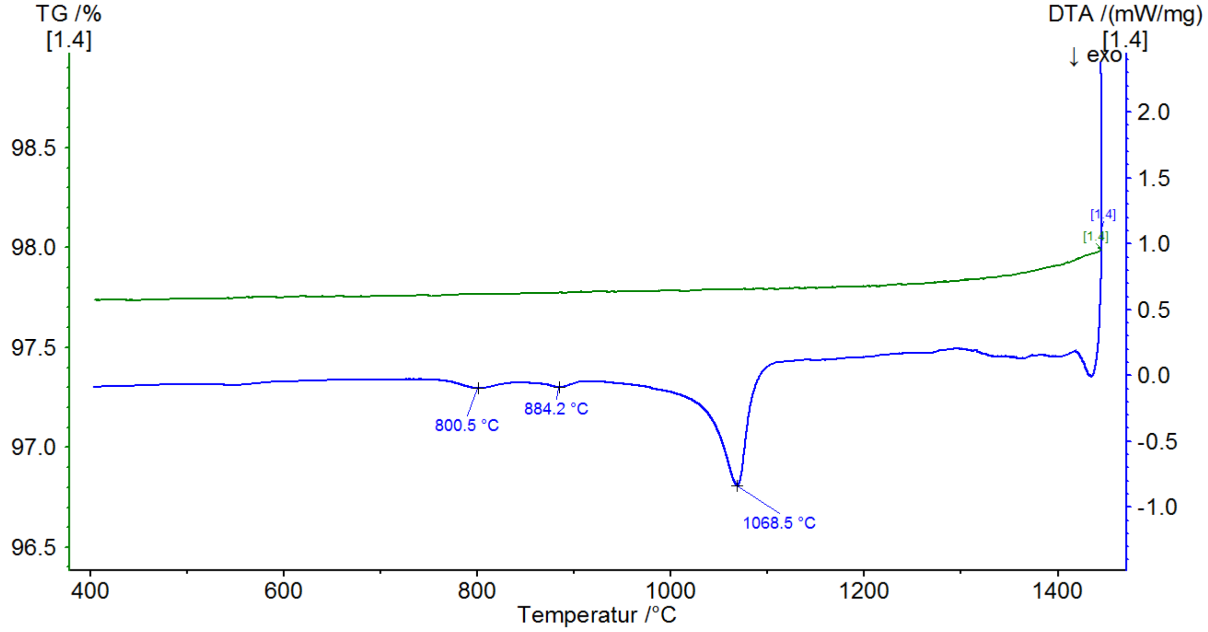

Figure C4. DTA cooling curve for slag E-2018-A015

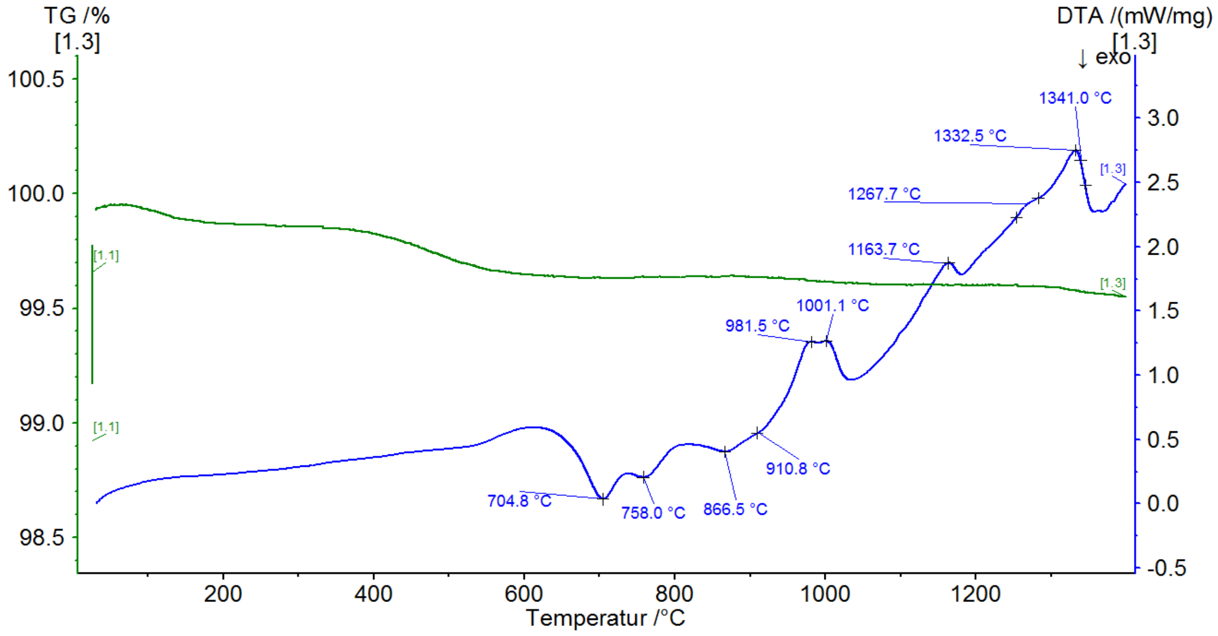

Figure C5. DTA heating curve for slag E-2018-A018

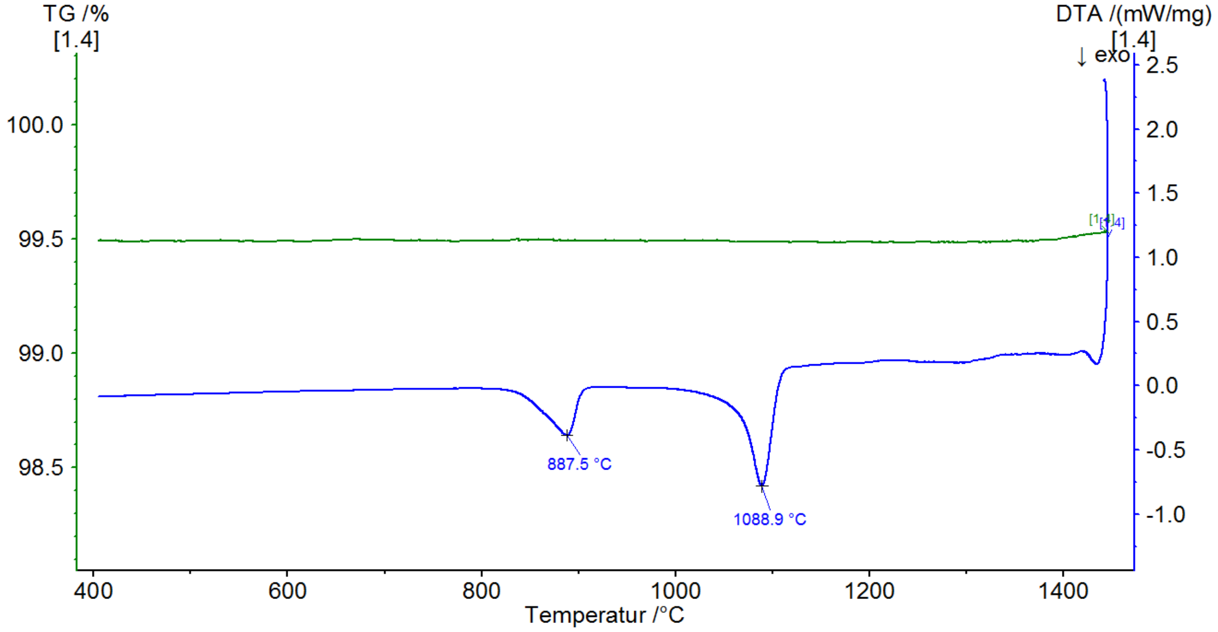

Figure C6. DTA cooling curve for slag E-2018-A018

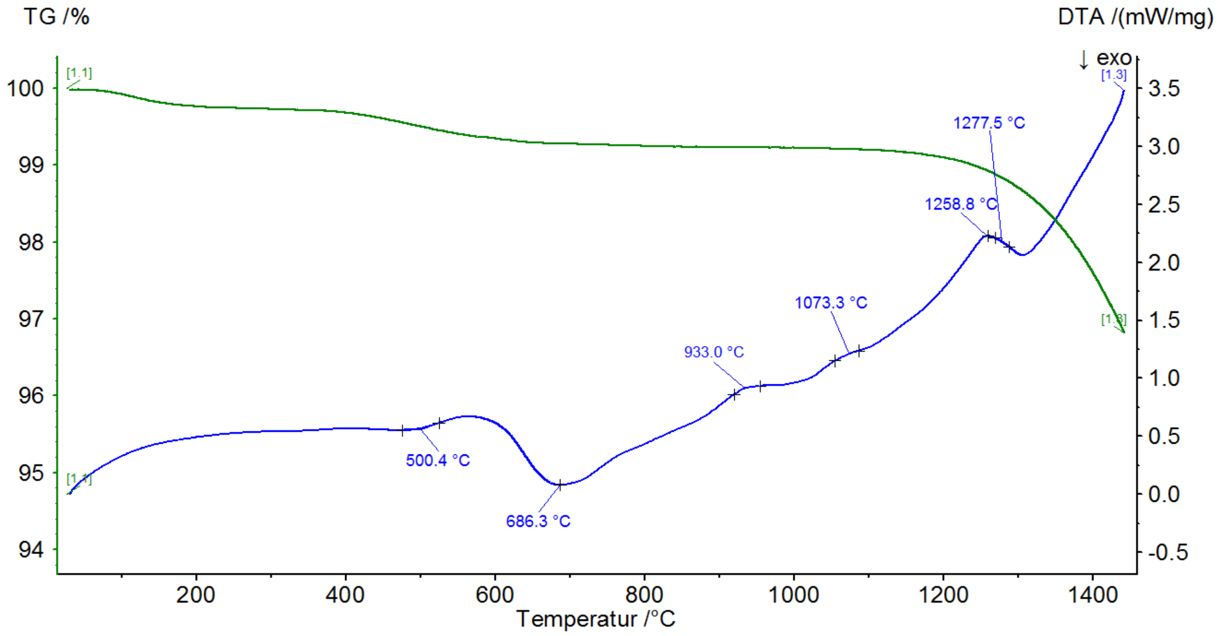

Figure C7. DTA heating curve for slag E-2018-A033

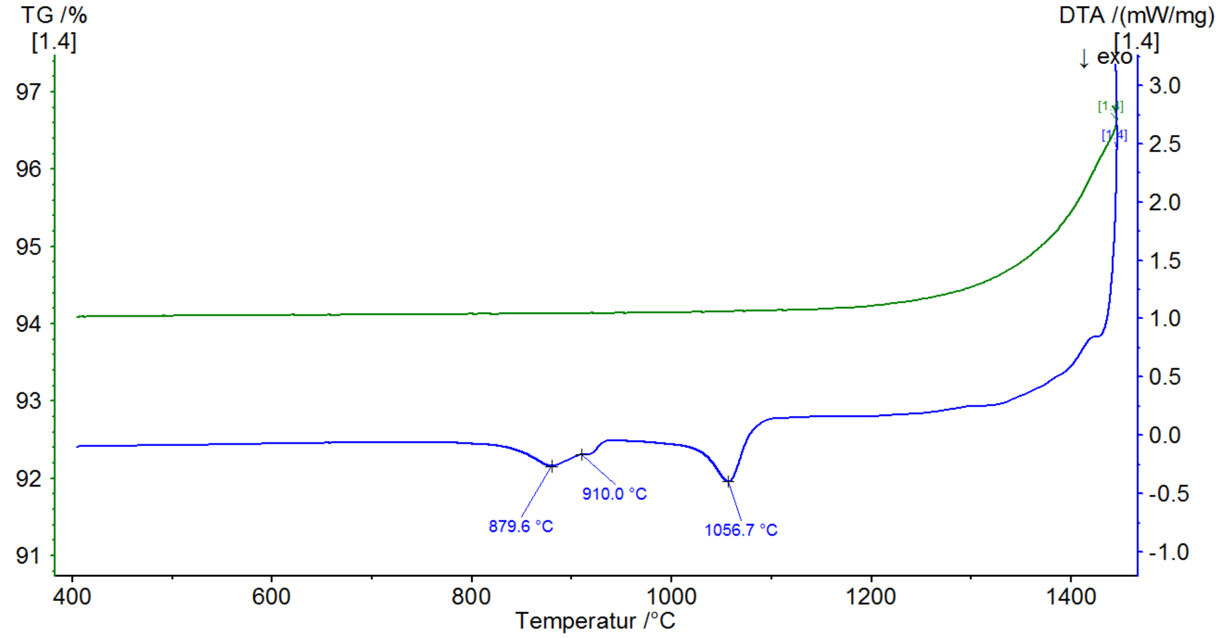

Figure C8. DTA cooling curve for slag E-2018-A033

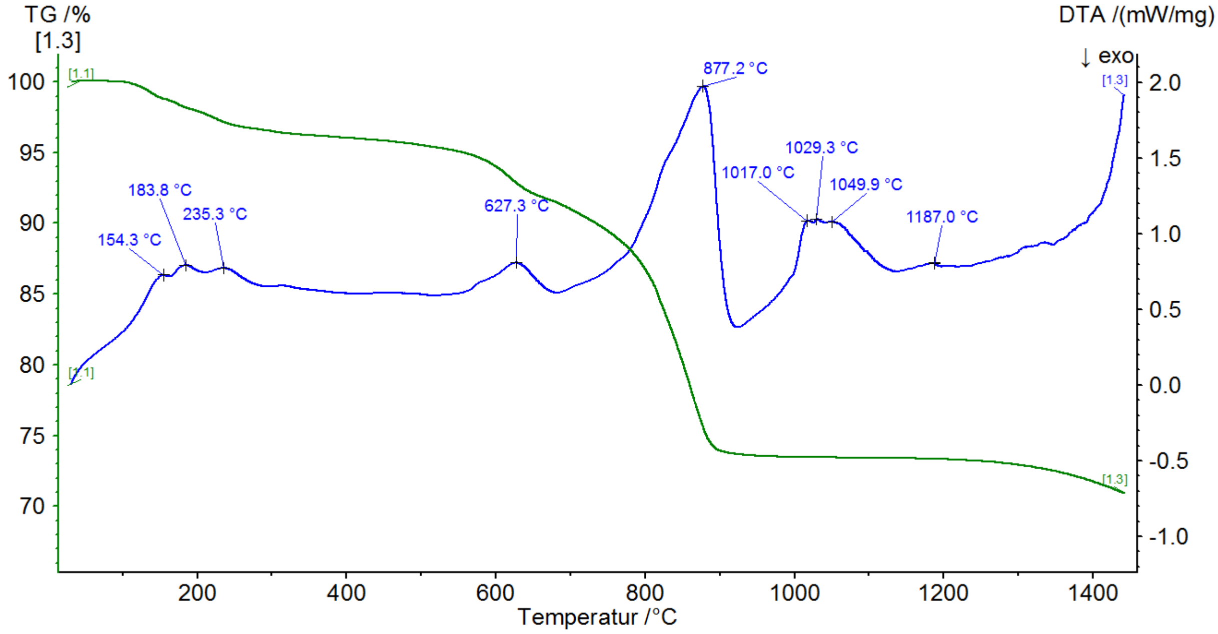

Figure C9. DTA heating curve for slag E-2018-A040

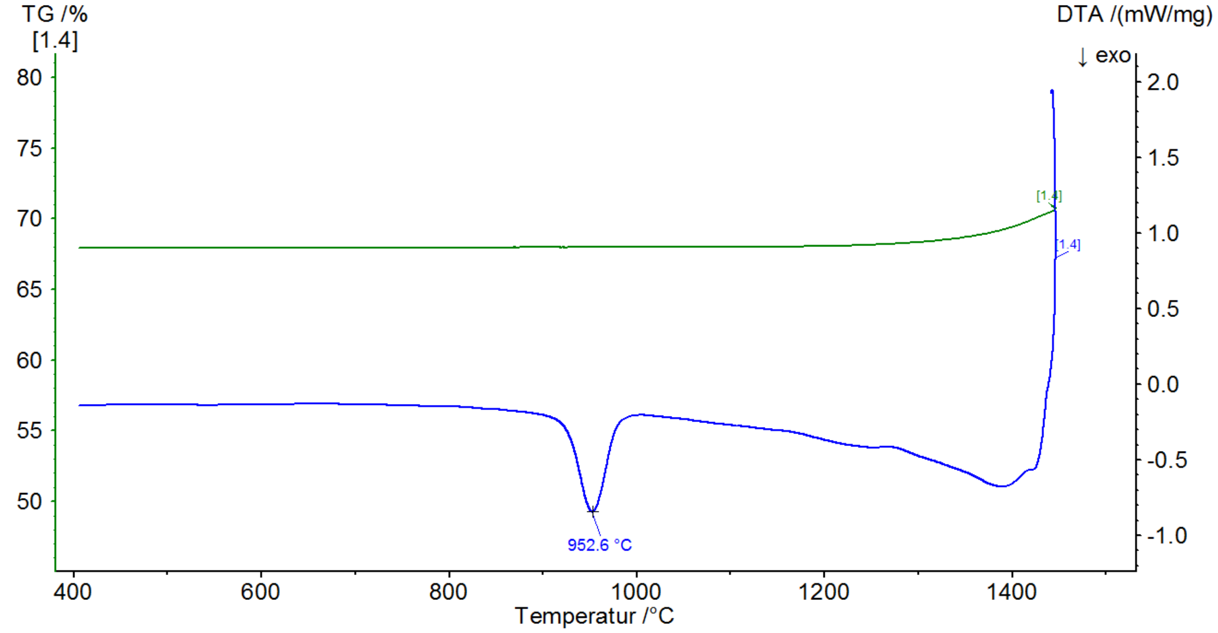

Figure C10. DTA cooling curve for slag E-2018-A040

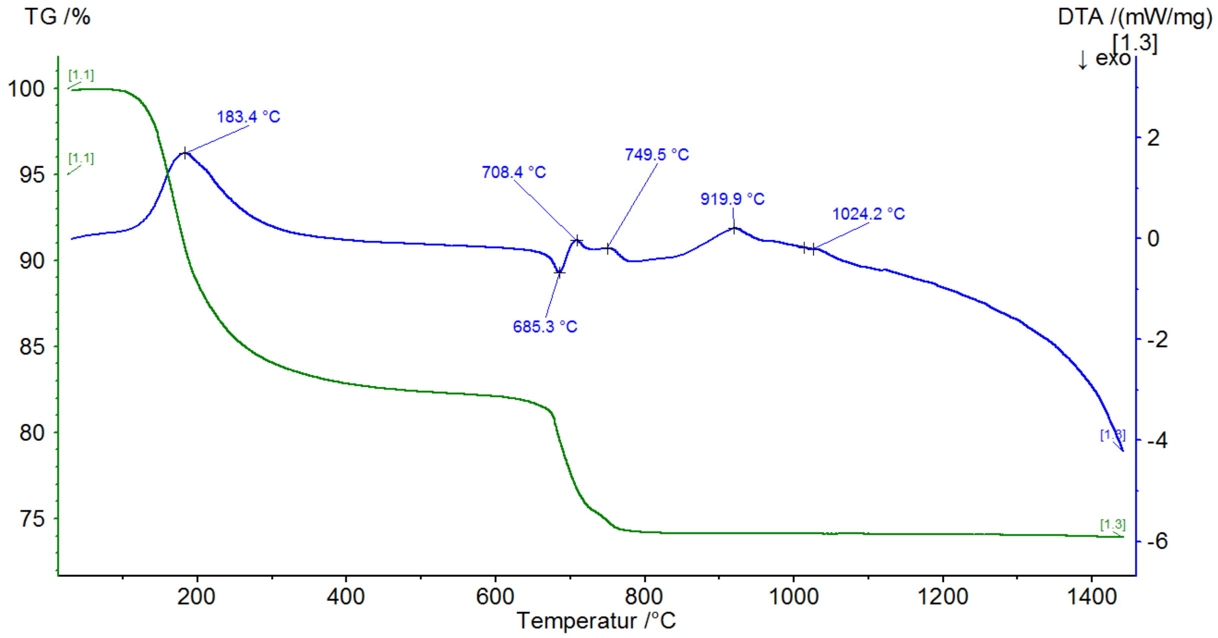

Figure C11. DTA heating curve for slag E-2018-A124

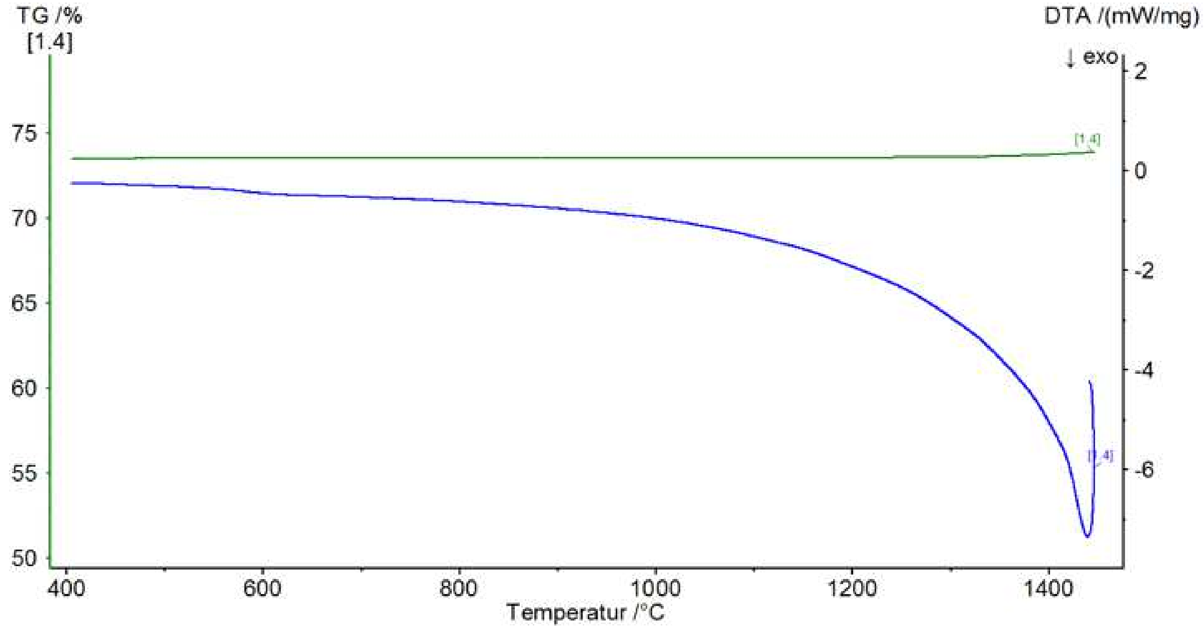

Figure C12. DTA cooling curve for slag E-2018-A124

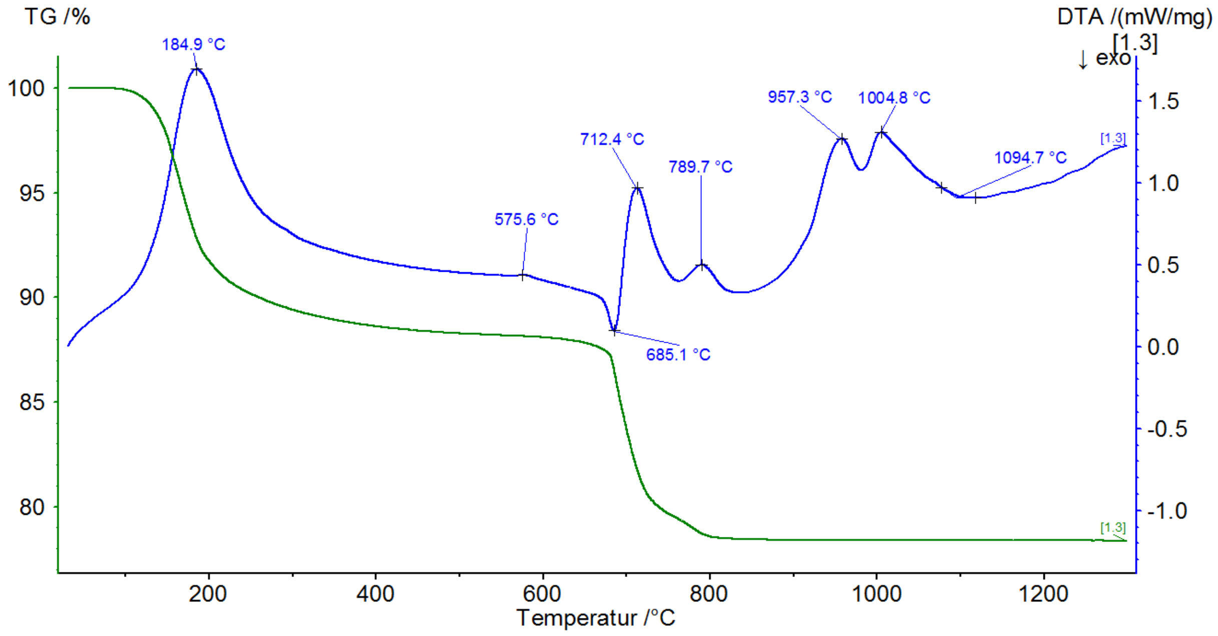

Figure C13. DTA heating curve for slag E-2018-A138

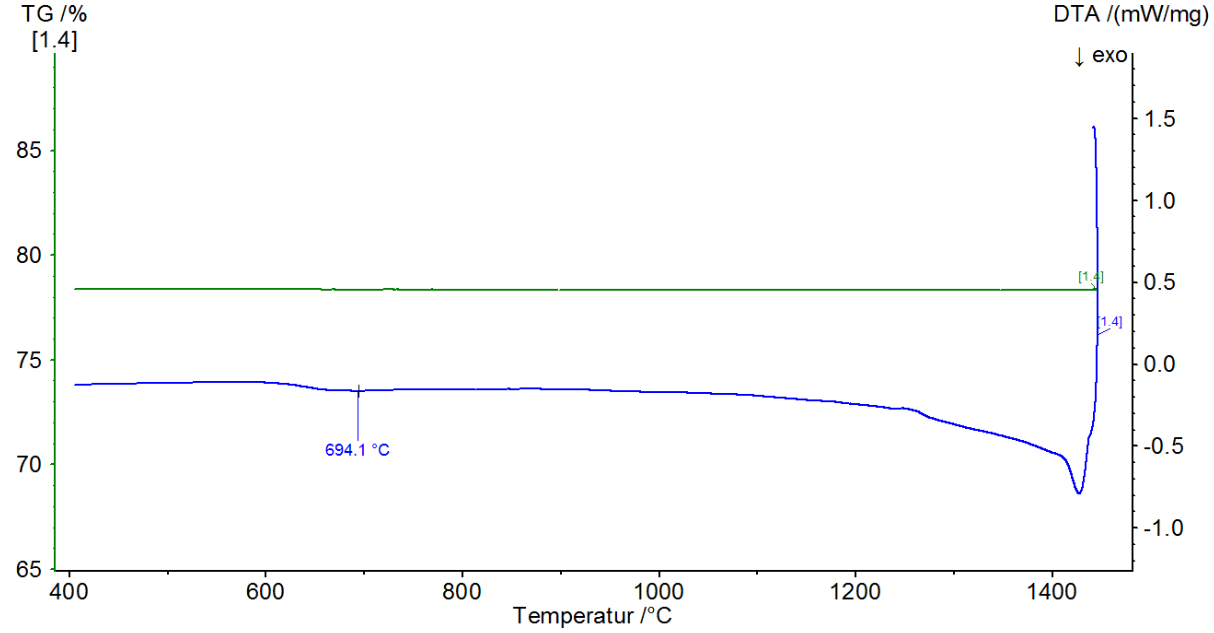

Figure C14. DTA cooling curve for slag E-2018-A138

## Appendix D. FCT graphs

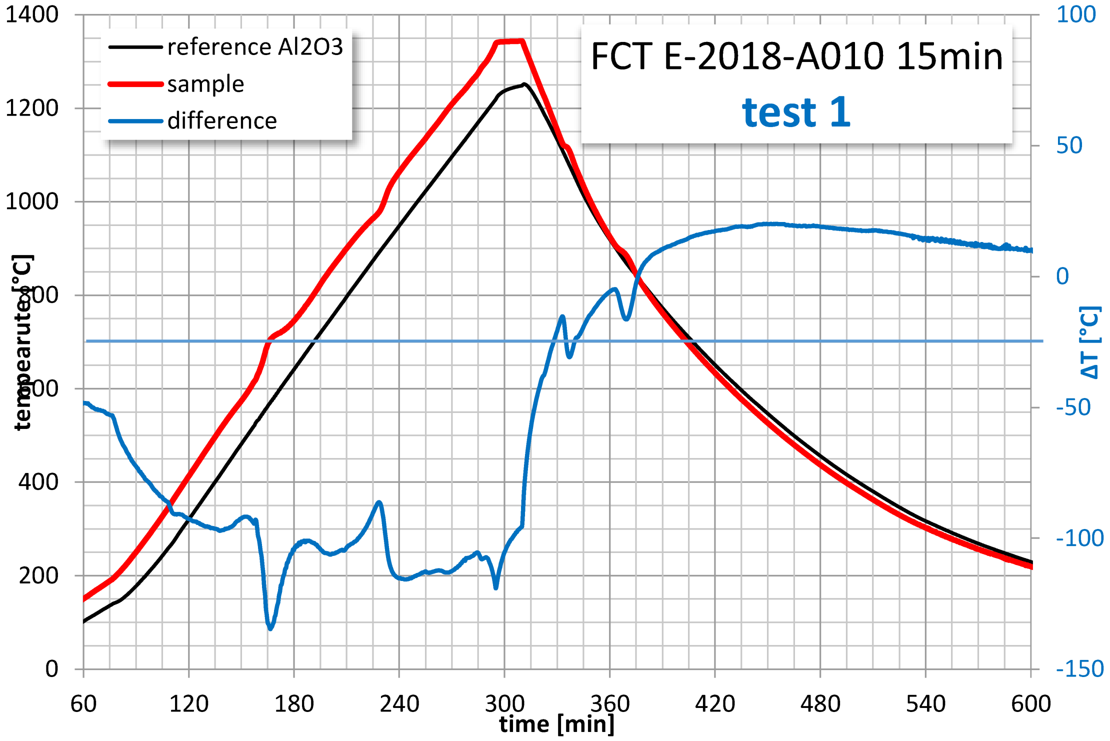

Figure D1. FCT result of E-2018-A010

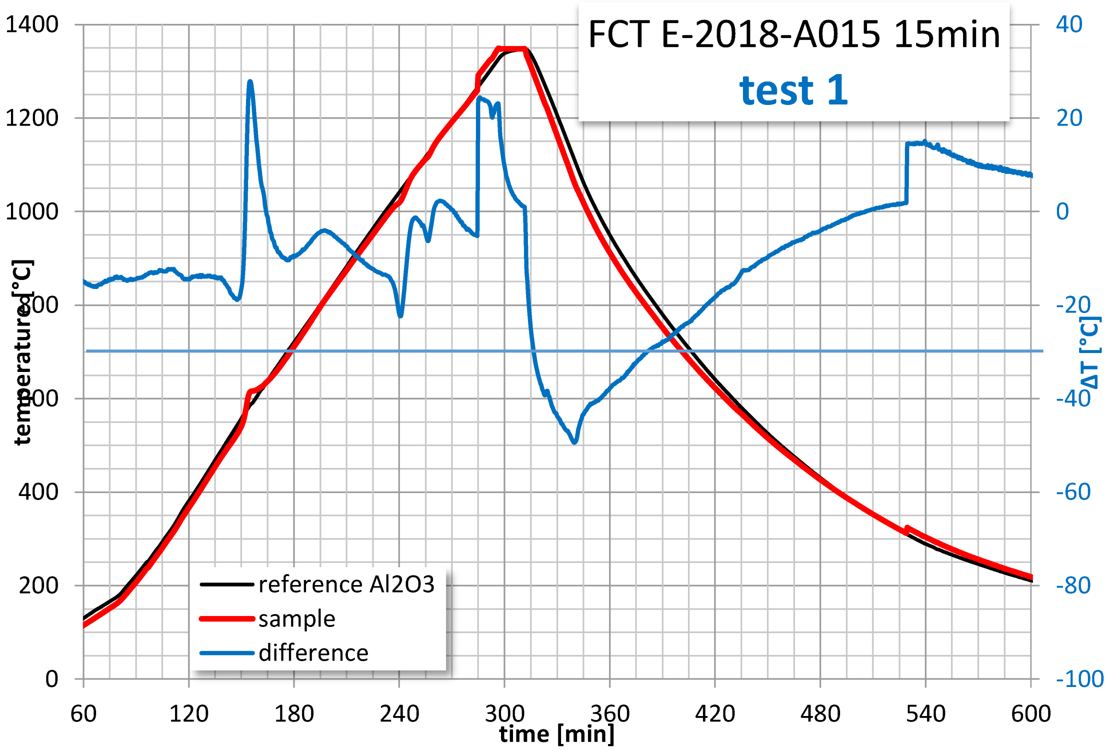

Figure D2. FCT result of E-2018-A015

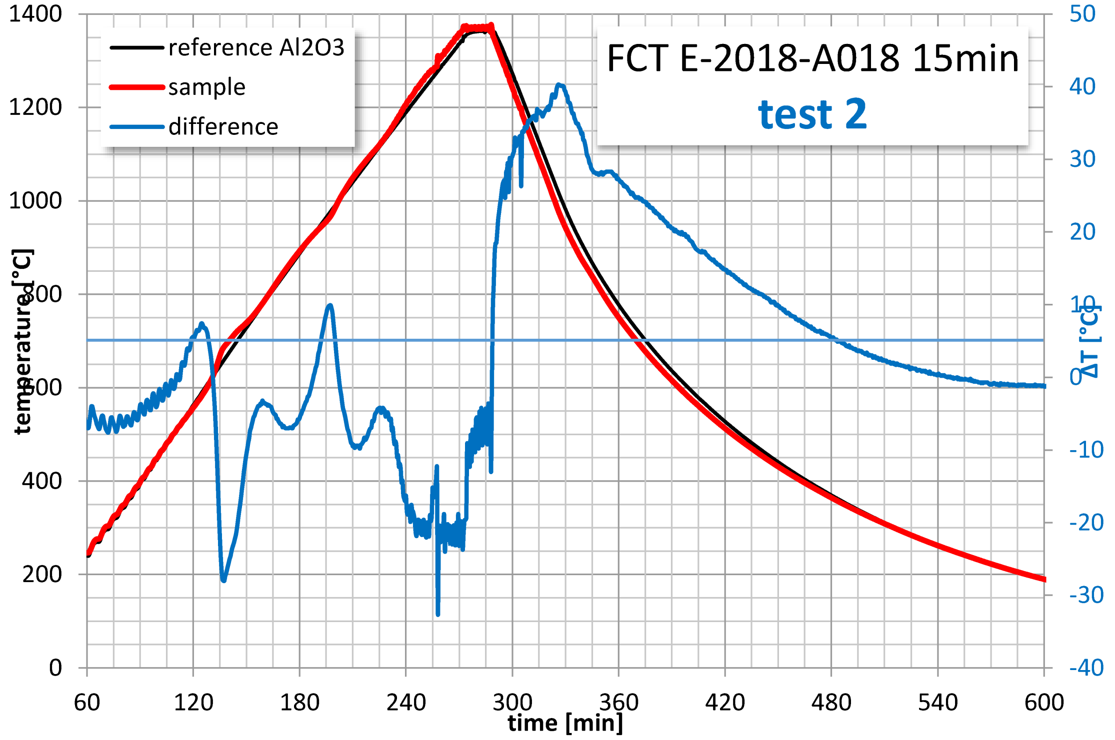

Figure D3. FCT result of E-2018-A018

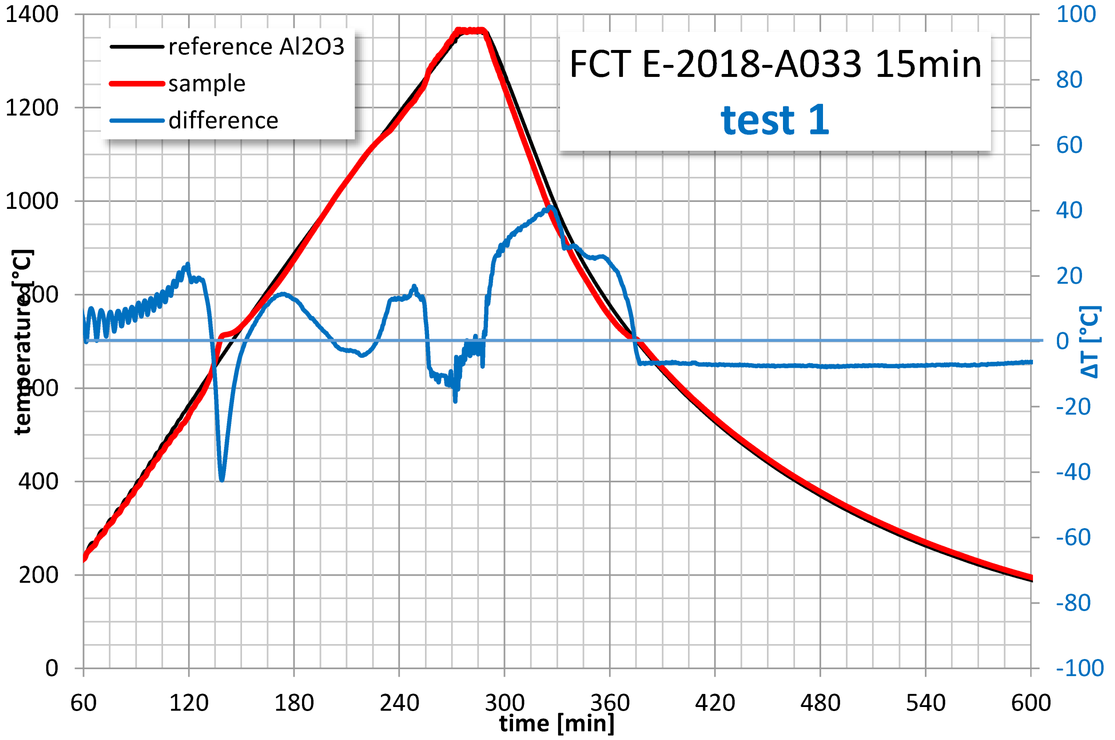

Figure D4. FCT result of E-2018-A033

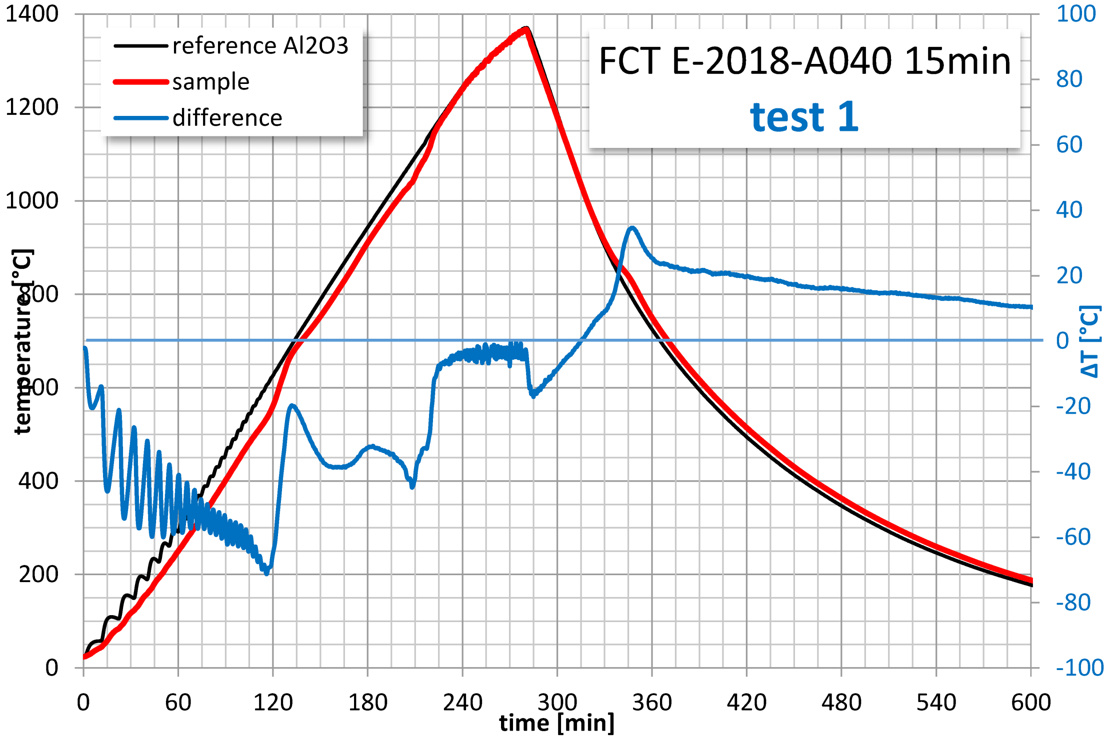

Figure D5. FCT result of E-2018-A040

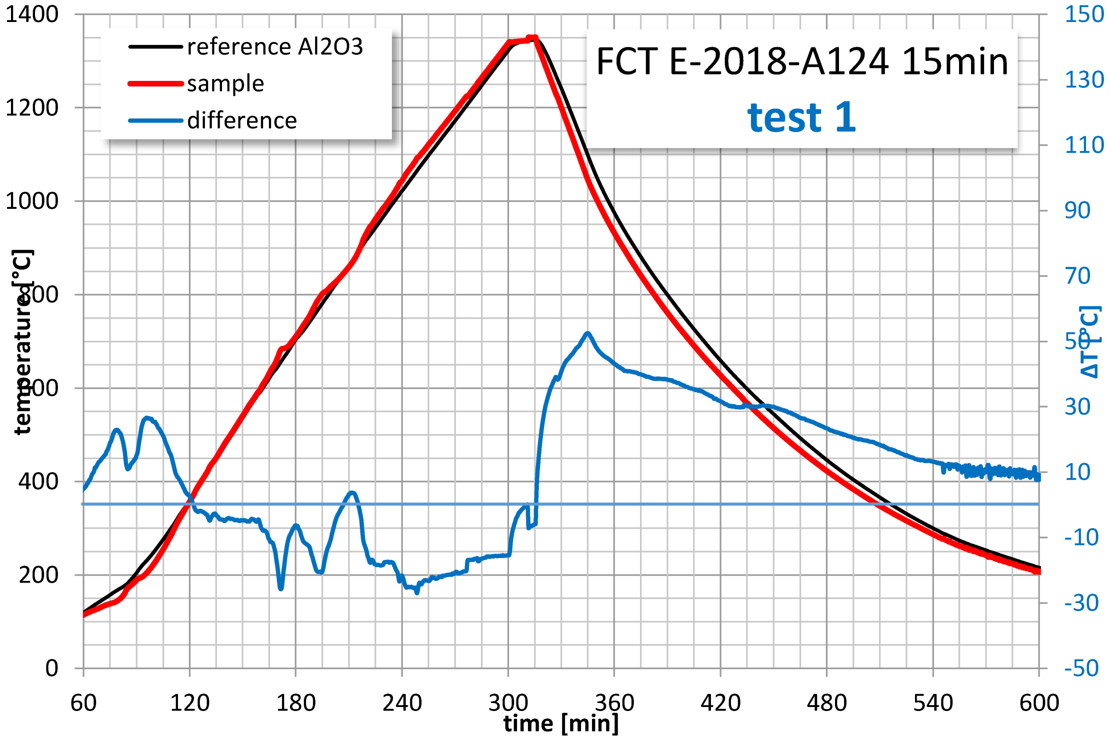

Figure D6. FCT result of E-2018-A124

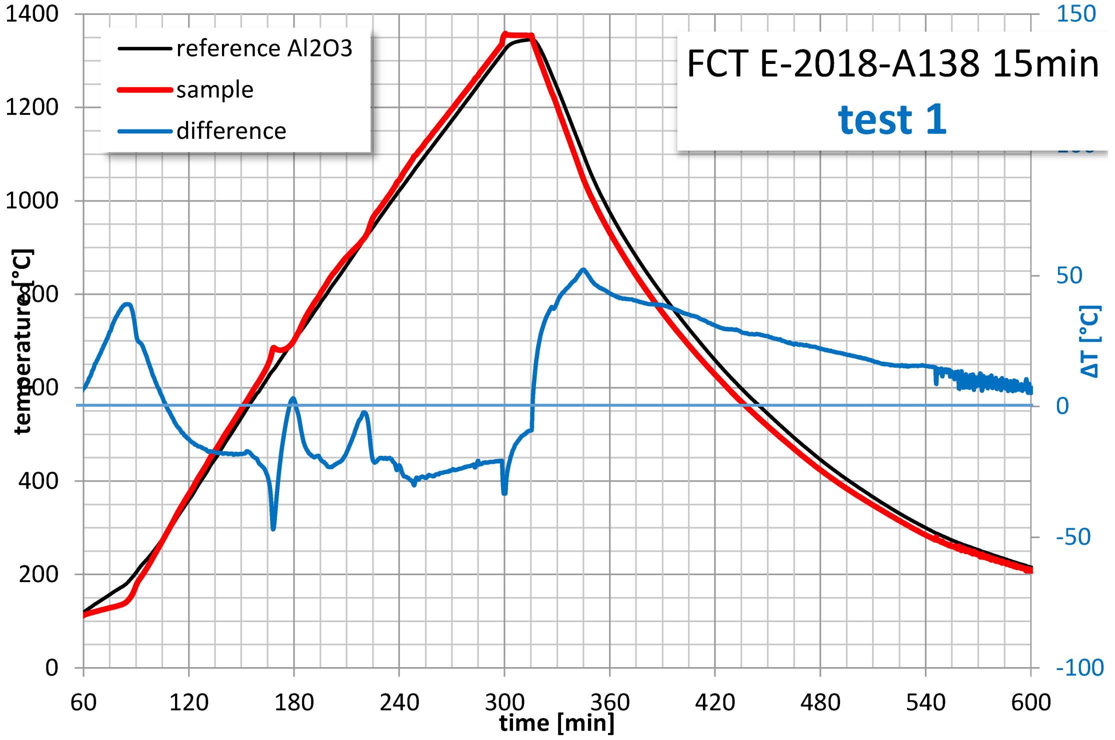

Figure D7. FCT result of E-2018-A138

Table D1. Chemical compositions of the FCT specimens according to SEM

| slag serial | [wt%] | $SiO_2$ | CaO | $Na_2O$ | $K_2O$ | MgO | $TiO_2$ | FeO | MnO | $Al_2O_3$ | $B_2O_3$ | C/S |
|---|---|---|---|---|---|---|---|---|---|---|---|---|
| E-2018-A002 | | 41.55 | 34.65 | 6.67 | 6.06 | 2.69 | 8.67 | 0 | 0 | 0 | 0 | 0.83 |
| E-2018-A010 | | 34.45 | 26.87 | 12.11 | 7.41 | 3.55 | 10.14 | 0 | 0 | 5.07 | 0 | 0.78 |
| E-2018-A015 | | 30.02 | 21.62 | 14.09 | 8.83 | 4.41 | 13.28 | 0 | 0 | 8.33 | 0 | 0.72 |
| E-2018-A018 | | 34.86 | 26.32 | 11.74 | 6.74 | 3.32 | 9.97 | 1.02 | 0.95 | 4.83 | 0 | 0.76 |
| E-2018-A033 | | 35.19 | 25.05 | 13.90 | 7.87 | 3.52 | 10.01 | 0 | 0 | 4.91 | 0 | 0.71 |
| E-2018-A040 | | 39.84 | 30.65 | 11.92 | 5.50 | 2.61 | 8.14 | 0 | 0 | 1.01 | 0 | 0.77 |